POLITECNICO DI MILANO

School of Industrial and Information Engineering

Master's Degree in Biomedical Engineering

CARDIAC CELLS PHOTOSTIMULATION THROUGH MOLECULAR PHOTOSWITCHES

Supervisor:

Prof. Guglielmo Lanzani

Cosupervisors:

Prof. Danilo Demarchi

Prof. Francesco Lodola

Vito Vurro

Master's Thesis of:

Beatrice Federici

Matr. 918255

Academic Year 2019 - 2020

ai miei nonni

Contents

List of Figures

List of Tables

Sommario

Estratto

La stimolazione ottica sta emergendo come promettente tecnologia per la gestione di alcune aritmie cardiache, con importanti vantaggi rispetto alle tradizionali terapie basate sulla stimolazione elettrica. In questo contesto, l'utilizzo di *fotoswitch* molecolari costituisce la nuova frontiera della stimolazione ottica non genetica.

Questo lavoro di tesi ha dimostrato la capacità di una molecola fotosensibile, chiamata Ziapin2, di modulare la frequenza di contrazione di cellule cardiache differenziate. Dall'analisi dei video raccolti con un microscopio ottico è stato osservato come la fotostimolazione di cellule cardiache caricate con il fotocromico sia responsabile di un incremento significativo della loro contrattilità, con un effetto reversibile e ripetibile. Al momento, il meccanismo biologico alla base di questa risposta funzionale resta ancora da indagare, sebbene i dati preliminari raccolti con esperimenti di elettrofisiologia e di localizzazione abbiano permesso di escludere che il processo biologico coinvolto sia uguale a quello osservato in altri modelli cellulari. Ulteriori esperimenti devono essere condotti per consentire la traslazione di questa tecnologia a modelli più complessi del tessuto cardiaco.

Parole chiave: *Fotoswitch* molecolari, Cardiomiociti differenziati, Frequenza di contrazione, Elettrofisiologia, Localizzazione della molecola

Introduzione

L'utilizzo di dispositivi elettrici, come il pacemaker o il cardiovertitore-defibrillatore impiantabile, costituisce attualmente il trattamento più comune per la gestione delle aritmie cardiache, con più di 1 milione di pacemakers e 300.000 cardiovertitori-defibrillatori impiantati all'anno [1]. Sebbene queste procedure mediche si siano dimostrate sicure e affidabili, sono ancora presenti importanti complicazioni legate all'utilizzo di questi dispositivi in clinica, specialmente per i defibrillatori impiantabili. I problemi principali sono dovuti alla durata limitata della batteria, che implica la sostituzione dei dispositivi ogni 4-7 anni con un alto rischio di infezione [2], [3], e alle sensazioni di dolore per lo più associate con gli shock elettrici generati dai cardiovertitori-defibrillatori per terminare le tachiaritmie [4].

Una emergente linea di ricerca sta esplorando l'uso della luce visibile, al posto della corrente elettrica, per modulare l'attività del cuore. Questo approccio innovativo presenta promettenti opportunità per il trattamento delle aritmie cardiache sia in termini di dolore, sia in termini di fabbisogno energetico [5]–[7]. Inutile dire che le

cellule cardiache non mostrano alcuna risposta biologica ad uno stimolo luminoso di per sè e che, pertanto, la stimolazione ottica del miocardio richiede necessariamente che il tessuto sia reso in qualche modo fotosensibile. A tale scopo, diverse strategie sono state proposte negli ultimi decenni. Il principio di base, comune a tutti questi approcci, è l'uso di un elemento sensibile alla luce e in grado di trasdurre le onde luminose in una particolare risposta biologica, che è a sua volta in grado di innescare l'eccitazione cellulare. In questo contesto, le due tecnologie attualmente più diffuse sono l'optogenetica [8], [9] e l'utilizzo di interfacce polimeriche fotosensibili [10], [11]. Nonostante i promettenti risultati ottenuti con entrambi gli approcci in numerosi esperimenti, esistono ancora seri problemi etici e sfide tecnologiche che ne impediscono l'effettiva traslazione in clinica come terapie per la gestione delle aritmie cardiache. Per fronteggiare alcune di queste problematiche e mantenere al contempo i vantaggi legati alla stimolazione ottica, è stata proposta negli ultimi un'alternativa basata sull'utilizzo di *fotoswitch* molecolari. L'uso di composti molecolari fotosensibili, infatti, non richiede alcuna modifica genetica delle cellule, come invece è richiesto dall'approccio optogenetico. Inoltre, dato che una molecola può essere facilmente distribuita nei tessuti, questo approccio potrebbe dimostrarsi essere anche più versatile rispetto all'uso di un attuatore a base polimerica in cui l'interfaccia deve essere verosimilmente posizionata in prossimità delle cellule da eccitare.

In accordo con tali premesse, questo lavoro di tesi ha voluto valutare la capacità di un *fotoswitch* molecolare, chiamato Ziapin2, di modulare l'attività delle cellule cardiache. Questo attuatore aveva già precedentemente dimostrato la sua funzionalità nei neuroni ippocampali primari mediante un effetto opto-meccanico applicato sulla membrana cellulare [12], ma nessuno studio completo era stato condotto sulle cellule cardiache prima di questo lavoro di tesi. É importante osservare che nelle cellule cardiache l'eccitazione provoca la contrazione cellulare grazie all'accoppiamento *eccitazione-contrazione* che caratterizza questo tessuto muscolare [13], e, di conseguenza, il comportamento delle cellule in termini di contrazione può essere utilizzato come indice della loro attività elettrica. Per tale motivo, il *rate* di contrazione delle cellule caricate con il fotocromico è stato monitorato durante lo stimolo luminoso. Una volta osservata la presenza di un effetto funzionale indotto dalla luce sulla contrazione cellulare, sono state esplorate le proprietà elettrofisiologiche delle cellule e la localizzazione molecolare. Queste ultime prove sono state condotte con l'obiettivo di fornire informazioni aggiuntive riguardo al fenomeno osservato, consentendo di avanzare ipotesi speculative sul meccanismo biologico coinvolto.

Procedure sperimentali

Modello cellulare. Come modello cellulare per le cellule cardiache sono stati utilizzati dei cardiomiociti derivanti da cellule staminali pluripotenti indotte (iPSCs). Questo modello cellulare offre diversi vantaggi rispetto ad altre fonti cellulari sia in termini di disponibilità, sia per il fatto che evita numerose problematiche etiche legate per esempio all'utilizzo di cellule staminali embrionali. Tuttavia, nonostante il protocollo di differenziamento consenta di raggiungere un ottimo livello di maturazione, queste cellule non sono ancora in grado di assomigliare sotto

tutti gli aspetti ai cardiomiociti. A titolo di esempio, la contrazione spontanea che caratterizza i cardiomiociti derivanti da iPSCs potrebbe aver influenzato l'analisi del comportamento di contrazione. Allo stesso modo, la variabilità associata a questo modello cellulare potrebbe aver causato una risposta irregolare da parte delle cellule.

Fotostimolazione. I cardiomiociti differenziati sono stati incubati con il *fotoswitch* molecolare, utilizzando dimetilsolfossido (DMSO) o acqua come solventi. L'illuminazione dei cardiomiociti differenziati è stata ottenuta tramite un sistema a LED in fibra accoppiato a un microscopio invertito, sia durante l'analisi di contrattilità che durante gli esperimenti di *patch-clamp*. La sorgente luminosa utilizzata è caratterizzata da un massimo di emissione in corrispondenza dei 470 nm (per combaciare con lo spettro di assorbimento di Ziapin2) e da una densità di potenza di 50 mW/mm^2. Per quanto riguarda il protocollo di incubazione, è bene osservare che il processo di carico non può essere controllato e che, pertanto, le cellule analizzate potrebbero essere state caricate con la molecola solo in parte.

Contrattilità cellulare. Per le analisi della contrattilità cellulare, i cardiomiociti differenziati sono stati incubati con Ziapin2/DMSO (5 μM) e Ziapin2/H_2O (5μM; 25 μM). Una volta incubati con le molecole fotocromiche, i cardiomiociti sono stati videoregistrati con un microscopio ottico per monitorare qualsiasi variazione nel comportamento di contrazione a valle della stimolazione luminosa. Due protocolli di stimolazione sono stati utilizzati: un primo protocollo con un singolo periodo di stimolazione (470 nm, in modalità pulsatile a 1 Hz) e un secondo protocollo con due periodi di stimolazione (470 nm, in modalità pulsatile a 1 Hz). Per ciascuna concentrazione e solvente, il *rate* di contrazione è stato calcolato come media su quasi 100/200 cellule. L'elevata produttività e la relativa semplicità degli esperimenti di video-microscopia offrono importanti potenzialità per la caratterizzazione funzionale delle cellule cardiache. Al contrario, il fatto che gli esperimenti siano stati condotti a temperatura ambiente (22-24$°C$) potrebbe rappresentare una notevole limitazione di questo saggio sperimentale. Non perché i dati possano essere errati, quanto piuttosto per il fatto che la contrazione delle cellule cardiache è limitata a temperature inferiori a quella fisiologica [10], [14]. Di conseguenza, potrebbe essere stata osservata una risposta biologica minore rispetto a quella osservabile a 37$°C$. Ulteriori analisi dovranno essere ripetute in temperatura controllata. Le registrazioni raccolte sono state elaborate con un algoritmo per processare i video scritto in Matlab. Il codice è stato scritto con l'obiettivo di estrarre per ciascuna cellula i valori del *rate* di contrazione nelle diverse finestre temporali: prima dello stimolo, durante lo stimolo, dopo lo stimolo. Il codice utilizza un algoritmo di *tracking* [15]–[17] per stimare lo spostamento del corpo cellulare della specifica cellula durante la contrazione ed estrarre da questo un segnale di contrazione cellulare. L'analisi dei dati estratti è stata condotta su *Origin 8.0*.

Elettrofisiologia. I cardiomiociti differenziati sono stati incubati con Ziapin2/H_2O (5μM). Gli esperimenti di *patch-clamp* sono stati eseguiti con un amplificatore, accoppiato ad un microscopio invertito. I dati sono stati acquisiti con il software

pClamp-10, analizzati con *Clampfit* e le analisi statistiche condotte in *Origin 8.0*. Gli esperimenti condotti in modalità *whole-cell* sono stati eseguiti a temperatura ambiente (22-24°C). Le cellule sono state illuminate con stimoli luminosi sia corti (20 ms) che lunghi (200 ms, 1000 ms). Solo cellule singole sono state selezionate per queste registrazioni. La modalità *current-mode* (I=0) è stata utilizzata per valutare la variazione del potenziale della membrana di tensione in caso di illuminazione, nonché la generazione di potenziali di azione. Uno stimolo a doppia frequenza (approccio delle *due sinusoidi*) è stato, invece, utilizzato per stimare la capacità della membrana e monitorarne le variazioni dopo lo stimolo luminoso. Si noti che gli esperimenti di *patch-clamp* hanno un rendimento estremamente basso, sebbene restino la tecnologia più diffusa e più precisa per misurare le correnti che attraversano la membrana cellulare. Di conseguenza, solo poche cellule sono riuscite ad essere analizzate durante questi esperimenti preliminari (circa 20 cellule per ogni condizione). Ulteriori esperimenti sono richiesti per confermare i risultati ottenuti.

Localizzazione. I cardiomiociti differenziati sono stati incubati con Ziapin2/DMSO (5 μM). Una volta caricate con il fotocromico, le cellule sono state trattate con una sonda per il reticolo endoplasmatico, per 30 minuti a 37°C. Dopo l'incubazione della sonda, le cellule sono state lavate correttamente per rimuovere il marcatore non interiorizzato. Le immagini di fluorescenza sono state acquisite con un microscopio confocale e un obiettivo ad olio. I parametri di eccitazione/emissione utilizzati sono riportati di seguito. Ziapin2: ex 488 nm; em 560-640 nm; reticolo endoplasmatico: ex 590 nm, em 620-700 nm. Si noti che la sonda utilizzata in questo test non è capace di distinguere correttamente tra reticolo sarcoplasmatico e reticolo endoplasmatico, due endomembrane ampiamente estese nei cardiomiociti differenziati.

Risultati e Discussione

Contrattilità cellulare. I dati raccolti con il protocollo *singolo periodo di stimolazione* suggeriscono che lo stimolo luminoso a 470 nm è in grado di aumentare la frequenza di contrazione dei cardiomiociti differenziati e caricati con Ziapin2. Questo fenomeno è stato osservato a temperatura ambiente, sia quando il fotocromico era stata caricato utilizzando come solvente il DMSO, sia quando era stata utilizzata l'acqua (aumento della freqeunza di contrazione durante lo stimolo di luce rispetto alla frequenza prima dello stimolo. Ziapin2/DMSO: 13 %; Ziapin2/H_2O (5 μM): 4 %; Ziapin2/H_2O (25 μM): 12 %. aumento della freqeunza di contrazione dopo lo stimolo di luce rispetto alla frequenza prima dello stimolo. Ziapin2/DMSO: 18 %; Ziapin2/H_2O (5 μM): 2 %; Ziapin2/H_2O (25 μM): 16 %). È importante sottolineare che nessun incremento statisticamente significativo è stato osservato nelle condizioni di controllo. Il protocollo caratterizzato da *due periodi di stimolazione* ha mostrato che gli effetti indotti dal primo stimolo luminoso sono reversibili e ripetibili. In altri termini, il trend ascendente nel valore di freqeunza di contrazione media è visibile sia durante il primo periodo di stimolazione, sia durante il secondo.

Nonostante sia Ziapin2/DMSO che Ziapin2/H_2O abbiano dimostrato un aumento della contrattilità cellulare durante lo stimolo luminoso, a parità di concentrazione,

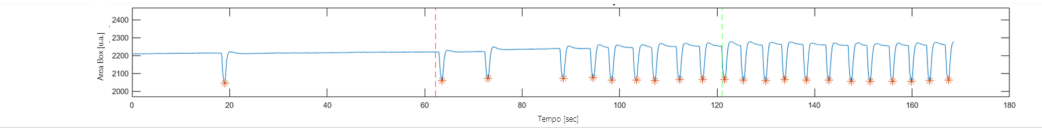

Segnale di contrazione. *Il segnale di contrazione è estratto da una cellula cardiaca differenziata da iPSCs e caricata con Ziapin2 durante lo stimolo luminoso (470 nm in modalità pulsatile a 1 Hz; 50 mW/mm^2; temperatura ambiente). Il segnale viene calcolato come area di un rettangolo posto attorno alla singolo cellula di interesse. Durante il periodo di stimolazione, lo spostamento del corpo cellulare (che si verifica ad ogni contrazione) è calcolato e il valore ottenuto è utilizzato per rimpicciolire o ingrandire il rettangolo attorno alla cellula. I minimi dell'area del rettangolo (asterischi arancioni), corrispondono agli istanti in cui la cellula è contratta. La linea rossa tratteggiata indica l'accensione della luce. Linea verde tratteggiata, invece, segna lo spegnimento della luce.*

gli effetti osservati con il DMSO sono risultati essere molto più evidenti e duraturi di quando lo fossero quelli ottenuti utilizzando l'acqua come solvente. É interessante notare che, usando una concentrazione maggiore di Ziapin2/H_2O (25 μM), la risposta funzionale aumenta e la modulatione del *rate* di contrazione mostra un trend simile a quello osservato nel caso di Ziapin2/DMSO. Questo risultato potrebbe suggerire che la presenza di aggregati in Ziapin2/H_2O [18] riduca la quantità di molecole funzionali singole capaci di essere facilmente internalizzate dalle cellule durante la fase di carico. Un'ipotesi alternativa è che il DMSO aumenti la permeabilità della membrana cellulare [19], favorendo l'ingresso della molecola fotosensibile all'interno della cellula. Di conseguenza, una maggiore concentrazione deve essere usata nel caso di H_2O per raggiungere una quantità di molecole internalizzate comparabile.

Un'ulteriore osservazione verte sul fatto che, indipendentemente dalla condizione e dalla concentrazione, le cellule che rispondono distintamente allo stimolo luminoso presentano per lo più una bassa o assente attività di contrazione a riposo. In queste cellule, l'incremento relativo del *rate* di contrazione raggiunge più del 200 % rispetto alla frequenza iniziale. É stato ipotizzato che questo fenomeno sia dovuto alla presenza di un limite massimo nel *rate* di contrazione raggiungibile da una cellula cardiaca a temperatura ambiente (i cardiomiociti, infatti, sono noti contrarsi più lentamente a basse temperature [10], [14]). Se questo fosse vero, le cellule, che mostrano a riposo un *rate* di contrazione vicino al limite superiore non sono in grado di aumentare la loro attività contrattile, anche nel caso in cui ci sia uno stimolo. Al contrario, cellule che presentano una bassa attività contrattile a riposo hanno un margine più ampio per incrementare il proprio *rate* di contrazione prima di raggiungere il limite superiorie. In alternativa a questa ipotesi, non si può escludere al momento la possibilità di una connessione tra la ridotta attività spontanea e il fatto che queste cellule abbiano effettivamente internalizzato la molecola. Infatti, è possibile che il fotocromico venga internalizzato solo da alcune cellule, ne modifichi l'attività spontanea e sia in grado di aumentare marcatamente la loro contrattilità quando illuminato.

Elettrofisiologia. L'aumento della contrattilità cellulare è stato associato ad una modulazione bifasica del potenziale di membrana e ad un aumento nella frequenza dei potenziali di azione generati. I dati raccolti con Ziapin2/H_2O (5

μM) suggeriscono che gli impulsi luminosi, sia che siano brevi sia che siano lunghi, inducono un'iperpolarizzazione transitoria del potenziale di membrana seguita da una modesta depolarizzazione. Questo effetto di *rebound* è stato visto verificarsi entro circa 350 ms dall'accensione della luce, sia per brevi che per lunghi impulsi luminosi. Il confronto con il controllo (senza molecola) ha permesso di confermare la significatività dei picchi di iperpolarizzazione e depolarizzazione.

I dati raccolti su cellule che non mostravano attività elettrica prima dello stimolo luminoso hanno dimostrato che più del 60% delle cellule genera almeno un potenziale di azione dopo l'insorgenza della luce e che questa risposta cellulare è mantenuta quando più stimoli sono applicati uno di seguito all'altro. Vale la pena sottolineare che i potenziali di azione sono registrati nei tracciati con un marcato ritardo rispetto al picco di depolarizzazione (tempo tra lo stimolo luminoso e il primo potenziale di azione. media ± s.e.m. 20 ms: 2,996 ± 0,653 s; 200 ms: 2,636 ± 0,597 s). Questo risultato potrebbe essere indicativo di un processo biologico che intercorre tra i due eventi.

La capacità di membrana dei cardiomiociti derivanti da iPSCs è stata anche studiata, dato che una modulazione simile del potenziale di membrana era stata precedentemente osservata nei neuroni in corrispondenza di una diminuzione della capacità di membrana all'accensione dello stimolo luminoso [12]. Tuttavia, i valori di capacità sono rimasti approssimativamente costanti tra prima e dopo lo stimolo luminoso (diminuzione media ± s.e.m.: 0,083 ± 0,011 pF, ovvero un calo di meno di 0,5 % del valore di capacità iniziale). Questo risultato suggerisce che la modulazione bifasica del potenziale non sia riconducibile ad una variazione della capacità di

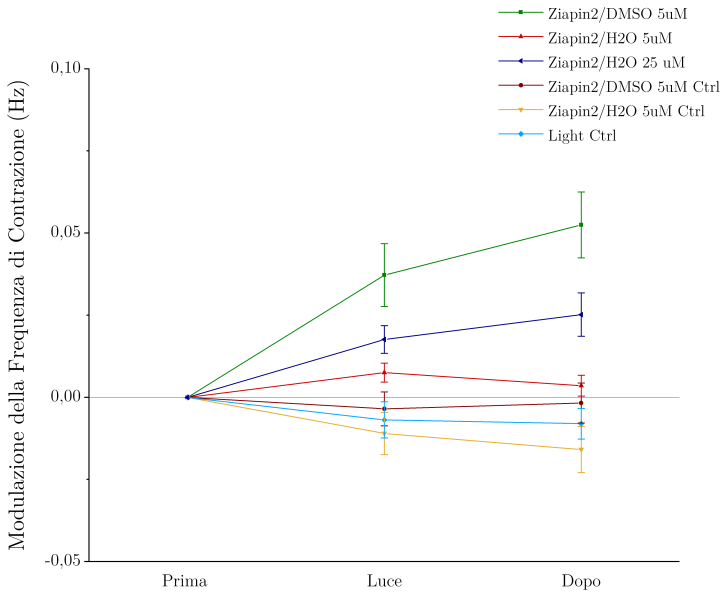

Frequenza media di contrazione. *Variazione della frequenza di contrazione in cellule cardiache differenziate da iPSCs e caricate con Ziapin2. La modulazione del rate di contrazione (CR) è intesa come ΔCR. Prima: ($CR_{Prima} - CR_{Prima}$); Luce: ($CR_{Luce} - CR_{Prima}$); Dopo: ($CR_{Dopo} - CR_{Prima}$). Ziapin2/DMSO (5 μM): n = 126; Ziapin2/H_2O (5 μM): n = 202; Ziapin2/H_2O (25 μM): n = 202; Ziapin2/DMSO Ctrl: n= 25; Ziapin2/H_2O Ctrl: n = 53; Light Ctrl: n=43.*

membrana. Tale ossservazione è in accordo con i risultati ottenuti dagli esperimenti di localizzazione, nei quali è stato osservato che la molecola localizza nello spazio intracellulare e non in membrana come era stato visto per i neuroni. Ne consegue che il meccanismo coinvolto nei cardiomiociti differenziati debba essere diverso da quello osservato in precedenza in altri modelli cellulari.

Localizzazione. Dato che la localizzazione di una molecola è strettamente correlata alla sua funzione biologica, la colocalizzazione di Ziapin2 con alcune strutture cellulari è stata analizzata. Come accennato sopra, le immagini di fluorescenza raccolte suggeriscono che il *fotoswitch* molecolare sia in grado di attraversare la membrana cellulare e localizzarsi nello spazio intracellulare. Studi teorici precedenti avevano dimostrato la presenza di una barriera energetica al desorbimento della molecola dalla membrana verso il citoplasma. Pertanto, ci si aspettava che la molecola si stabilizzasse in membrana, come osservato sia nei neuroni [12] sia nelle Hek293 [18]. É stato ipotizzato che un sistema di trasporto specifico o una diversa composizione della membrana debbano essere presenti nei cardiomiociti differenziati per giustificare questo risultato.

Oltre al processo di internalizzazione, è stata presa in considerazione anche la localizzazione esatta della molecola all'interno dello spazio intracellulare. Il segnale di fluorescenza emesso da Ziapin2 è stato osservato provenire da strutture simili a micelle o essere concentrato in una regione perinucleare sovrapposto parzialmente al segnale emesso della sonda per il reticolo endoplasmatico. Per quanto concerne le strutture vescicolari, si è ipotizzato che tali micelle corrispondano ad aggregati molecolari. Questa assunzione deriva da studi precedenti nei quali è stato visto che Ziapin2 tende ad aggregarsi in acqua [18]. Al contrario, il segnale emesso dallo spazio perinucleare è stato ricondotto ad una frazione di molecole funzionali colocalizzate con una endomembrana o in qualche modo schermate dall'ambiente

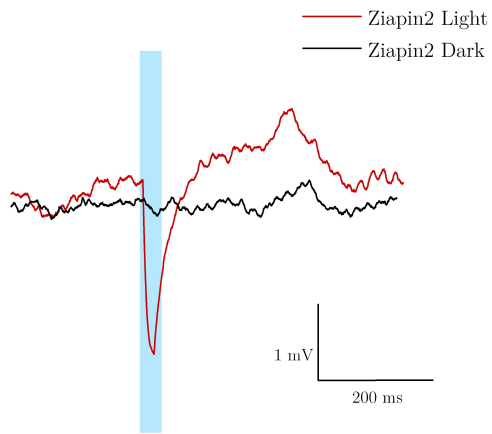

Variazione del potenziale di membrana. *Tracce rappresentative di whole-cell current-clamp registrati da cardiomiociti derivanti da iPSCs caricati con Ziapin2/H_2O (5 μM) al buio (nero) e dopo lo stimolo luminoso (rosso). L'area indicata in azzurro rappresenta l'impulso di luce visibile (durata: 20 ms). Ogni traccia si ottiene come media di 20 sweeps consecutivi.*

acquoso del citoplasma. Non è ancora chiaro dove queste molecole siano posizionate e come contribuiscano all'aumento della frequenza di contrazione. Ulteriori studi sono necessari per comprendere completamente il meccanismo coinvolto.

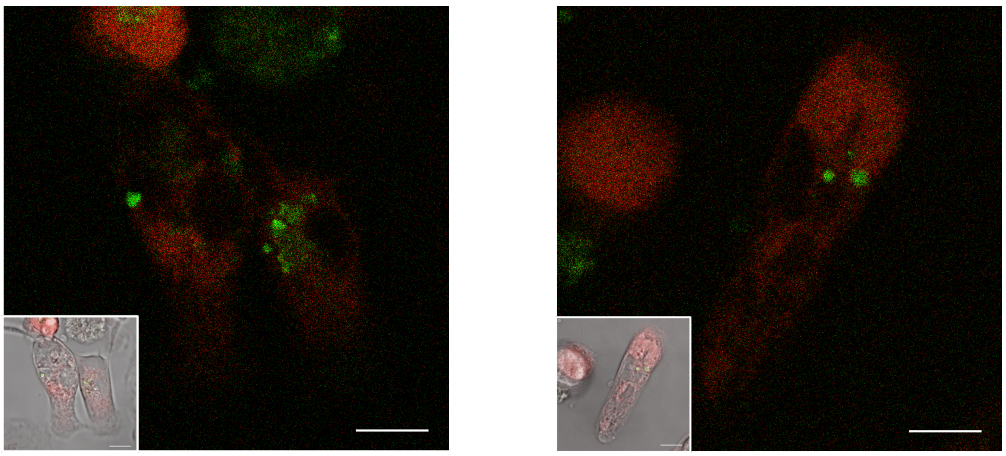

(a) **(b)**

Immagini in fluorescenza. *Colocalizzazione tra Ziapin2 e il reticolo endoplasmatico in cardiomiociti differenziati da iPSCs. Ziapin2: verde. Sonda per il reticolo endoplasmatico: rosso. Scala = 10 μm*

Conclusione

Questo lavoro di tesi ha dimostrato la capacità di Ziapin2 di modulare la risposta funzionale di cardiomiociti, derivanti da cellule staminali pluripotenti indotte, quando sottoposti a stimolo luminoso. In particolare, i video raccolti con il microscopio ottico suggeriscono che la luce sia in grado di indurre un aumento significativo del *rate* di contrazione cellulare e che questo effetto è reversibile e ripetibile. Il meccanismo biologico responsabile di tale aumento non è ancora stato identificato, ma alcuni risultati preliminari sulla capacità della membrana e la localizzazione della molecola sembrano indicare che il processo coinvolto è diverso da quello precedentemente osservato in altri modelli cellulari.

I prossimi studi saranno mirati a caratterizzare il meccanismo biologico coinvolto e verificare la possibilità di modulare la contrazione cellulare ad una precisa frequenza definita dallo stimolo luminoso. Inoltre, l'estensione di queste scoperte da esperimenti su singola cellula a esperimenti su tessuti cardiaci sarà necessaria per dimostrare la capacità della stimolazione ottica di provocare la contrazione sincrona di tutte le cellule illuminate.

Summary

Abstract

Optical stimulation is emerging as a promising technology to restore healthy heartbeats, with potential improvements over traditional electronic device therapy. In this respect, molecular photoswitches are rapidly spreading as the new frontier of non-genetic approaches for cardiac photostimulation.

This work provides evidence of the capability of a light-sensitive azobenzene compound, named Ziapin2, in modulating the contraction behavior of differentiated cardiomyocytes. Video recordings collected with optical microscopy demonstrate that Ziapin2-loaded cardiac cells increase their contraction rate upon illumination and that this effect is reversible and repeatable. Although at present few is known about the biological mechanism involved, preliminary patch-clamp experiments and localization assays have confirmed that it should be different from the membrane-related opto-mechanical effect observed in other cellular models. Further studies are required to fully understand the phenomenon and translate this nanoscale tool towards a more complex model of cardiac tissue.

Keywords: Molecular photoswitches, Differentiated cardiomyocytes, Contraction rate, Electrophysiology, Molecule localization

Introduction

Electronic device therapy is currently the first-line treatment for cardiac arrhythmias, with more than 1 million pacemakers and 300,000 implantable cardioverter-defibrillators implanted per year [1]. Although these medical procedures have demonstrated to be relatively safe and reliable, device-related complications are not insignificant, especially for cardioverter-defibrillators. Major issues are due to the limited battery life, which implies device replacements every 4–7 years [2], [3], and pain sensation, mostly associated with the high-energy shocks generated by implantable cardioverter-defibrillators to terminate tachyarrhythmias [4].

An emerging field of research is exploring the use of visible light, instead of electrical currents, to modulate the activity of the heart and eventually treat cardiac arrhythmias. This groundbreaking approach presents promising opportunities for restoring normal heart rhythm painlessly and with modest energy requirements [5]–[7]. Needless to say, cardiac cells do not display any response to light by themselves, thus a strategy to induce light-sensitivity should be drafted. To this end, different approaches have been proposed over the last decades. The basic

principle, common to all, is the use of a light actuator able to transduce light into a biological response, which ultimately triggers cell excitation. Although optogenetics [8], [9] and polymer-based interfaces [10], [11] have expanded rapidly in this field with promising preliminary results, there are still potential hurdles to their translation as clinical cardiac anti-arrhythmic therapies. A further improvement of these technologies might be offered by photoactivable molecules, and especially by molecular photoswitches [20]–[23]. Indeed, this class of chemical compounds could be superior w.r.t. optogenetics since their use does not require the genetic modification of tissue prior to optical stimulation. Moreover, given that a molecule can be easily distributed in tissue, this approach could also be more versatile than the use of a polymer-based actuator in which the interface should be necessarily positioned close to the targeted cells.

According to these premises, this thesis work wanted to evaluate the capability of a recently developed molecular photoswitch, Ziapin2, in modulating cardiac cells activity. This azobenzene-based light actuator had already proven its functionality in primary hippocampal neurons by the means of an opto-mechanical effect applied on cell membrane [12], but no complete study had been carried out to assess its usability in cardiac cells before this work. Given that, in the cardiac domain, excitation results in cell contraction due to the peculiar *excitation-contraction coupling* [13], the contraction rate (CR) of optically stimulated Ziapin2-loaded cardiac cells was monitored to assess whether Ziapin2 could modulate contraction behavior or not. Once observed the presence of a functional effect elicited by the photoswitch on cell contraction, the electrophysiological properties of the cells were explored, together with the molecular localization. These latter assays were of crucial importance even if only to speculate about the possible biological mechanism responsible for the observed effects.

Experimental procedures

Cellular model. Cardiomyocytes derived from human induced pluripotent stem cells (hiPSC-CMs) were used as a cellular model for cardiac cells. This cellular model offers several advantages over other cell sources both in terms of availability and ethics. However, despite the increased level of maturation reached by mature hiPSC-CMs, these cells still lack to achieve a complete functional maturation that allows them to resemble in all respects to CMs. For instance, the presence of spontaneous beating before the stimulus application could have affected the measurements. Likewise, the variability associated with this cellular model may have caused an uneven response from cells.

Photostimulation. hiPSC-CMs were incubated with molecular photoswitch, either using dimethyl sulfoxide (DMSO) or water as solvents (for 7 minutes at $37°C$). Illumination of hiPSC-CMs during contractility analysis and patch-clamp experiments was provided by a LED system fiber-coupled to a microscope. The light source emission peaked at 470 nm (to match the Ziapin2 absorption spectrum). The power density of the source was about 50 mW/mm^2. Concerning the incubation protocol, it is worth mentioning that the loading process cannot be controlled and

that, therefore, some cells might have internalized the Ziapin2 molecule and others not.

Contractility analysis. hiPSC-CMs were incubated with Ziapin2/DMSO (5 μM) and Ziapin2/H_2O (5μM; 25 μM). Once incubated with the photochromic molecules, hiPSC-CMs were video recorded with optical microscopy to monitor the contraction behavior upon illumination. Videos were acquired with *Nikon Eclipse Ti* and a $20x$ objective. Two stimulation protocols were used: a *single stimulation protocol* with a single stimulation period (470 nm, 1 Hz for 60 s), and a *double stimulation protocol* with two repeated stimulation periods (470 nm, 1 Hz for 2$\times$ 60 s). For each condition, the mean CR was computed from almost 100/200 of cells. The high-throughput of video microscopy experiments offer important potentialities for the functional characterization of cardiac cells. On the contrary, the fact that the experiments were conducted at room temperature (22-24$°C$) could represent a remarkable limitation of this experimental assay. Indeed, from the literature it is known that a lower temperature can dramatically reduce the cell contraction capabilities [10], [14]. The collected video recordings were processed with a custom-built Matlab-based code to extract the values of CR over the different time windows: before light stimulus, during light stimulus, after light stimulus. The code uses a tracking algorithm [15]–[17] to estimate the displacement of the cell body during the contraction and extract from this value a beating signal. Statistical analysis and data analytics were conducted on *Origin 8.0*.

Electrophysiology. hiPSC-CMs were incubated with Ziapin2/H_2O 5μM. Standard patch-clamp recordings were performed using an amplifier coupled to an inverted microscope. Data were acquired with *pClamp-10* software and processed with *Clampfit*. Exploratory data analysis was conducted on *Origin 8.0*. Whole-cell recordings of hiPSC-CMs were performed at room temperature (22–24$°C$) with freshly pulled glass pipettes, filled with an intracellular solution. Only single cells were selected for recordings and enlightened with both short (20 ms) and long (200 ms, 1000 ms) light stimuli. Current-clamp mode (I=0) was used to assess variation in the voltage membrane potential upon illumination, as well as the firing activity. Additionally, capacitance measurements were performed using the *two-sinusoids* approach. Note that patch-clamp assays, though being the standard reference for high-precision electrical measurements of cells, have an extremely low yield. As a consequence, at present only few cells were analyzed (i.e., about 20 cells for each light stimulus condition). Thus, further experiments should be carried out to confirm these results.

Localization. hiPSC-CMs were incubated with Ziapin2/DMSO (5 μM). After the standard loading procedure, cells were treated with an endoplasmatic reticulum (ER) probe, for 30 minutes at 37$°C$. After the probe incubation, cells were washed properly to remove the not-internalized marker. Fluorescence images were acquired with a confocal microscope and a oil objective. Excitation/emission parameters. Ziapin2: ex 488 nm; em 560-640 nm; reticolo endoplasmatico: ex 590 nm, em 620-700 nm. Note that the probe used in this assay cannot properly distinguish

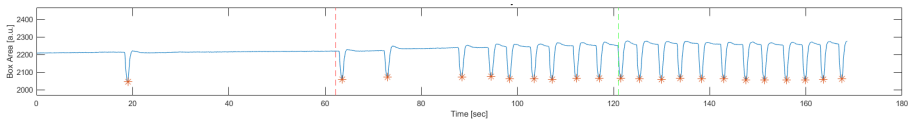

Beating signal during light stimuli. *Representative beating signal of a Ziapin2-loaded hiPSC-CM upon illumination. The signal is computed as area of the box surrounding a cell over the stimulation period (470 nm; 50 $mW mm^2$; room temperature). Dashed red line: light onset. Dashed green line: light offset. Orange star: minimum of beating signal, i.e. single contraction.*

between sarcoplasmic reticulum (SR) and ER, two extended endomembranes in hiPSC-CMs.

Results and Discussion

Contractility analysis. Collected data suggested that Ziapin2-loaded hiPSC-CMs can increase their contraction rate upon illumination at room temperature, either when Ziapin2 is loaded with DMSO or with water (mean increase during the light stimulus and post it w.r.t. resting condition. Ziapin2/DMSO: 13 %, 18 %; Ziapin2/H_2O (5 μM): 4 %, 2 %; Ziapin2/H_2O (25 μM): 12 %, 16 %). No statistically significant increment was observed in the control conditions. Importantly, the *double stimulation* protocol provided evidence that the observed effects are reversible and repeatable, which implies that the ascending trend observed during the first light stimulus in the mean CR was visible also when the second light pulse was turned on. Despite both Ziapin2/DMSO and Ziapin2/H_2O demonstrated an increase in cell contractility upon illumination, at equal concentration the effects were much more striking and long-lasting with Ziapin2/DMSO rather than Ziapin2/H_2O. Interestingly, the marked effect observed with Ziapin2/DMSO was almost restored when a high concentration of Ziapin2/H_2O (25) was employed. This observation could suggest that the presence of aggregates in Ziapin2/H_2O [18] reduces the amount of free functional molecules in the medium that could be easily internalized by the cells during the loading phase. An alternative hypothesis is that DMSO enhances cell membrane permeability [19] favoring the entering of the molecular photoswitch within the cell and that a higher concentration should be used with Ziapin2/H_2O to obtain a comparable effect.

Besides these differences, it is interesting to observe that, independently from the condition, the cells that respond distinctly to light stimulus mostly present a low or zero beating rate at resting condition. In these cells, the relative increment in the CR reached much more than 200 % w.r.t. the resting CR. It could be speculated that this phenomenon is due to the presence of a maximum limit of CR that can be reached at room temperature (e.g. CMs contract more slowly at low temperatures [10], [14]). If this would be the case, those cells, which show at rest a CR close to the upper bond, are unlikely to increase the rate even if a trigger is present. Alternatively, it might be that a connection is present between the reduced spontaneous activity and the fact that these cells have internalized the molecule, which implies that they respond significantly to light. Further experiments are needed to validate these speculative hypotheses.

Electrophysiology. The increase in the contraction rate was associated with a biphasic modulation of the membrane potential upon illumination and the delayed generation of action potentials (APs).

Data collected on Ziapin2/H_2O-loaded hiPSC-CMs (5 μM) suggested that both

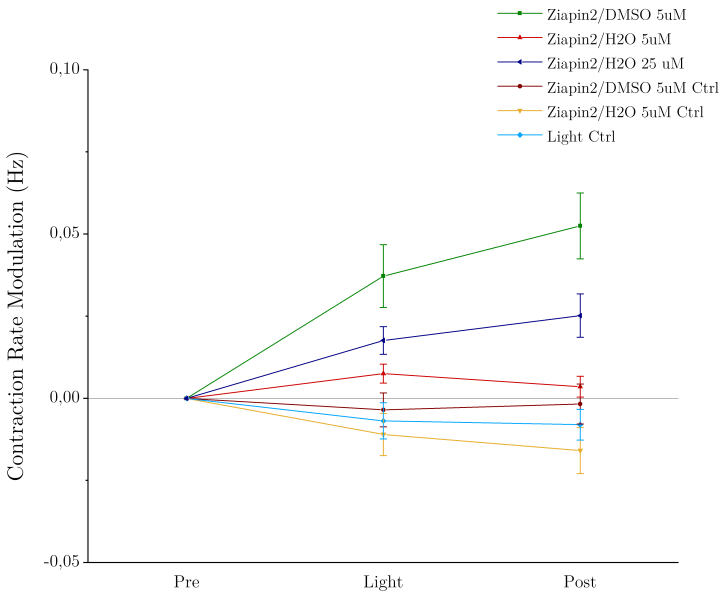

Contraction rate trend. *Contraction frequency of optically stimulated Ziapin2-loaded hiPSC-CMs. The contraction rate modulation is intended as* ΔCR. *Pre:* (CR_{Pre} CR_{Pre}); *Light:* (CR_{Light} CR_{Pre}); *Post:* (CR_{Post} CR_{Pre}). *Ziapin2/DMSO (5* μM*): n = 126; Ziapin2/*H_2O *(5* μM*): n = 202; Ziapin2/*H_2O *(25* μM*): n = 202; Ziapin2/DMSO Ctrl: n= 25; Ziapin2/*H_2O *Ctrl: n = 53; Light Ctrl: n=43.*

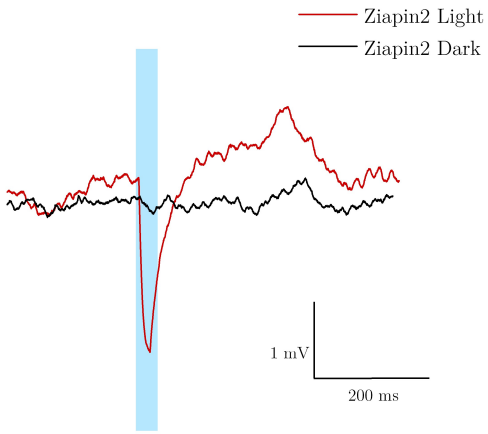

Membrane potential variation. *Representative whole-cell current-clamp trace recorded from a hiPSC-CM loaded with Ziapin2/*H_2O *(5* μM*) in dark (black) and upon illumination (red). Cyan shaded areas represent the visible light pulses (20 ms). Every trace is obtained as average of 20 consecutive sweeps.*

short and long pulses of visible light induce a transient hyperpolarization of the voltage membrane followed by a consequent depolarization within about 350 ms from the light onset. This membrane potential modulation appeared statistically significantly different from the control conditions. Data collected about the firing activity of spontaneously-not-beating cells showed that more than 60% of cells generate an AP after light onset and that this electrical response is maintained over multiple sweeps. Remarkably, the APs were generated with a marked delay w.r.t. the depolarization peak observed in the membrane voltage track (time between light onset and first AP. mean ± s.e.m. 20 ms: 2,996 ± 0,653 s; 200 ms: 2,636 ± 0,597 s). This result might be indicative of a biological pathway that occurs between the two events.

Given that a similar modulation of the membrane potential was observed in Ziapin2-loaded neurons [12] and associated with a capacitance drop upon illumination, the capacitance of hiPSC-CMs was also studied in dark and light conditions. Surprisingly, the capacitance values remained approximately constant after the light onset, suggesting that a different biological mechanism should be involved (mean decrease ± s.e.m.: 0,083 ± 0.011 pF, which corresponds to a drop of less than 0.5 % of the initial capacitance value). This finding was supported by the fluorescence images collected with the localization assay that demonstrated the intracellular localization of Ziapin2 in hiPSC-CMs, different from the membrane-loaded condition observed previously in neurons.

Localization. Since the location of a molecule is strictly related to its biological function, the colocalization of Ziapin2 with cellular structures of hiPSC-CMs was also analyzed. The collected fluorescence images hint that the photoswitch places intracellularly in hiPSC-derived CMs. The fact that the molecules are internalized by the cells was unforeseeable. Previous theoretical studies had proposed the presence of an energetic barrier to molecule desorption from the membrane to the cytosol that should have favored its stabilization at the membrane, as done in both neurons [12] and Hek293 [18]. To explain this unexpected result, it has been hypothesized that a specific transport system or membrane composition should be present in hiPSC-CMs.

Besides the internalization process, the precise localization within the intracellular space was also considered. The fluorescent signal of Ziapin2 was observed to be emitted from micelle-like structures or concentrated in perinuclear regions partially overlapped with the signal emitted by the ER probe. The observed clusters of cells were associated with molecular aggregates, given the known tendency of Ziapin2 to aggregate in water [18]. On the contrary, the signal emitted from the perinuclear space was proposed to be emitted from a fraction of functional molecules dwelled in an endomembrane or somehow shielded by the cytoplasmatic water-like environment. Where these molecules are precisely placed and how they contribute to the biological response is still unclear and further studies are needed to fully understand the involved mechanism.

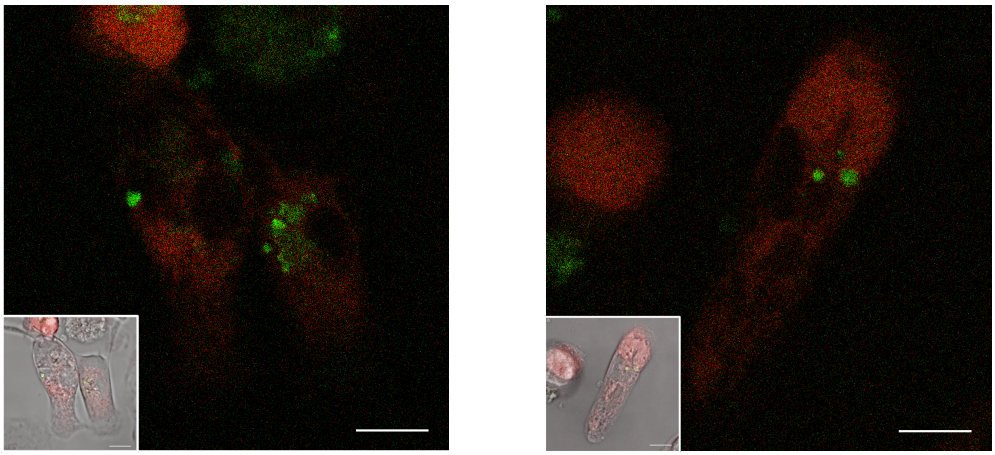

(a) **(b)**

Fluorescence images. *Confocal 3D-z-stack representative images of Ziapin2 fluorescence (green) in hiPSC-CMs and its colocalization with endoplasmatic reticulum probe (red). Scale bar = 10 µm*

Conclusions

This work has demonstrated the capability of Ziapin2 in modulating the functional response of Ziapin2-loaded hiPSC-CMs upon illumination. In particular, data collected with video microscopy suggest that a light stimulus can induce a significant increase in cell CR and that this effect is reversible and repeatable. The biological mechanism responsible for this increase has not yet been identified, but the results obtained from preliminary electrophysiological and localization assays indicate that the involved biological pathway should be different from the one previously observed in other cellular models.

Follow-up activities will aim to characterize the involved biological mechanism and verify the possibility of modulating the CR at a specific frequency set with the light stimulus. Moreover, the extension of these discoveries from single cell to the tissue level will be necessary to assess the capability of optical stimulation to elicit the synchronous contraction of all the enlightened cells.

Motivation and Problem Statement

Problem Description

The heart is a muscular organ primarily responsible for pumping blood and for distributing oxygen and nutrients throughout the body. The fulfillment of this blood-pumping function is possible by the presence of a complex electrical system that elicits the heart contraction and enables the consequent distribution of blood throughout the body.

Diseases or injuries can alter this physiological electrical activation of the heart, leading to abnormal heart rhythm, named arrhythmias, which in turn impair the pump-action, causing major complications. Arrhythmias affect millions of people and are associated with substantial morbidity and economic costs. Abnormalities of cardiac rhythm are prevalent and affect more than 2% of middle-aged and older adults with a rate of about 0.5% per year. Risk factors for rhythm abnormalities include older age, male sex, traditional cardiac risk factors, chronic kidney disease, and heart failure [24]. Existing therapies differ depending on the type of arrhythmia and its site of origin. Successful treatment methods include (1) catheter ablation, which suppresses the pathway of abnormal electrical propagation; (2) medications, which alter the cellular properties of cardiac tissue (i.e., anti-arrhythmic drugs); and (3) implantable cardiac pacemaker or cardioverter-defibrillators [25]–[27]. The latter are the first-line treatment in high-risk individuals, with a dramatic propensity for life-threatening arrhythmias and the greatest risk of sudden cardiac death (SCD) [28]. Besides the reduced mortality rate recorded in several clinical trials [29]–[31], unmet needs concerning implantable cardioverter-defibrillators (ICDs) remain [32]–[34]. High-voltage electric shocks can cause serious myocardial tissue damage [35], pain, and anxiety in a significant percentage of patients wearing an ICD [36]. A lot of research has been done over the last decades to tackle these issues and design more effective and painless new-generation devices for cardiac arrhythmia management, but there is still much room for improvement.

An emerging field of research has explored the use of light-based defibrillators to restore normal cardiac activity in case of atrial or ventricular tachyarrhythmias [7], [37]. Compared with high-energy electric shocks, optical stimulation of the light-sensitized heart could extinguish arrhythmia using significantly less energy and with an unprecedented spatio-temporal resolution, that allows avoiding any collateral excitation of muscles surrounding the heart, thereby eliminating the major source of defibrillation-induced pain and discomfort. Noticeable, optical stimulation of the heart requires that the heart has been previously made sensitive to light. To this end, few approaches are currently being investigated [38].

Among these, cardiac optogenetics has already succeeded to demonstrate its potentialities *in vitro*, *in silico*, and *in vivo*. Nevertheless, optogenetics still raises some significant concerns due to the required use of viral transfection [39] that precludes or at least postpone its translation to the clinic.
As opposed to this technique, the use of light actuators to be interfaced with the living matter offers a promising alternative option to induce cell light sensitivity. These light actuators can come in a variety of shapes and compositions and have already demonstrated their undeniable potential in optical cell stimulation, with major advantages w.r.t. both optogenetics and electrical stimulation [38].

Objectives

The long-term goal of this project is the use of molecular photoswitches to induce light sensitivity in the myocardium and open up new possibilities for cardiac arrhythmias treatment. As aforementioned, optical stimulation of cardiac cells has intriguing translational potential as a novel alternative to conventional electrical stimulation currently used in clinical devices. However, a large set of proof-of-concept experiments need to be performed to move this exciting new technology into the clinical environment. First of all, the novel therapy must be evaluated at a cellular level, followed by animal tests and computational studies. Only once all the pre-clinical studies will have provided extensive evidence of the potentialities of this new technology, clinical and pivotal studies could be carried out.

This thesis work lies only at the beginning of this long path, but it is worth to begin since *nil sine magno vita labore dedit mortalibus*[1].
The principal objective of this work was to evaluate the capability of a recently designed molecular photoswitch, named Ziapin2, in modulating the cardiac cells contraction behavior. To this end, the light-induced effects on cells contraction rate were characterized. In parallel, preliminary electrophysiology and localization assays were performed with the aim of collecting information useful to put forward some hypotheses about the biological mechanism involved.

[1] *Life gave nothing to mortals without great effort.* (Orazio, *Satire* 1,9,59-60)

Capitolo 1

Background

1.1 Cardiac electrophysiology

The heart is a muscular organ primarily responsible for pumping blood and for distributing oxygen and nutrients throughout the body. In mammals and birds, the heart is a four-chambered organ, divided into a right atrium and ventricle (commonly referred to as the right heart) separated from a left ventricle and atrium (the left heart). The left heart provides oxygenated blood to the body, while the right heart pumps the deoxygenated blood to the lungs [40]. This blood-pumping function is possible by a coordinated contraction of the heart muscular tissue, which follows an electrical activation of cardiac cells. Briefly, an electrical impulse is generated at a specific region of the heart and is routed through the anatomic conduction system of the heart to the rest of the myocardium tissue. This electrical signal activates cardiac cells and triggers their mechanical contraction [13], [40]. Noticeably, the maintenance of this synchronous contraction is strictly related to the peculiar cytoarchitecture of the myocardium and any alteration of this organized structure can lead to life-threatening complications [41].

Cardiac conduction system. The proper conduction of the electrical signal and the consequent synchronized contraction is controlled and triggered by the *cardiac conduction system*. The main components of this conductive system are the sinoatrial (SA) node, the atrioventricular (AV) node, the bundle of His, the bundle branches, and the Purkinje fibers [40], [42], [43]. The first phase of cardiac electrical activation is the spread of the depolarization wave through the atria, followed by atrial contraction. The triggering stimulus originates in the SA, a cluster of cells in the right atrium that show autorhythmicity properties i.e., they spontaneously depolarize and initiate an electrical impulse in the absence of an external electric stimulation [40]. After atria depolarization, the impulse stimulates specialized conduction tissues in the AV, located in the interatrial septum. This AV junction slows down the impulse propagation and allows to complete the atrial contraction before proceeding towards the ventricles. The signal is then conducted through the His-Purkinje system, which rapidly transmits depolarization wavefronts to the right and left ventricular myocardium. The main left bundle bifurcates into two primary subdivisions, a left anterior fascicle and a left posterior fascicle

[40]. The depolarization wavefronts then spread through the ventricular wall, from endocardium to epicardium, triggering ventricular contraction and enabling blood-pumping.

Working myocardium. As opposed to the cardiac conduction system which enables fast conduction of the impulse, other cardiac cells are mainly responsible for mechanical contraction and are therefore called *working myocardium*. Once the electrical signal reaches these regions, cardiac cells are excited and the contraction process is activated. The coordinated contraction of the myocardium is the result of the rapid propagation of the electrical signals through the working myocardium and the strong cohesion between adjacent cells which allows a proper force transmission. These properties are both possible by the electromechanical coupling between adjacent cardiac cells and the fiber-like arrangement of the myocardium. Remarkably, any discontinuity or non-uniformity of this anisotropic cytoarchitecture may substantially compromise the heart functionality [44].

1.1.1 Cellular basics of cardiac contraction

At a cellular level, cardiomyocytes (CMs) represent the primary working cell type responsible for heart contraction. CMs are individual striated, branching, mononucleated cells, responsible for both conduction of electrical impulses and mechanical contraction. Each cell is around 60–140 μm in length and 17–25 μm in diameter [40]; it contains contractile filaments, called myofibrils, organized into serially repeating structures, the sarcomeres. This regular organization is responsible for the striped or striated appearance that cardiac muscle cells show under a microscope. The cytoplasm contains other cell constituents, including the single centrally located nucleus, numerous mitochondria, and the intracellular membrane system, the sarcoplasmic reticulum (SR). At the interface between two adjacent cardiac cells, there is an organized structure called the intercalated disk, which enables electromechanical interaction between cells. At this location, three distinct intercellular junctional structures can be identified: (1) adherens junctions, (2) desmosomes, and (3) gap junctions [45], [46]. Adherens junctions and desmosomes play a key role in cell-cell adhesion and intercellular mechanical strength. On the contrary, gap junctions (GJ) are mainly responsible for the electrical connection between the two adjacent cells. Indeed, GJs are commonly referred to as clusters of single gap-junction-channel, which directly connect the cytoplasm of two adjacent cells, supporting the exchange of small molecules and ions [44]. The presence of electric coupling between adjacent cardiac cells through the low-resistance (high conductance) GJ is crucial for the rapid propagation of the electrical signals that trigger muscle cell contraction. Moreover, the prominence of these junctional structures at cell poles, together with the elongated shape of cardiac cells, reduce the longitudinal resistivity w.r.t. the transverse resistivity, leading to the well-established myocardium electrical anisotropy (Fig. 1.1).

Automaticity. Some CMs demonstrate automaticity properties. This biological feature is defined as the capability of cardiac cells to undergo spontaneous diastolic

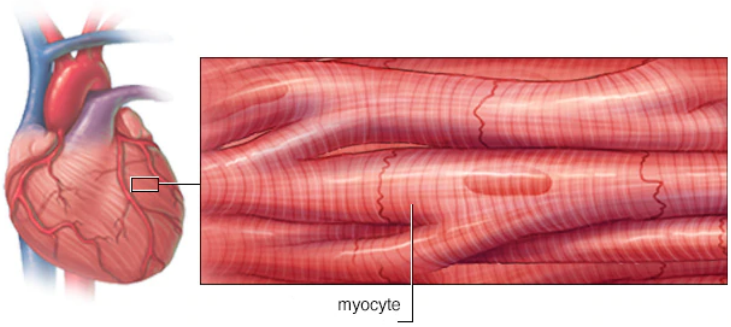

Figura 1.1: Cardiac anisotropy. *Myocytes, or cardiac muscle cells, are individual striated muscle cells joined together in a fiber-like structure. At the interface between two adjacent cells, intercalated disks enable the electromechanical coupling between them. This peculiar cytoarchitecture is responsible for the anisotropic mechanical and electrical properties of the myocardium. Reproduce from [27]*

depolarization and to initiate an electrical impulse in the absence of external electric stimulation. These spontaneously originated electrical impulses are propagated through cardiac myocytes via low-resistance intercellular connections, with active regeneration along cellular membranes [42], [43], [45]. The cells that belong to the conduction system share this automaticity property [42], [43]. Among them, the cells with the highest firing frequency act as the main pacemaker of the heart and are responsible for heartbeat initiation. Under normal conditions, the triggering stimulus for the heartbeat originates in the SA node. Indeed, even if other parts of the conduction system, such as the AV node and the His-Purkinje system, may also spontaneously fire, their firing rate is slower than SA node and thus their firing is suppressed.

Excitability. CMs are excitable cells, which means that they respond to an electrical stimulus out of proportion to the strength of that stimulus. Cell excitability is normally maintained by separation of chemical charge, which results in an electrical transmembrane potential (TMP). In CMs, this electrochemical gradient is created by differing intracellular and extracellular concentrations of sodium (Na^+) and potassium (K^+) ions. Na^+ predominates extracellularly, while K^+ ions are more concentrated intracellularly. Although this transmembrane gradient is maintained by the high chemical resistance intrinsic to the lipid bilayer of the cellular membrane, passive leakage of these ions occurs across the cellular membrane through ion channels. To compensate this passive leakage, two active transport mechanisms are used, each transporting three positive charges out of the myocyte in exchange for two positive charges that are moved intracellularly [42], [43]. The resting potential difference measured inside and outside the cardiac muscle cell in humans is between -85 and -95 mV. Occasionally the membrane potential rapidly increases and decreases following a consistent pattern in time. This event, commonly referred to as an action potential (AP), can be induced by an AP from adjacent excitable cells or from an external depolarizing impulse. In the first case, upon the activation of a CM, a positive ionic current flows through the gap-junction-channels to adjacent CMs and causes the increment of their intracellular potential. When

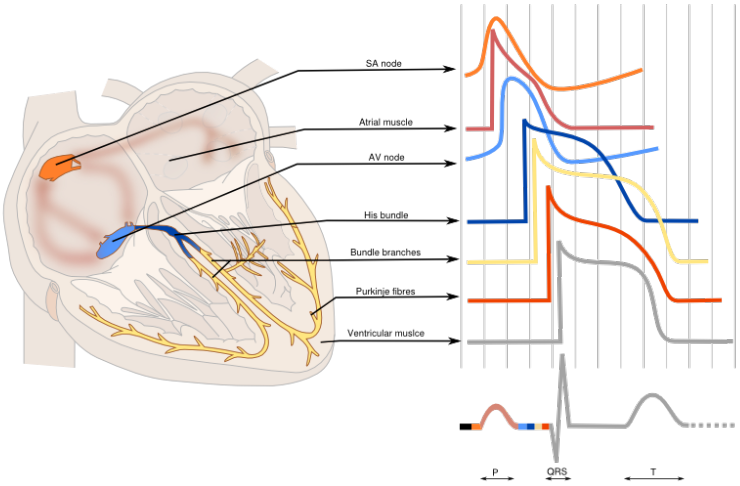

Figura 1.2: Heterogeneity of action potential waveforms. *Schematic representation of the different shapes of the cardiac action potential in the cardiac conduction system and the working myocardium. The characteristic waveform of the different parts of the conduction and working system is the result of the specific traits of the individual myocytes. Reproduced from [47].*

this depolarizing current reaches a certain threshold, a new AP is generated in the cells. In this way, the AP can propagate through the cardiac muscle in the form of an excitation wave, or activation wave.

Cardiac action potential. The AP profile is sculpted by the orchestrated activity of multiple distinctive time-dependent and voltage-dependent ionic currents. These currents are carried by complex transmembrane proteins that passively conduct ions down their electrochemical gradients through selective pores (ion channels), actively transport ions against their electrochemical gradient (pumps or transporters), or exchange of ionic species (exchangers). APs in the heart are regionally distinct due to differences in the number and types of ion channel proteins expressed by different cardiac cells (Fig. 1.2). For instance, ionic currents, that are active in pacemaking muscle cells, are unique and differ from the currents recorded in the same cell type in other regions of the heart.

Under normal conditions, the SA node is the primary pacemaker of the heart, with a resting membrane potential (RMP) of approximately 60 mV. As previously mentioned, the cardiac cells within the SA node depolarize spontaneously. This automatic depolarization occurs due to the presence of a specific ionic current, the so-called *funny current*, that periodically increases the membrane potential through a net inward flow of sodium (Na^+). When the membrane potential reaches - 40 mV, calcium (Ca^{2+}) currents (T-type $I_{Ca,T}$ and L-type $I_{Ca,L}$) are activated, and serve as the predominant ion carriers during the AP upstroke of pacemaker cells. Subsequently, outward potassium (K^+) currents are activated and Ca^{2+} currents are inactivated. The membrane potential decreases due to the outward flow of K^+ and, upon reaching the RMP, the cycle is reinitiated [48].

As opposed to SA node, working CMs do not undergo a spontaneous depolarization but can be excited by adjacent cells through the inflow of positive charges

across GJ channels. This depolarizing current increases the membrane voltage of working CMs from its resting value of - 90 mV. When the TMP of a cardiac muscle cell reaches the threshold for the activation of voltage-gated sodium channels (approximately - 65 mV), these channels modify their conformation from an inactive to an active state, allowing the abrupt influx of extracellular Na^+ ions into the myocyte and the TMP rapidly raises to approximately +20 mV [49], [50]. This fast upstroke creates a short period of overshoot potential (phase 0), which in turn activates an outwardly directed potassium (K^+) current that initiates the repolarization of the cell (phase 1) [51]. In the meantime, an inward calcium (Ca^{2+}) current is also elicited through voltage-dependent calcium channels. Potassium and calcium currents counterbalance themselves and determine the characteristic plateau phase in the cardiac AP (phase 2). Remarkably, the aforementioned inward calcium current is critical to activate the mechanical contraction of CMs. Below a certain potential, the voltage-gated calcium channels are inactivated (phase 3) and the outward potassium currents repolarize the membrane potential of CMs to a normal diastolic RMP (Fig. 1.3a). In human CMs, a complete cycle is typically performed in 200-300 ms [40].

During this time period, the ability of the CMs to respond to another stimulus depends on the time that elapsed since the previous depolarization. Four states of refractoriness can be identified throughout the AP: (1) absolute refractory period (ARP) or effective refractory period (ERP), which is the period during which whatever electrical stimulus cannot elicit an AP because the membrane is not sufficiently repolarized and sodium channels have not completely recovered from the inactivated state; (2) relative refractory period (RRP), which requires a stimulus larger than in case (1) to initiate an AP; (3) supernormal period (SNP), during which the threshold is lower than typically required to generate an AP; and (4) normal excitability (Fig. 1.3b).

Excitation–contraction coupling. The contraction of a cardiac myocyte is governed primarily by intracellular calcium (Ca^{2+}) concentration. Ca^{2+} enters the cell during the plateau phase of the AP through the L-type Ca^{2+} channels (see Paragraph 1.1.1) that line areas of specialized invaginations known as transverse tubules (T-tubules). Although the rise in intracellular Ca^{2+} is small and not sufficient to induce contraction, the small amount of Ca^{2+} entering the cell via $I_{Ca,L}$ triggers a massive release of Ca^{2+} from the SR (the major store for Ca^{2+}) into the cytosol by opening the ryanodine receptor 2 (RyR_2) channels (present in the membrane of the SR) in a process known as calcium-induced calcium release (Fig. 1.4). The combination of Ca^{2+} influx and release raises the free cytosolic Ca^{2+} levels. The free Ca^{2+} binds to myofilament protein troponin C, leading to a conformational change in the troponin-tropomyosin complex. This conformational change causes the exposure of an active site on the actin molecule, responsible for binding the myosin adenosine triphosphatase (ATPase) located on the myosin head. This bond results in adenosine triphosphate (ATP) hydrolysis, which in turn supplies energy for a conformational change in the actin-myosin complex. The principal outcome is that actin and myosin filaments slide past each other, shortening the sarcomere length. These ratcheting cycles continue to occur as long as

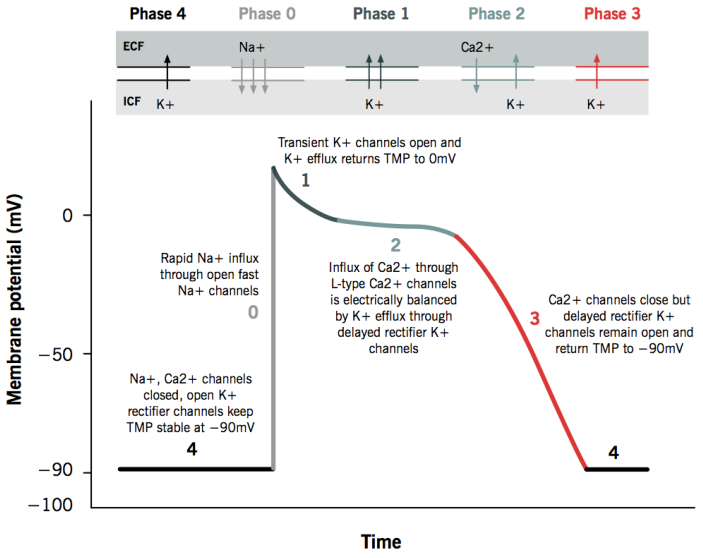

(a)

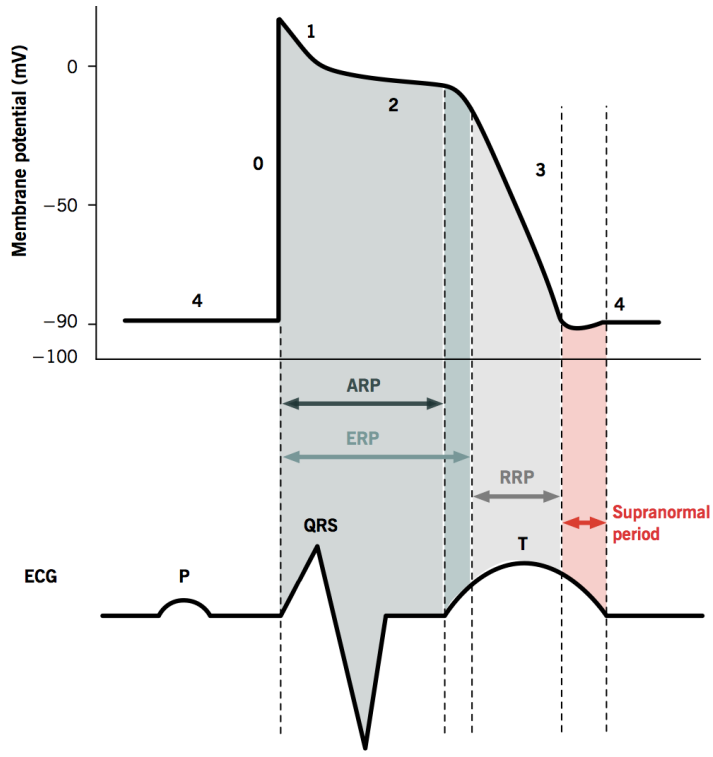

(b)

Figura 1.3: Cardiac action potential. *(a) The figure shows the cardiac action potential (AP) and the respective sequence of ion channel activities. Phase 0 represents the fast opening of voltage gated sodium channels and the influx of sodium ions. Transmembrane potential (TMP) is raised by almost 100 mV from a mean resting potential of - 90 mV to 10 mV. In Phase 1, a small amount of potassium channels is opened and TMP is brought to ± 0 mV. Voltage-gated calcium channels are opened in phase 2 of the AP leading to a calcium-induced calcium release. This enables CMs for contraction. Phase 3 resembles the depolarization of CMs by opening delayed rectifying potassium channels bringing the cell to a resting TMP of - 90 mV. (b) Cardiac AP and refractory period can be classified as: (1) absolute refractory period (ARP) or effective refractory period (ERP); (2) relative refractory period (RRP); (3) supernormal period (SNP). Normal excitability (4) exists outside of the total refractory period. Reproduce from [52].*

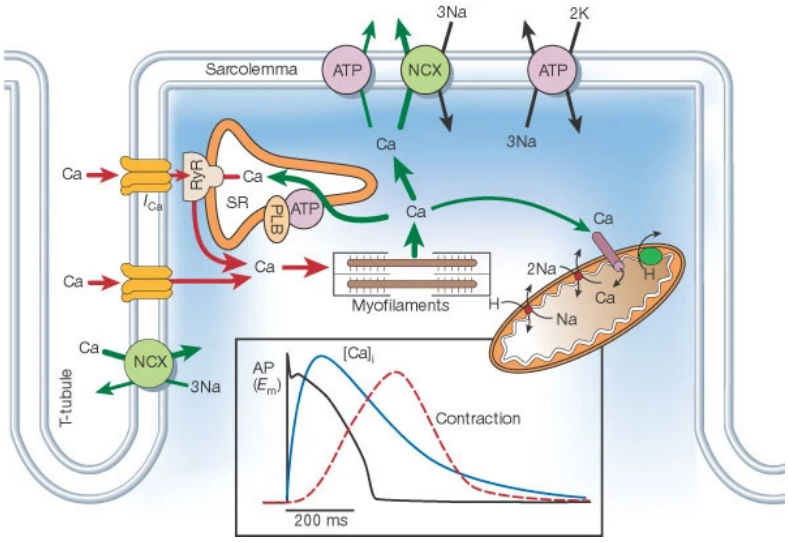

Figura 1.4: Cardiac excitation–contraction coupling. *Inset: Diagram showing the relationship between the time course of transmembrane action potential (AP), Ca^{2+} transient, and the contractile response in a ventricular muscle cell. NCX = Na^+/Ca^{2+} exchange; ATP = ATPase; PLB = phospholamban; SR = sarcoplasmic reticulum. Reproduce from [13]*

cytosolic Ca^{2+} levels remain elevated. When intracellular Ca^{2+} levels decline, Ca^{2+} dissociates from troponin C and relaxation occurs. The decrease of cytosolic Ca^{2+} concentration requires Ca^{2+} transport out of the cytosol by four pathways involving SR Ca^{2+}-ATPase, sarcolemmal Na^+/Ca^{2+} exchange, sarcolemmal Ca^{2+}-ATPase or mitochondrial Ca^{2+} uniport. [40], [42], [43].

1.2 Cardiac arrhythmias

Cardiac arrhythmia is a form of irregularity in heart rhythm and, in some cases, results in heart disease, which poses serious threats to human lives. Arrhythmias affect millions of people and are associated with substantial morbidity and economic costs. Besides some arrhythmias are not particularly dangerous, others may be indicative of structural heart disease or predispose to complications such as stroke and cardiac arrest [53], [54].

1.2.1 Classification

Cardiac arrhythmias refer to any abnormality or disturbance in the normal activation sequence of the myocardium and can be classified by rate (tachycardia, bradycardia), mechanism (automaticity, re-entry, triggered), duration (isolated premature beats, couplets, runs), or site of origin (supraventricular, ventricular) [54].

Supraventricular Tachycardias

Supraventricular tachycardia is a broad term which includes different forms of arrhythmia originating above the ventricles (supraventricular) in the atria or AV node. These arrhythmias have been seen to cause sudden episodes of irregular heartbeats that begin and end abruptly. Supraventricular tachycardia occurs when faulty electrical connections in the heart or abnormal areas of electrical activity trigger and sustain an abnormal rhythm. When this happens, the heart rate accelerates too quickly and doesn't allow enough time for the heart to fill before it contracts again and the stroke volume might be insufficient to properly oxygenate body organs. Supraventricular tachycardia includes: (1) atrioventricular junctional tachycardias, which in turn comprehend atrioventricular nodal re-entrant tachycardia and non-re-entrant junctional tachycardia; (2) atrioventricular re-entrant tachycardia, which use an anatomically defined re-entrant circuit that consists of a physiological and an accessory pathway; and (3) atrial tachycardia, such as sinus tachycardia, atrial fibrillation (AF), focal atrial tachycardia and multifocal atrial tachycardia [55].

Ventricular arrhythmias

Ventricular arrhythmias include a broad spectrum that ranges from premature ventricular complex to ventricular fibrillation (VF), respectively with a different clinical presentation that ranges from a total lack of symptoms to cardiac arrest. Most life-threatening ventricular arrhythmias are associated with ischemic heart disease, particularly in older patients. The risks of ventricular arrhythmias and SCD vary in specific populations with different underlying cardiac conditions, and with specific family history and genetic variants, and this variation has important implications for studying and applying therapies [56].

Tabella 1.1: *Mechanism of cardiac arrhythmias*

Disorders of Impulse Formation	Disorders of Impulse Conduction
Automaticity	*Reentry*
Altered normal automaticity	Anatomic reentry
Abnormal automaticity	Functional reentry
Triggered activity	
Delayed afterdepolarization	
Early afterdepolarization	

Bradycardia

Bradyarrhythmias occur if the heart rate is slower than normal. If the heart rate is too slow, not enough blood reaches the brain. This reduction in blood perfusion can ultimately lead to death. Generally, in adults, a heart rate slower than 60 beats per minute is considered a bradyarrhythmia, however, some people (e.g., athletes) normally have slow heart rates thereby 60 beats per minute might be not dangerous. Bradyarrhythmias can be caused by heart attacks or other conditions that harm or change the heart's electrical activity.

Bradycardia can be broadly classified into 2 general categories: (1) sinus node dysfunction and (2) atrioventricular block [57].

1.2.2 Electrophysiological mechanisms

The mechanisms responsible for cardiac arrhythmias may be divided into disorders of impulse formation, disorders of impulse conduction, or a combination of both (Fig. 1.5). Among disorders of impulse formation, arrhythmia can originate from abnormal or enhanced automaticity and triggered activity. Disorders of impulse conduction, instead, include anatomic or functional re-entry mechanisms [58]–[60].

Automaticity

Arrythmic mechanism linked to automaticity can be classified as altered normal automaticity or abnormal automaticity, where electrical activity is elicited by non-pacemaker cells.

Altered normal automaticity. As previously mentioned (see Paragraph 1.1), some specialized heart cells possess the property of pacemaker activity or automaticity. Under normal conditions, the SA nodal cells have the fastest rate of firing among the pacemaker cells of the cardiac conduction system and, thereby, the "subsidiary" pacemaker cells, which fire spontaneously at slower rates, do not trigger the heart depolarization. Any alteration in the rate of impulse initiation can disrupt the hierarchic activation of the heart from SA node to ventricles. In other terms, enhancement or suppression of this activity may lead to clinical arrhythmias [61]. Enhanced automaticity of pacemaker cells can increase the rate of AP discharge. When this occurs in the SA node, it can lead to an increase in heart rate, termed

sinus tachycardia. This can be physiological, due to increased sympathetic tone during exercise, or pathophysiological, due to hypovolemia, ischemia, or electrolyte disturbances. Suppression of the sinus automaticity, instead, results in sinus bradycardia or even sinus arrest, which in turns enables a subsidiary pacemaker cell (i.e., another pacemaker cell of cardiac conduction system) to manifest its own rhythm, without being suppressed by the physiological faster firing rate of SA node (Fig. 1.5).

Abnormal automaticity. Atrial and ventricular non-pacemaker myocardial cells, which in the normal heart typically do not exhibit spontaneous activity, may exhibit automaticity properties. This can happen under conditions that drive the maximum diastolic potential towards the threshold potential.

Triggered Activity

Triggered activity is defined by impulse initiation caused by oscillations of membrane potential, named early or delayed after-depolarizations [62].

Early after-depolarizations. Early after-depolarizations (EADs) are associated with an increased AP duration (APD) causing long QT syndrome (Fig. 1.5). APD prolongation is commonly caused by the presence of altered net inward currents ($I_{Ca,L}$, I_{NCX}). Noticeably, repolarizing ion channels can be altered by both genetic mutations and drug interactions, which in turn results respectively into congenital long QT[1] and acquired long QT. EAD-triggered ventricular tachycardia is polymorphic and is commonly referred to as Torsade de Pointes [63].

Delayed after-depolarizations. Delayed after-depolarizations (DADs) usually occur when Ca^{2+} in the SR is elevated (Fig. 1.5). During diastole, this condition triggers calcium leakage into the myoplasm. As a consequence, the Na^{+}/Ca^{2+} exchanger pushes out elevated diastolic Ca^{2+} from the cell in exchange for Na^{+} (1 Ca^{2+} for 3 Na^{+}), finally resulting in a net inward current, that elicits DADs [63].

Reentry

During the normal electrical activity, the trigger signal is elicited by the SA node and propagates throughout the heart until the entire tissue is activated. This impulse dies out when all fibers have been depolarized and are completely refractory. Nevertheless, if a group of isolated fibers is not activated during the initial wave of depolarization, this bunch of cardiac fibers can recover excitability in time to be depolarized before the impulse dies out. This excitable area may serve as a link to re-excite areas, that were previously depolarized, but have already recovered from the initial depolarization. Such a process is commonly denoted as reentry, referring to a repetitive propagation of the wave of activation, returning to its site of origin to reactivate that site. Reentry is the most common arrhythmia

[1]The QT interval represents the duration of ventricular electric systole, it is measured from the beginning of the QRS complex to the end of the T-wave in the electrocardiogram.

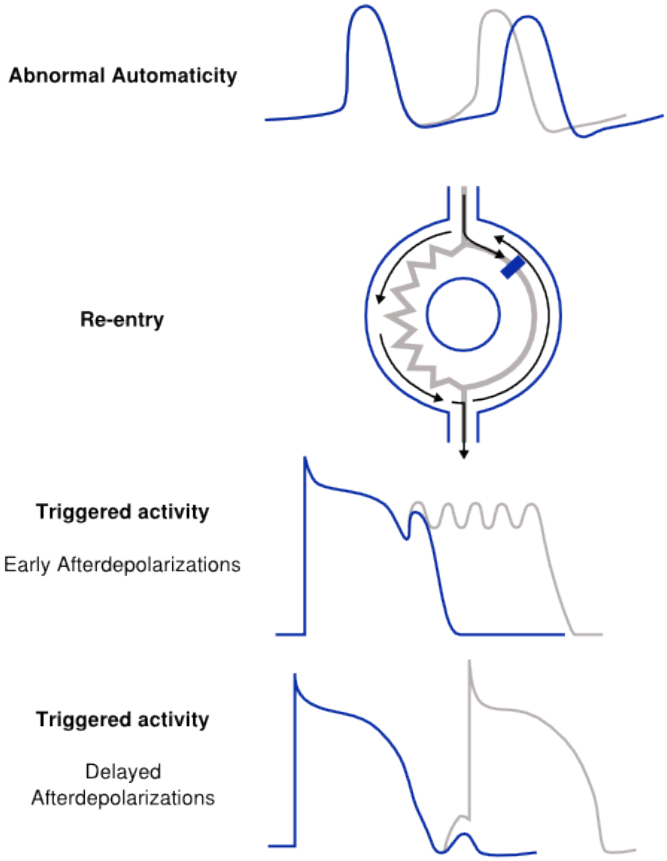

Figura 1.5: ***Mechanism of cardiac arrhythmias.*** *Reproduce from [47]*

mechanism seen in clinics, both in classical or variant forms [59]. A key concept of this type of reentry is the presence of an excitable gap, i.e., an excitable region of myocardium that exists between the head of the reentrant wavefront and the tail of the preceding wavefront [64]. This excitable gap allows the reentrant wavefront to continue propagation around the circuit. Remarkably, the presence of this excitable gap also makes it possible to enter in the reentrant circuit using external pacing and explains the phenomena of resetting, entrainment, and termination of the tachycardia with electrical stimulation.

Two major categories of reentry have been identified: anatomical reentry and functional reentry [59].

Anatomical reentry. The classic reentry mechanism is based on a non-excitable anatomical obstacle (e.g. scar tissue following myocardium infarction) surrounded by a circular pathway in which the wavefront can reenter, creating fixed and stable reentrant circuits. When a wavefront encounters an anatomical obstacle, it can conquer the obstacle to its right or to its left (Fig. 1.5). If there is a point of block down a pathway, the electrical signals stop at that point (unidirectional block), leaving an excitable region below this point. The wavefront that has traveled down the opposite pathway can reenter this way, initiating a reentrant circuit. Initiation and maintenance of reentry will depend on the conduction velocity and refractory

period of each pathway, which determine the wavelength value (wavelength equals to the product between conduction velocity and refractory period). For reentry to occur, the wavelength must be shorter than the length of the pathway. Thereby, conditions that decrease conduction velocity or shorten the refractory period will facilitate the initiation and maintenance of reentry.

Functional reentry. In functional reentry, the circuit is not determined by anatomic obstacles; it is defined by dynamic heterogeneities in the electrophysiologic properties of the myocardium. The location and size of functional reentrant circuits can vary, but they are usually small and unstable. Functional reentry includes leading circle reentry [65], anisotropic reentry [64], [66], spiral wave or rotors [67] and reflection [59].

1.2.3 Current treatments

Not all arrhythmias need to be treated. Usually, only those patients who present significant symptoms or are at high risk of complications receive medical care. Common arrhythmia treatments include medicines, medical procedures, and surgery.

Medicines. Antiarrhythmic drugs are usually the first treatment options for abnormal heart rhythm. The most common medicines that are used to slow a fast heart rate are beta-blockers, calcium channel blockers. Remarkably, at the moment, no drug can reliably speed up a slow heart rate, and thereby abnormally slow heart rates need to be treated with pacemakers [27]. Besides restoring a steady heart rhythm, medicines are also used to avoid complications of arrhythmias. For instance, blood-thinning medicines are commonly used by people who suffer from AF to reduce the risk of blood clots forming.

Medical procedures. Certain types of supraventricular arrhythmias can be stopped by using particular maneuvers that include holding the breath and straining, dunking the face in ice water, or coughing. These maneuvers are generally called vagal maneuvers because they affect the vagus nerve, which helps control the heart rate and often cause the heart rate to slow.

Another common treatment is cardiac ablation. This technique works by scarring or destroying tissue in the heart that triggers or sustains an abnormal heart rhythm. Cardiac ablation usually uses long, flexible catheters inserted through a vein or artery in the groin and threaded to the heart to deliver energy in the form of heat or extreme cold. Cardiac ablation can be done through open-heart surgery, but the use of catheters is commonly preferred since it makes the procedure less invasive and shortens the recovery time. This procedure is a treatment option only for those kinds of arrhythmias that can be effectively treated by ablation of a certain tissue region, such as Wolff-Parkinson-White syndrome.

Some arrhythmias, that cannot be successfully treated by medications and that do not respond well to cardiac ablation, require the implantation of a cardiac pacemaker or an ICD. Both these devices are implanted in the chest or abdomen

and help control abnormal heart rhythms. A pacemaker uses electrical pulses to prompt the heart to beat at a normal rate. It can speed up a slow heart rhythm, control a fast heart rhythm, and coordinate the chambers of the heart. Basically, if your heart rate is too slow or if it stops, the pacemaker sends out electrical impulses that stimulate your heart to beat at a steady rate. An ICD, instead, senses dangerous rhythms and delivers electrical shocks to restore the heartbeat. This type of treatment is called cardioversion or defibrillation, depending on which type of arrhythmia is being treated. The ICDs are of extreme relevance in controlling life-threatening arrhythmias, especially for those patients who are at high risk of sudden cardiac arrest. Most new ICDs can act as both a pacemaker and a defibrillator.

Surgery or other procedures. Some arrhythmias can also be treated with surgery, especially if the operation is already being done for another reason, such as the repair of a heart valve. One type of surgery for AF is called maze surgery. During this surgery, a surgeon makes small cuts or burns in the atria. Since scar tissue doesn't conduct electricity, these cuts or burns prevent the spread of disorganized electrical signals. If arrhythmia is caused by coronary heart disease, coronary artery bypass grafting might be suggested to improves blood flow to the heart muscle and, thus, reduce the risk of abnormal rhythm onset.

1.3 Electrical stimulation

1.3.1 Historical background

The use of electrical stimulation to elicit artificial cardiac pacing and defibrillation dates back to 1958, when John Hopps found that if the heart stops beating it could be restarted artificially using mechanical or electrical stimulation. The pioneering research of this canadian electrical engineer allowed the development of the first cardiac defibrillation machine. The system was used by Hopps in 1949 to start a dog's heart and, almost one year later, in a human being. Unfortunately, the size of this preliminary device was still too large to be used internally and it took almost ten years to obtain the first implantable cardiac pacemaker [68]. At that time, while cardiac pacing was joyfully achieved, life-threatening ventricular arrhythmias were still treated using only anti-arrhythmic drugs. The concept of an implantable defibrillator to prevent sudden arrhythmic death was first published by Michel Mirowski in 1970 [69]. Despite concerns by the scientific community, Michel Mirowski continued the development of his vision, upon the first defibrillator successfully implanted in a 57-year-old woman in 1980 [70], which preceded the US Food and Drug Administration approval in 1985.

1.3.2 Basic principle

Direct electrical stimulation of excitable cardiac tissue causes a change in the TMP of cardiac cells. If the TMP is raised to a certain level, an AP is initiated in the cells and spreads to adjacent working myocardial cells. Isolated myocytes can be electrically stimulated in two ways: (1) direct transmembrane current injection with a microelectrode, or (2) external field stimulation. Common implantable devices, for both cardiac pacing or defibrillation, stimulate CMs by external field stimulation. To this end, all defibrillator and pacemaker electric circuits have both a positively charged electrode (the anode) and a negatively charged electrode (the cathode). The negatively charged cathode is typically the tip electrode on a pacing lead. Electrons from the pulse generator flow through the cathode-tissue interface and return to the anode, which may be located on a pacing lead or the pulse generator casing. When an electric field is applied in a certain region, current flows from one electrode to another, but only little current enters the cells due to the relatively high impedance of the cell membrane compared with the impedance of the extracellular space and the small cell length [71].

The effect of electric stimulation might be explained considering a single cell immersed in an electric field. In this context, it can be assumed that the intracellular voltage (V_i) does not change appreciably from one end of the cell to the other. On the contrary, the extracellular voltage (V_e) drops linearly over the cell length due to the applied external electric field. As a result, the TMP ($V_m = V_i - V_e$) also changes along the cell length as a linear function (Fig. 1.6) with hyperpolarization and depolarization at the cell ends facing the anode and cathode, respectively. Positive polarization can result in the prolongation (if the cell was refractory) or activation (if the cell was excitable) of an AP. Negative polarization, which hyperpolarizes or repolarizes the cell, abbreviates the AP and eventually lead to *deexcitation*, i.e., the

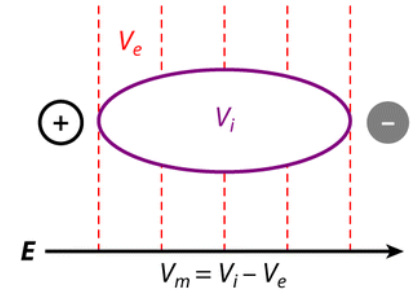

(a)

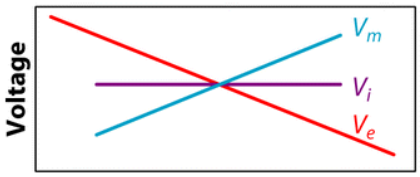

(b)

Figura 1.6: Electrical stimulation: single cell response to electric fields. *V_m response in a single cell to an electric field. (a) Schematic of an elongated cell in an electric field. An electric field (E) creates a gradient of extracellular potential (V_e). Dashed lines indicate isopotential lines. Because of the relatively high impedance of the cell membrane and the short cell length, negligible amounts of current pass through the membrane, and the intracellular voltage (V_i) remains nearly constant throughout the cell. (b) Spatial profiles of V_e, V_i, and TMP (V_m) along the cell. Reproduce from [72]*

negative polarization is strong enough to abolish the AP and restore excitability. When V_m in the depolarized section of the cell reaches the activation threshold, a sufficient number of ion channels are opened and an AP is generated. This AP then spreads to adjacent cells by the means of ionic currents through GJs and raising V_m in adjacent cells, thus initiating an active response through the activation of Na^+ channels [58], [72], [73].

Even if the response of a single cell to an electric field is straightforward, cardiac cells are not isolated cells that respond independently from the surrounding tissue. GJs between cells, collagenous septae, tissue orientation, fiber curvature, and other factors may alter the response of a single cell to an electric field [58], [72], [73]. Nevertheless, the basic principle of the electrical stimulation remains the same: the transmembrane voltage of a group of myocytes raises above a threshold, leading to the generation of an AP. This stimulus then propagates to nearby myocytes and trigger depolarization of those membranes. The result is a self-regenerating AP that progresses in a wavelike beyond the local effect of the device-induced stimulus.

Stimulation threshold. Myocardial stimulation threshold for pacing is defined as the minimum stimulus amplitude at any given pulse width required to consistently achieve myocardial depolarization outside the heart's refractory period. The stimulation threshold can be expressed as a function of current density (A/cm^2) at the stimulating electrode or the magnitude of the electric field gradient (V/cm in viable tissue) that is induced in the myocardium beneath the stimulating electrode.

The stimulus is defined by the pulse amplitude and the pulse duration. An exponential relationship exists between the stimulus amplitude and the duration, resulting in a hyperbolic strength–duration curve. When pulse are short, a small change in the pulse width is associated with a significant change in the pulse amplitude required to achieve myocardial depolarization; conversely, when long pulse are applied, a small change in pulse duration has relatively little effect on threshold amplitude. On the strength–duration curve two crucial points can be identified: the rheobase and the chronaxie. The former is defined as the smallest amplitude (voltage) that stimulates the myocardium at an infinitely long pulse duration (ms). The chronaxie, instead, is the threshold pulse duration at twice the stimulus amplitude, which is twice the rheobase voltage. The chronaxie is important in the clinical practice of pacing because it approximates the point of minimum threshold energy (μJ) required for myocardial depolarization (Fig. 1.7). Note that with the magnitude of a stimulus generated by a pacemaker pulse generator, the electric field gradient and ion current density near the electrode are great enough to trigger an AP only extremely close to the electrode. Cardiac contraction results from the propagation of this local depolarization through the conduction system, towards the myocardium. In contrast to cardiac pacing, defibrillation needs to produce depolarization over major portions of the myocardium and therefore it involves a high-energy stimulation able to provide a much wider local voltage gradient.

Unipolar or bipolar. In unipolar pacing systems, the lead tip functions as the cathode, and the pulse generator functions as the anode. In bipolar systems, instead, the lead tip functions as the cathode, and the lead ring functions as the anode (Fig. 1.8). Noticeable, the pacemaker canister is in contact with the pectoralis major muscle at the pacemaker pocket floor. Despite the large surface area of the anode, sometimes the current density can increase above the capture threshold of the pectoralis major muscle and cause contractions in the pocket during unipolar pacing, especially when high outputs are used. On the contrary, in bipolar systems, the ring electrode acts as the anode and since there is no issue in muscle capture, the ring electrode has a small geometric surface [74]. There are long-standing controversies regarding unipolar and bipolar configurations and which one, if either, is superior. However, the bipolar configuration is generally preferred over unipolar. This is firstly due to the fact that bipolar pacing cannot cause extracardiac stimulation at the pulse generator, which may occasionally occur with unipolar pacing due to current returning to the generator. Moreover, bipolar sensing is less likely to detect myopotentials, far-field signals, and electromagnetic interference, which lead to a more accurate sensing process.

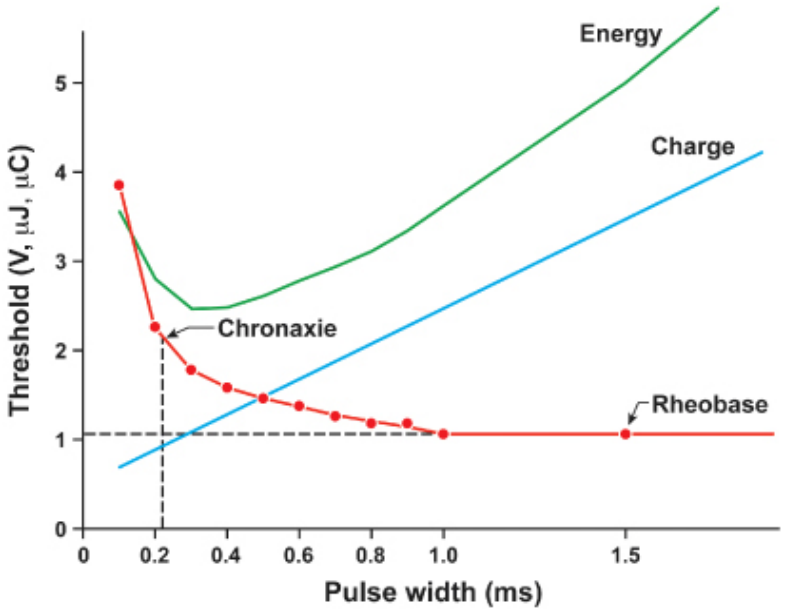

Figura 1.7: Electrical stimulation: strength–duration curve. *Relationship of charge, energy, voltage, and current to pulse duration. Relationships among chronic ventricular strength–duration curves from a canine, expressed as potential (V), charge (μC), and energy (μJ). Rheobase is the threshold at infinitely long pulse duration. Chronaxie is the pulse duration at twice rheobase. Reproduce from [58], [75]*

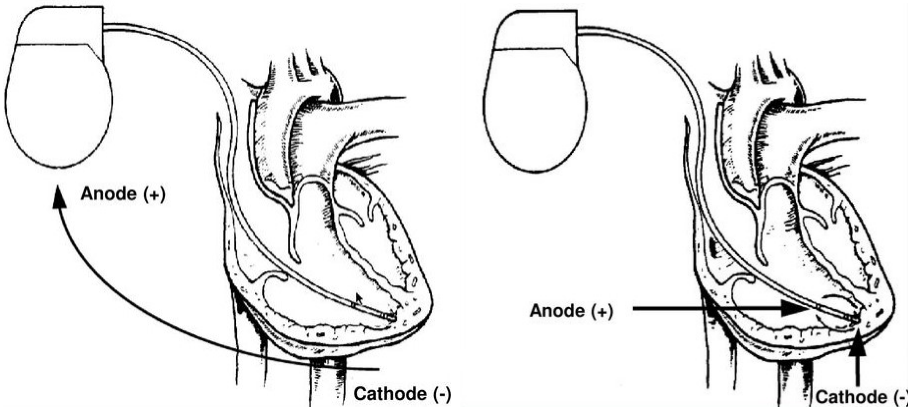

(a) *Unipolar* **(b)** *Bipolar*

Figura 1.8: Electrical stimulation: unipolar and bipolar configurations. *(a) In a unipolar configuration, the case serves as the anode, or (+), and the electrode lead tip as the cathode, or (–). In other terms, unipolar configuration consists only of one channel which would deliver the electrical impulse to the myocardium and the circuit would be completed by the chest wall tissues which are in contact with the metal device canister, which represents the anode. (b) In a bipolar configuration, instead, the anode is located on the ring electrode, proximal to the tip, or cathode. Thereby, bipolar leads consist of two electrical channels encased in an insulating material: one channel would conduct the electrical impulse towards the lead tip and the other channel would complete the circuit back to the device. The distance between the tip and the ring electrode varies among manufacturers and models. Reproduce from [76]*

1.3.3 Cardiac pacing

A pacemaker is a small device that's placed in the chest or abdomen to help control abnormal heart rhythms. Pacemakers use low-energy electrical pulses to prompt the heart to beat at a normal rate and overcome the faulty electrical signaling commonly related to cardiac arrhythmias.
The device can be temporary or permanent. Temporary pacemakers are used in hospital to treat short-term heart problems, such as a slow heartbeat that's caused by a heart attack, heart surgery, or an overdose of medicine. Permanent pacemakers, instead, are used to control long-term heart rhythm problems.
Despite the first pacemakers functioned as fixed-rate devices, nowadays pacemakers can be programmed as demand pacing and rate-responsive pacing. A demand pacemaker monitors the heart rhythm and only sends electrical pulses if the heartbeat is too slow or if the heart misses a beat. A rate-responsive pacemaker will speed up or slow down the heart rate depending on how the patient is active. For such devices to function as programmed, accurate, and consistent sensing of the native rhythm is essential. Indeed, the device monitors the sinus node rate, breathing, blood temperature, and other factors to determine the activity level.

Working mechanism

A pacemaker consists of a battery, a computerized generator, and wires with sensing electrodes at their tips. The battery powers the generator, and both are surrounded by a thin metal box. The wires, instead, connect the generator to the heart. At this level, the electrodes detect the heart's electrical activity and send data through the wires to the computer in the generator. If the heart rhythm is abnormal, the processor will direct the generator to send electrical pulses to the heart.
Artificial pacing involves delivery of an electrical impulse from an electrode of sufficient strength to cause depolarization of the myocardium in contact with that electrode. The minimal amount of energy required to produce this depolarization is called the stimulation threshold. Once the AP is elicited, it propagates into electrically coupled adjacent cells and finally triggers a heartbeat.
Commonly, pacemakers have one to three wires that are each placed in different chambers of the heart:

1. The wires in a single-chamber pacemaker usually carry pulses from the generator to the right ventricle.

2. The wires in a dual-chamber pacemaker carry pulses from the generator to the right atrium and the right ventricle. The pulses help coordinate the timing of these two chambers' contractions.

3. The wires in a biventricular pacemaker carry pulses from the generator to an atrium and both ventricles. The pulses help coordinate electrical signaling between the two ventricles. Also, this type of pacemaker is called a cardiac resynchronization therapy device since it allows to coordinate the contraction of both ventricles.

Clinical indication

Pacemakers can be used for several reasons, but the most common ones are bradycardia and heart block. In bradycardia, the heartbeat is slower than normal and the pacemakers can speed up the slow heart rhythm. In case of heart block, instead, the electrical signal is slowed or disrupted as it moves through the heart. This condition can occur as a result of aging, damage to the heart from a heart attack, or other conditions that disrupt the heart's electrical activity. Here, a pacemaker can be used to coordinate the electrical signaling between the upper and lower chambers of the heart. Other conditions might support the use of a pacemaker. A pacemaker can also help monitor the ventricle contraction in case of AF, where the atria are quivering instead of beating with a normal rhythm. Doctors also may recommend pacemakers for people who have certain types of congenital heart disease or for people who have had heart transplants.

Concerning issues

Despite the success of these medical innovations, nowadays there is a growing demand, not only to improve overall patients' mortality and safety, but also to improve patient quality of life. Pacemaker implantation causes anxiety disorders and depression in patients up to the first month [77]. Once a pacemaker is implanted, the patient has to avoid close or prolonged contact with electrical devices or devices that have strong magnetic fields, since these devices can disrupt the electrical signaling of the device and stop it from working properly.
Additionally, possible complications can come out if wires get dislodged or broken or the battery gets weak or fails. To overcome this latter case, the generator should be replaced along with the battery after 5-15 years, before the battery starts to run down. Replacing the generator and battery is less-involved surgery than the original surgery to implant the pacemaker, but it seems to be associated with higher risks of infections [2], [78].

1.3.4 Cardiac defibrillation

In the 1940s, Gurvich and Yuniev predicted that electric shocks led to premature tissue stimulation in advance of propagating wavefronts, preventing continued progression of the wavefront and, thus, able to terminate cardiac arrhythmias [79]. This discovery laid the groundwork for many of the researches that followed towards the development of medical devices that restore a normal heartbeat by sending an electric pulse or shock to the heart.
Different types of defibrillators work in different ways. Automated external defibrillators, which are in many public spaces, were developed to provide immediate support to people, which are experiencing life-threatening arrhythmias and might be not able to reach the hospital in time to survive. For those patients who are at high risk of these kinds of life-threatening arrhythmias, a personal device might be preferable. To this end, ICDs placed inside the chest with transvenous leads were developed [26]. Over the last decade, a novel entirely subcutaneous implantable defibrillator (S-ICD) has been launched for specific patient populations, including

pediatric patients, those with difficult or absent venous access, and those at high risk for bacteremia such as dialysis patients [80].

Working mechanism

An ICD is a small battery-powered device able to detect irregular heartbeats and deliver electric shocks via one or more wires connected to your heart to terminate the arrhythmia and fix it. Depending on the detected problem, the ICD can be programmed for (1) low-energy pacing, i.e. a series of low-voltage electrical impulses at a fast rate to try and correct the heart rhythm; (2) cardioversion, i.e. one or more small electric shocks to try and restore the heart to a normal rhythm; (3) defibrillation protocol, i.e. larger electric shocks to restore the heart to a normal rhythm. The latter can be extremely painful until the shock ends.

Antitachycardia pacing. Antitachycardia pacing has long been recognized as a way to pace-terminate certain types of arrhythmias, particularly slow monomorphic VT involving a reentry circuit. For the re-entrant circuit to perpetuate itself, the tissue immediately in front of the leading edge of the wavefront must have recovered excitability so that it can be depolarized. In other terms, an excitable gap of tissue must be present in advance of the leading tachycardia wavefront or the arrhythmia will terminate. According to this principle, ATP can terminate VT by depolarizing the tissue in the excitable gap, so that the tissue in front of the advancing wavefront becomes refractory and prevent further arrhythmia propagation. The ability of a train of impulses to travel to the site of the re-entrant circuit and interrupt VT depends on the site of pacing, the size of the excitable gap, and the length of the tachycardia cycle [81].

Cardioversion. Synchronized cardioversion is performed on patients that still have a pulse, but are hemodynamically unstable. All tachycardic rhythms, whether wide (ventricular) or narrow (supraventricular) QRS complex, are considered to be unstable if the patient also has chest pain, dyspnea, altered mental status, hypotension, pulmonary edema, or ischemic changes on the electrocardiogram (ECG). Thereby, synchronized cardioversion is used to treat both hemodynamically unstable ventricular and supraventricular rhythms [82]. In synchronized electrical cardioversion, a therapeutic dose of electric current is given to the heart at a specific moment in the cardiac cycle, restoring the activity of the electrical conduction system of the heart. A synchronizing function allows the cardioverter to deliver a reversion shock at the optimal moment in the cardiac cycle, which corresponds to the R-wave of the QRS complex on the ECG. Timing the shock to the R-wave prevents the delivery of the shock during the vulnerable period (or relative refractory period) of the cardiac cycle, which could induce VF. The recommended energy levels used to perform synchronized cardioversion vary from 50 to 200 J. Recalling the specific energy level for a particular sub-type of unstable tachycardia is difficult, especially in an emergent situation. The safest and easiest recommendation is to start at the lowest energy level (50 J) and if the shock is unsuccessful, double the amount of energy used [82].

High-energy shock. When the detected life-threatening arrhythmia is a VF or a pulseless ventricular tachycardia, the device is programmed to proceed immediately to an unsynchronized shock, commonly referred to as defibrillation. This medical procedure uses a therapeutic dose of electric current to the heart at a random moment in the cardiac cycle and is the most effective resuscitation measure for cardiac arrest.

Despite the efforts made over the last decades in understanding the technology required for defibrillation (e.g. lead design and position, waveform selection), the basic underlying mechanism has not been definitively determined. Few contemporary theories accounting for how an electric shock terminates fibrillation have been proposed with some overlapping: (1) critical mass theory, (2) upper limit of vulnerability hypothesis and (3) virtual electrode hypothesis.

1. *Critical mass theory.* Only if the defibrillating shock renders unavailable to fibrillation a *critical mass* of myocardium, the remaining excitable tissue is insufficient to support the wandering wavelets, and the arrhythmia is terminated [83].

2. *Upper limit of vulnerability hypothesis.* In the following years, several works analyzed the electrical activation maps after failed shocks. The presence of an isoelectric interval (an electrical pause) between failed shocks and resumption of fibrillation, suggested that VF was indeed terminated by the shock and that new arrhythmias were secondarily regenerated [84], [85]. Furthermore, it was observed that VF was frequently reinitiated in the regions of lowest shock intensity. It was therefore hypothesized that shocks with potential gradients lower than a minimum critical value, termed the upper limit of vulnerability (ULV), could re-initiate fibrillation. Since at any given time during fibrillation some of myocardial regions are repolarizing and thus vulnerable, a shock with a potential gradient below a certain threshold may create a critical point at the intersection of a spatial gradation of refractoriness with a spatial gradation of the extracellular ΔV field created by the shock [86]. At this point, fibrillation can re-initiate. Conversely, a shock with a gradient above the ULV across the entire myocardium can elicit active responses, even from supposedly refractory myocardium. The principal consequence is the obtainment of effective myocardial resynchronization (Fig. 1.9) and the defibrillation protocols succeed [58], [87].

3. *Virtual electrode hypothesis.* Optical signal measurements of TMPs have demonstrated also the presence of virtual electrodes far away from the physical ones [58]. The presence of virtual electrodes seems to be essential to make defibrillation effectively in a much larger area. However, even in this case, the pattern of the virtual electrodes of hyperpolarization and depolarization zone might lead to new fibrillation events. Indeed, even though the myocardium was in phase 2 of the AP before the electrical shock (absolute refractory period), hyperpolarized regions have been seen to induce the de-excitation of the myocardium, restoring its excitability. After the shock, the high gradient of TMP caused a positive polarization to interact electrotonically with the newly formed excitable region, producing a new wavefront propagating.

These adjacent regions of positive and negative polarization help explain the mechanism of break stimulation. If the spread of subsequent excitation is rapid and does not degenerate into sustained reentry, the defibrillation is still successful; whereas if the wavefront spread is slow and rotors form via virtual electrode-induced phase singularity mechanism the defibrillation fails and a new fibrillation event occurs [73], [88]. These considerations led to the development of *critical point theory*, which suggested that critical points are formed by a combination of the field gradients and refractory tissue and that newly fibrillation events may occur at sites far from electrodes. To limit the formation of these new life-threatening arrhythmias, Efimov and coworkers proposed that an optimal biphasic waveform is better able to defibrillate because the second phase of the shock restores the TMP back toward the levels before the shock, thus obliterating the virtual electrodes and preventing the launch of an activation front after the shock in the hyperpolarized region. To be more precise, the second phase of an optimal biphasic shock reverses the virtual electrode polarization pattern in a nonlinear fashion. The de-excited hyperpolarized region is easily re-excited and completely depolarized, whereas the depolarized part of virtual electrode polarization is only partially reduced [73]. In other terms, the second phase of a biphasic shock eliminates virtual electrode polarization and homogenizes polarization (Fig. 1.10 B). This way the substrate for postshock break excitation and potential phase singularities is eliminated. However, not every biphasic shock will be able to produce this effect (Fig. 1.10 C). For instance, if the second phase energy is below a certain threshold, it will not be able to reverse hyperpolarization. Whereas, if the energy of the second phase is above a certain value, it will reverse both positive and negative polarizations, creating mirrored virtual electrode pattern with similar consequences as that of monophasic shocks, i.e., postshock reexcitation and virtual electrode-induced phase singularities (Fig. 1.10 A). [72], [73].

Clinical Indications

ICDs, first successfully implanted in a human in 1980 by Michael Mirowski [70], have long been proven to improve mortality in a number of clinical conditions causative for SCD. Remarkably, the indications for ICD have expanded greatly since Mirowski's initial pilot study. The devices were used initially in secondary prevention (i.e. with patients that have already experienced a cardiac arrest) [89]–[91] and later also in primary prevention (i.e. to patients who have not suffered a life-threatening arrhythmia) [30], [31]. Nowadays, ICDs are considered the routine treatment and they have been included in international guidelines [28], [55].

Concerning issues

While ICDs are certainly a life-saving technology, lead and device-related complications are not insignificant. Concerning issues of transvenous systems include both acute complications related to the implant procedure [33], [34] and late complications due to infection or lead malfunction [78], [92], [93]. While the absolute complication rates are low, the severity of potential complications, namely massive

intrathoracic bleeding and death, is high [94]. Parallel to these complications, ICD can induce significant psychological distress among patients. Patients' lives change after ICD implantation, and ICD recipients often live with fears related to the

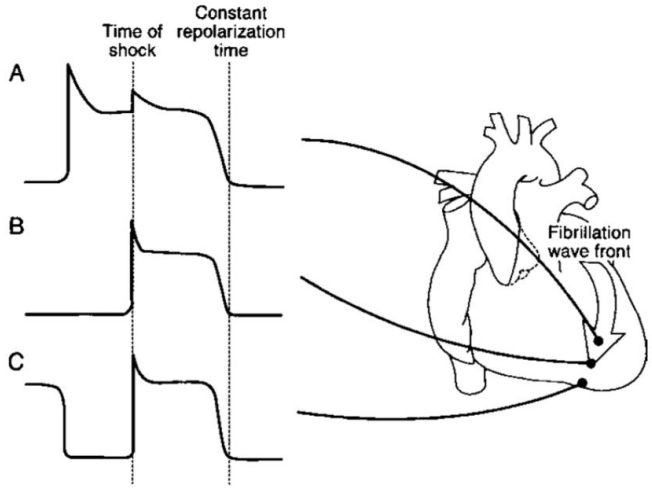

Figura 1.9: Electrical stimulation: resynchronization. *A fibrillatory wavefront is depicted by the arrow and the action potential (AP) response to a defibrillatory shock is demonstrated at three points surrounding the wavefront. The fibrillatory wavefront has just passed through a myocyte at point A when the shock is delivered. The myocyte is in its plateau (phase 2), when it would ordinarily be refractory to additional stimulation. However, when a sufficiently strong shock is delivered, the myocyte can generate an active response with prolongation of the AP and of the refractory period. The response is referred to as additional depolarization time. The tissue at point B is at the leading edge of the fibrillatory wavefront. The shock strikes this myocardium at the time of the upstroke (phase 0) and has little effect on the AP. The tissue at point C is excitable (it is the excitable gap that the fibrillatory wavefront was about to enter) when the shock is delivered. The shock elicits a new AP in this excitable tissue. Despite the different temporal and anatomical locations of the three APs depicted, after the shock, there is resynchronization by the constant repolarization time. Reproduce from [58]*

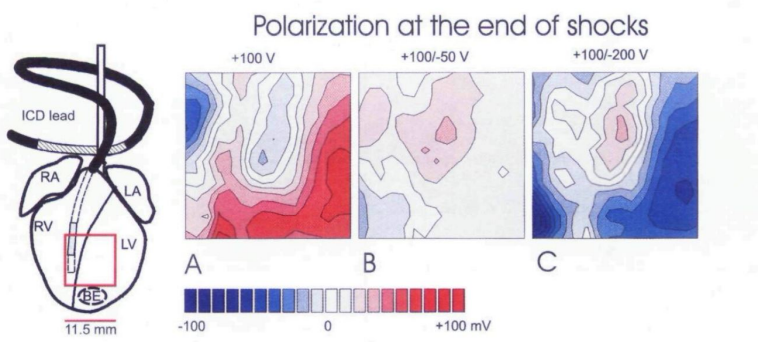

Figura 1.10: Electrical stimulation: spatial pattern of polarization. *Spatial pattern of polarization of the shock produced by (A) a monophasic (+ 100 V. 7^{th} ms of 8-ms shock), (B) optimal biphasic (+ 100 / — 50 V. 15^{th} ms of 16-ms shock), and (C) nonoptimal biphasic (+ 100 / — 200 V. 15^{th} ms of 16-ms shock) shocks. The area of recordings is indicated by the red box. Values of polarization are shown relative to the preshock transmembrane voltage, with red assigned to positive polarization, blue to negative polarization, and white to areas of no polarization. ICD = implantable cardioverter-defibrillator: LA = leff atrium: EV = leff ventricle: RA = right atrium; RV = right ventricle. Reproduce from [73]*

unpredictability of ICD shocks and the possibility of device failure [4], [95], [96]. It is worth mentioning that, although S-ICD is associated with a lower rate of complications due to the lack of venous access, not all patients are ideal candidates and thereby these issues cannot be fully settled [97]–[99].

1.4 Optical stimulation

Electronic cardiac devices are the primary therapy for arrhythmias that cannot be treated with drugs or surgery. Although uncommon, infections, lead failures, and vascular complications do result in mortality and morbidity for some patients [100]. Battery life limitations, which require device changes and increase risk of infection [2], [3], and pain due to high-energy electricshocks [4] are just a few examples of these unsolved problems. Because of these and other shortcomings, the development of a novel tool for arrhythmias treatment is of great interest.

The use of light for optical stimulation of CMs has emerged in the last decade as a valid alternative to electrical stimulation since it allows high spatial and temporal precision of manipulation and modest energy requirements [6]. Moreover, light allows decoupling recording from stimulation and avoids physical contact between the stimulation source and the target cell, thus escaping problems related to contact impedance [101].

It seems likely that these advances have relatively little relevance in pacing devices that are already highly efficient and reliable but could be quite attractive in cardiac defibrillation. Indeed, optical stimulation of a light-sensitized heart could extinguish arrhythmia using significantly less energy than high-energy electric shocks delivered by implantable devices. This could dramatically improve battery life and reduce tissue damage. Additionally, the high spatial resolution of point light source would prevent collateral excitation of muscles surrounding the heart, thereby eliminating the major source of defibrillation-induced pain and discomfort [5], [6]. Therefore, optical defibrillators could potentially offer a pain-free therapy applicable to conditions that are not treated today due to the low tolerance of shocks. AF, for instance, is not treated with electrical defibrillators since it would need to deliver painful electroshocks many times a day [6], [7].

However, since cardiac cells do not display any specific response to light, several strategies have been proposed to elicit light-sensitivity in target cells. The basic principle is the realization of suitable light actuators, which means interfaces able to transduce light into a biological signal (bioelectrical, biochemical, or biomechanical). Optogenetic, for instance, uses a genetic modification of cells to express light-sensitive actuators (ion channels/pumps or molecular switches) on their membrane [102]–[104]. Optogenetics allows controlling in a very selective and specific way transmembrane as well as intracellular events, but it has the major obstacle of requiring the introduction of exogenous genetic material using viral vectors. In addition to the safety issues related to the choice of a suitable viral vector (diffusion, inflammation, gene incorporation in the genome), another pitfall is due to the expression of heterologous proteins from very distant species that can trigger an appropriate but undesirable, immune response in the host organism [105]. Avoiding these problems would open up a much broader field of applications. For this reason, the geneless opto-stimulation of living cells and tissues is a growing field of research at the border between photonics, materials science, and biology. Metals, inorganic and organic semiconductors, or just molecular chromophores have been used as phototransducers in different shapes, from planar interfaces to micro-structured surfaces and nano-particles or micro-particles. These light-based stimulation methods initially found neuroscience applications, but, more recently,

have proved relevant to other excitable tissues. In cardiology, optical stimulation is giving great opportunities both in fundamental science and in translational research.

Concerning *in vivo* light delivery, LEDs in flexible biocompatible membranes [106], [107] or μLED arrays [107], [108] have been recently proposed as cutting edge technologies, but further improvements will be necessary for cardiac optical stimulation to become relevant for clinical applications.

1.4.1 Optogenetic approaches

Since its development, optogenetics has been used in the field of neuroscience to study neurophysiopathology by light-induced modulation of electrical activity in neurons. Bruegmann and coworkers have shown for the first time that optogenetics can be employed for light-based pacing of CMs *in vitro* and of the atria and ventricles of transgenic mice *in vivo* [8]. Similarly, Arrenberg and colleagues demonstrated in embryonic zebrafish hearts light-induced hyperpolarization with a light-driven chloride-pump to block excitation as well as pacing based on optogenetic protein Channelrhodopsin2 (ChR2) [109]. These publications set the stage to subsequent publications focusing mainly on optogenetic pacing [110]–[113]. The potential application of this technique has been reviewed extensively in [5]–[7], [114].

In 2016, Bruegmann et al. published the first proof of concept for optogenetic defibrillation of VT in perfused mouse hearts [9]. Computational models of patient-specific hearts were also used to dissect mechanisms and assess the feasibility of translating optogenetic defibrillation to clinical settings. The results revealed that light stimulation could potentially terminate VT in the human heart, but only using a deeper-penetrating red light able to overcome the significant light attenuation in the thick human ventricular walls. In later studies, optogenetic defibrillation has been proposed for both AF [115]–[117] and VF [9], [118]–[120].

Three main strategies have been explored since then: (1) optogenetic defibrillation using conduction block by continuous depolarization; (2) defibrillation using a filling of the excitable gap by optogenetic pacing and (3) defibrillation by optogenetic hyperpolarization (Fig. 1.11). An extensive review was recently published by Sasse et al. [7].

Before optogenetic therapies can be suggested to patients, the proof-of-concept studies mentioned above have to be verified in preclinical large animal models with human-like anatomy and arrhythmia. In addition to it, long-lasting virus-based gene transfer without immunological reactions against viruses or the non-human optogenetic proteins must be established. Furthermore, because of the thick left ventricular wall of humans, it is questionable if epicardial gene painting results in sufficient transmural gene expression for optogenetic termination of arrhythmias or if the systemic or intracoronary infusion of adenoviral vectors is better suited in this case. Finally, sufficient transmural illumination must be achieved, e.g., by injectable cellular scale optoelectronics [121], [122],

1.4.2 Geneless approaches

Although effective and non-invasive, optogenetic cardiac modulation could be difficult to implement in patients due to the need for gene transfection and the

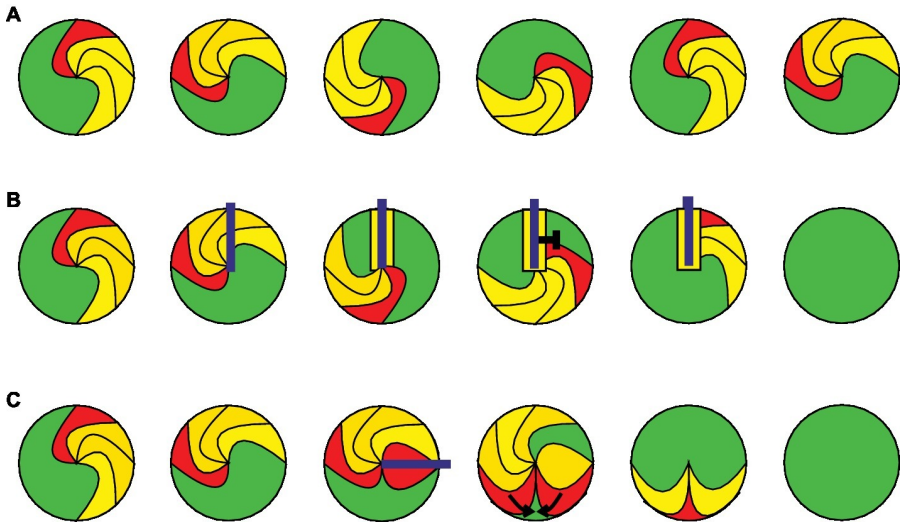

Figura 1.11: Optogenetic termination of cardiac arrhythmia. *The leading edge of the arrhythmic wavefront is shown in red, the depolarized and refractory tissue in yellow, and the excitable gap in green. The illumination is displayed in blue. (A) A stable rotor of a cardiac arrhythmia is shown at different time points during one cycle around a phase singularity. (B) Example of optogenetic arrhythmia termination by conduction block. Sustained illumination starts within a depolarized area and keeps the surrounding area depolarized until the next arrhythmic wavefront entering this region is blocked by refractory tissue. (C) Optogenetic arrhythmia termination by filling of the excitable gap. Brief illumination of the excitable gap generates a second excitation wavefront, which travels toward the arrhythmic wavefront until both are extinguished by their collision. Reproduce from [7]*

possibility of an immune response. Other optical modulation techniques rely on light stimuli alone or the use of a material that can convert the optical input into heat or electricity to alter the membrane voltage of the target cells.

Infrared radiation. Firstly, the use of infrared radiation (IR) has been investigated. IR control is defined as thermally-induced infrared light activation or inhibition of excitable tissues. In cardiology, the technique showed promising results in 2010 [123] and 2013 [124], when Jenkins and coworkers paced an intact embryonic heart and an adult rabbit heart, respectively.
The mechanism of action was investigated by Shapiro et al., in 2011 [125]. According to this work, infrared light is absorbed by water and produces a rapid local increase in temperature, which transiently alters the electrical capacitance of the plasma membrane, finally generating depolarizing currents. It is precisely this potentially-damaging overheating that raises concern in the scientific community about the possible use of the technology in the clinic, even though that several studies have confirmed its safety [126].

Light-sensitive interfaces. An alternative approach exploits the photoinduced physical phenomena of certain light actuators to induce light-evoked stimulation in living matter. Metals, inorganic and organic semiconductors have been used as phototransducers in different shapes, from planar interfaces to micro-structured surfaces and nano-particles or micro-particles [38]. In that regard, Gentemann et al. described the use of gold nanoparticles irradiated with a $532nm$ laser to induce

heating of the cardiac cells, which leads to calcium oscillations and cell contraction when placed in a calcium-containing buffer [127]. In a different approach, Savchenko et al. used graphene's ability to convert light into electricity to pace cardiac cells and tissues *in vivo* [128]. Further development in the field was presented in 2019 by Parameswaran and coworkers. The authors developed a flexible polymer–silicon nanowire mesh for the optical stimulation of cultured primary CMs as well as adult hearts *ex vivo* [11]. Extended planar organic interfaces were also used by our research group to achieve light-dependent modulation of the electrical state of CMs *in vitro* through a photothermal effect [129]–[131]. Overall, these findings represent the proof-of-concept that the polymer-mediated cell photostimulation phenomenon opens up interesting possibilities in cardiac therapy and for the implementation of *in vitro* studies.

Photoactivatable molecules. An even less invasive strategy employs photosensitizing dye molecules for light-based cell stimulation. This technique could be considered as part of the growing area of photopharmacology, where the photochemistry and pharmacology of biologically active molecules are linked. In this field, photopharmacological agents operate via the incorporation of a molecular photoswitch or a photoactive protecting group into their structure [132].

Focusing on optical stimulation of cells, the two most common approaches are the use of molecular photoswitches targeted to membrane bilayers [133]–[137] or photo-triggers, where a photosensitive element is linked to an ion channel to modulate its dynamics in a light-dependent fashion [138]–[141]. The latter uses the so-called *caging approach*, where a key functional group is protected with a light-sensitive protecting group. This approach renders the biomolecule inactive until the caging group is removed with light. Molecular photoswitches, instead, are a class of chemical compounds that can be switched between at least two distinct thermodynamically stable states by the application of an external stimulus. A desirable feature of such photoswitches is photochromism, whereby the switches exist reversibly in two stable states with different electronic properties (e. g., HOMO-LUMO gaps, dipole moments, and π-conjugation). Several organic compounds have been deployed to develop a functional photoswitch. Among them, the most widely used class has been represented by the azobenzene and its derivatives, due to its extremely high photostability and ease of functionalization [142].

The use of azo-compounds in cardiac electrophysiology is an emerging field of research, but few works have been published so far. In 2011, the research group of Agladze demonstrated that monolayers of neonatal CMs treated with azobenzene trimethylammonium bromide (AzoTAB) can be rendered unexcitable when illuminated by $440nm$ light (*trans* isomer) and can fully recover their excitability when the illumination wavelength is switched to 350 nm (*cis* isomer). Simultaneous irradiation at two wavelengths with properly chosen intensities allowed for dynamic control of the *cis* isomer/*trans*-isomer ratio and the level of excitability from normal to fully unexcitable [20]. In the following study, the authors investigated the effects of *trans* and *cis* isomers of azoTAB on voltage-dependent sodium (I_{Na}), calcium (I_{Ca}), and potassium (I_K) currents in isolated neonatal rat CMs using the whole-cell patch-clamp technique. The experiments showed that azoTAB modulated

ion currents, causing suppression of sodium (Na^+) and calcium (Ca^{2+}) currents and potentiation of net potassium (K^+) currents [21]. In other terms, azoTAB reversibly enables the tuning of cardiomyocyte excitability to the desired degree. Nevertheless, azoTAB is noticeably toxic to the cells, thus, it has no pharmacological prospects and cannot be used in tissue culture experiments for extended periods, i.e., several hours or more. For these reasons, new work has been recently devoted to evaluating the effectiveness of stilbene derivative c-TAB in controlling cardiac cells excitability. Remarkably, even c-TAB was shown to successfully inhibit excitation in cardiac cells, as well as single cells and cells in a culture, in both, *trans*- and *cis*- forms. However, the excitation inhibition of cardiac cells under c-TAB can be restored only by washing out the c-TAB and not by light illumination. Moreover, irradiation of cardiac cells with near-UV, when the *trans*- form of c-TAB is applied, changes reversible inhibition to a permanent one that cannot be overturned by a washout [22]. A slightly different approach has been reported by Riefolo et al., in 2019. In their work, the authors were able to modulate the cardiac function with a light-dependent activation of the muscarinic acetylcholine receptors, which are known to decrease heart rate and prolong the atrioventricular conduction time when stimulated. Specifically, a molecule, named PAI, was designed by the introduction of a photoswitch into the molecular structure of an M2 muscarinic acetylcholine receptors agonist. PAI activates M2 receptors in its *trans* configuration and can be reversibly photoswitched with different wavelengths including near-infrared light under two-photon excitation [23].

Overall, these results provide a first proof-of-concept that molecular photoswitches and photo-triggers can offer an effective solution for a non-invasive cardiac cells optical stimulation.

1.5 Azobenzene-based photoswitches

1.5.1 Azobenzene chromophore

The discovery of azo-compounds dates back to the mid-1800s and for many years azo-compounds have been an important class of synthetic coloring agents in the dye industry [143]. In 1937, G. S. Hartley observed a lack of reproducibility in absorbance measurements when an azobenzene solution was exposed to light. This experiment together with further analysis proved almost conclusively that the phenomenon was consistent with a reversible formation of azobenzene *cis*-isomer [144]. Since then, a large body of work has made azobenzene among the best characterized molecular photoswitch. Despite the abundance of application-driven research, azobenzene photochemistry and the isomerization mechanism remain topics of investigation. A recent review can be found at [145].

Photoisomerization

The *trans* conformation of azobenzene is more stable than the *cis* isomer so that, in the dark at equilibrium, *trans* is the dominant isomer. *Trans*-to-*cis* isomerization occurs following irradiation with UV-visible light, mechanical stress [147], or electrostatic stimulation [148]. *Cis*-to-*trans* isomerization, instead, can occur both spontaneously in the dark owing to the thermodynamic stability of the *trans* isomer, or by visible-light irradiation (Fig. 1.12).

Trans azobenzene undergoes *trans*-to-*cis* isomerization following both $S_1 \leftarrow S_0$ and $S_2 \leftarrow S_0$ excitation. On the contrary, the *cis* isoform can be converted to *trans* azobenzene by exciting into the S_1 or S_2 state. Four mechanisms (rotation, inversion, concerted inversion, inversion-assisted rotation) have been proposed as possible pathways for its photoisomerization (Fig. 1.13).

According to X-ray and computational data, the *trans* conformation is near planar, with C_{2h} symmetry and a dipole moment close to zero. The *cis*-isomer, instead, adopts a non-planar conformation with C_2 symmetry. The *cis* isomer adopts a bent conformation with its phenyl rings twisted $\sim 55°$ out of the plane from the azo group and has a dipole moment of 3 *Debye*. In addition to the

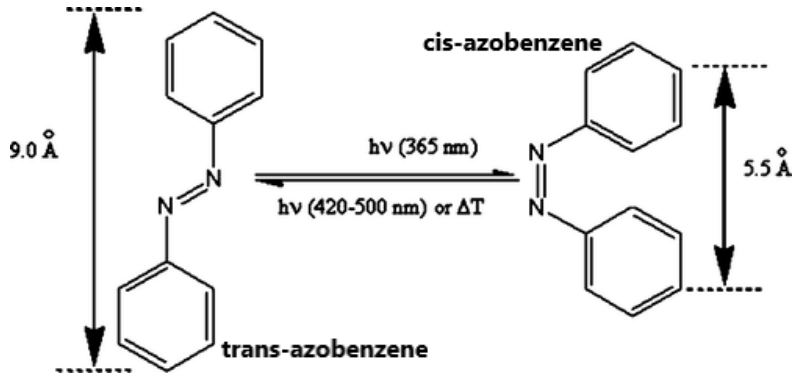

Figura 1.12: Schematics of the isomerisation process in azobenzene. *Reversible isomerization of azobenzene molecule between trans (planar, t-AB) and cis (twisted, c-AB) geometries in response to external stimuli such as light and heat. Reproduced from [146]*

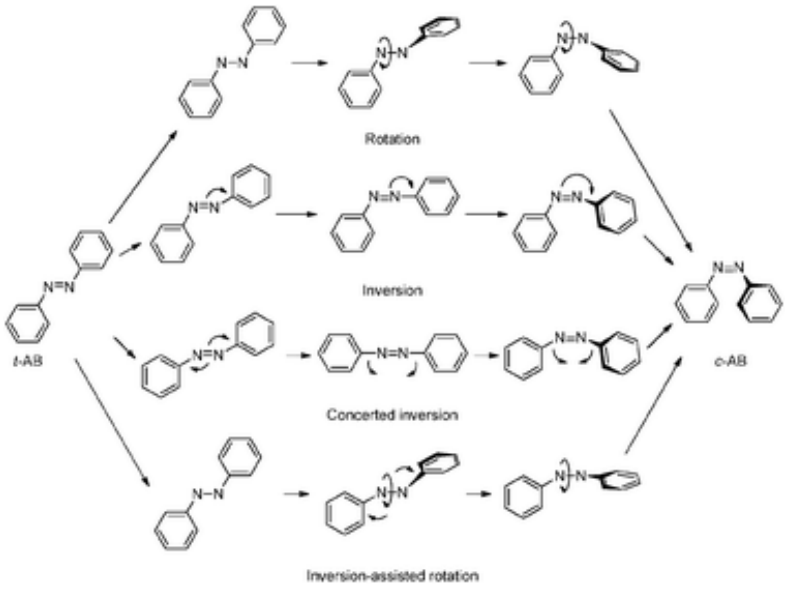

Figura 1.13: Isomerization mechanisms of azobenzene. *Proposed mechanisms for the trans-to-cis isomerization of azobenzene. Reproduced from [145]*

shape and dipole moment changes, the end-to-end distance of each isomer is also substantially different. Remarkably, it is this length difference that has mainly been exploited in azobenzene-based photoswitches [149], [150].

Spectral features

The absorption spectrum of the *trans* azobenzene shows two well-separated bands in the UV visible region. The weak band in the visible region (near 450 nm) corresponds to the symmetry forbidden $n \rightarrow \pi^*$ transition, while the much stronger UV band (near 320 nm) arises from the symmetry allowed $\pi \rightarrow \pi^*$ transition. The $n \rightarrow \pi^*$ transition of the *cis*-isomer absorbs much stronger than the *trans* isomer, causing a much prominent band in the visible region of the absorption spectrum (also near 450 nm). On the contrary, the $\pi \rightarrow \pi^*$ of the *cis*-isomer is weaker than the *trans* azobenzene. The $n \rightarrow \pi^*$ and $\pi \rightarrow \pi^*$ transitions excite to $S_1(n\pi^*)$ and $S_2(\pi\pi^*)$ states, respectively (Fig. 1.14) [145].

Azobenzene-derivatives

As previously mentioned, azobenzene compounds photoisomerizes from *trans* to *cis* with UV light, however, this can be an issue for photocontrol *in vivo* where cells and tissues can be harmed by UV exposure. Thereby, the photochemical properties of azobenzene must be modified for its practical use in biology and medicine. To this end, ring substituents have shown to be promising for the modulation of the absorption and emission spectra, as well as the photochemical properties of azobenzene. As a pointed example, substituents on the phenyl rings can make the *cis*-isomer more thermodynamically stable than the *trans*-isomer or modulate the rate of thermal *cis*-to-*trans* relaxation. The latter being dramatically affected by solvent and temperature.

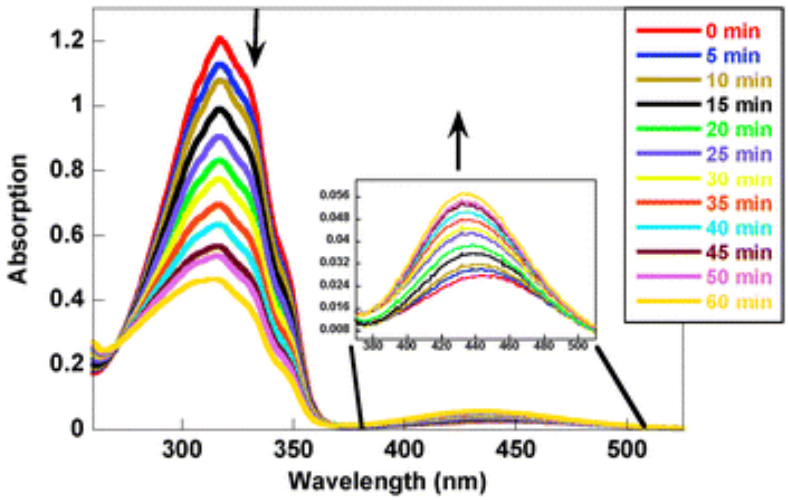

Figura 1.14: Spectral features of azobenzene. *Changes in the absorption spectrum of azobenzene upon irradiation with 316 nm light. The $S_1 \rightarrow S_0$ transition appears as a band at 440 nm (inset) and the $S_2 \rightarrow S_0$ transition absorbs at $\sim$ 320 nm. Reproduced from [145]*

Besides absorption spectrum tuning, attention must be given to the design of light-sensitive actuators *in vivo* to create molecules that are chemically stable in the reducing intracellular environment [151]. Finally, to achieve photocontrol of biological function *in vivo*, the photochromic must be modified to specifically target a biomolecule or/and to be membrane permeable.

1.5.2 Applications in biology

Azobenzene moiety has been widely employed as a versatile photoresponsive element for conferring reversible photosensitivity to bio-inspired targets, such as peptides, nucleic acids [152], ion channels, and artificial membranes. The principal applications are reported below.

Azobenzene-modified peptides

Peptides, for instance, have been considered a promising target for photo-control due to their multiple functional roles in biology (e.g. hormones and ligands for receptors). Both backbone and side-chain incorporation of azobenzene photoswitches has been explored. Backbone incorporation of azobenzene, for instance, was used to allow or prevent the formation of $\beta-$turn like structures in acyclic peptides [153]. Azobenzene derivatives via peptide side-chains, instead, were used by Woolley and colleagues to target $\alpha-$helical peptides [154]. The basic concept of these approaches is that end-to-end distance change between *cis* and *trans* isomers and that determine the disruption or the stabilization of peptide structure (e.g. helical content).

Azobenzene-modified proteins

Parallel to light-sensitive peptides, azobenzene-modified proteins have attracted a growing interest due to the variety of roles of proteins as biological catalysts and information traffickers in cell signaling. Two general approaches have been described.

The first widely used strategy is to use the azobenzene photoswitch directly to trigger an alteration in the protein structure, and consequently in its function. As with the photo-control of the peptide structure described above, the strategy was to couple the end-to-end distance change that occurs upon azobenzene isomerization to a protein structural/functional change. Woolley and colleagues, for instance, started from the X-ray crystal structure of a folded protein, to identify potential pairs of surface-exposed residues for cross-linking based on end-to-end distance matching with *cis* or *trans* azobenzene cross-linkers [155]. The cross-linking sites identified were then mutated to *cis*-isomer and cross-linked. Thus, *trans* form destabilizing the protein while the *cis* form stabilized the folded state [156]. The second approach for photo-controlling protein function is the development of photoswitchable tethered ligands that control protein function. This area has been dominated by Isacoff, Kramer, Trauner, and colleagues who used photoswitched tethered ligands as a general tool to photo-control ion channels (e.g. light-gated K^+ ion channel). Substantially, the photoswitchable ligand reacted with a residue at a specific distance from the binding pocket, and the different extension between *trans* and *cis*-isomer allows the blocker to reach or not the pore, respectively preventing or enabling the ion flow. This light-gated ion channel allowed for reversible photo-inhibition (hyperpolarization) of APs in hippocampal neurons [138], [157]–[161]. The major difference of this approach w.r.t. optogenetics (see Paragraph 1.4.2), is that this strategy allows endogenous ion channels to be targeted without the expression of modified genes which may not be very practical under certain conditions.

Azobenzene-loaded membranes

Contemporary with the development of these strategies, which target both peptides or biomolecules to control cell biology, azobenzene-loaded membranes have been also explored. This field of research has evolved considerably over the last decades, demonstrating that a conformational change in the structure of a photochromic molecule incorporated into a membrane can effectively induce a reversible change in its properties.

Pioneering work in this research field was presented in 1991 by Fujiwara and Yonezawa. The study showed a photoelectric response in a *black lipid membrane* of egg lecithin doped with an amphiphilic azobenzene derivative [135]. At that time, the authors hypothesized that the transient current (Fig. 1.15) pulses under alternate irradiation with UV and visible light could be related to a change in the membrane capacitance caused by *cis-trans* photoisomerization of the azobenzene compound. Additionally, Tanaka and Yonezawa observed that the transient photocurrent overlap with a steady d.c. current, possibly related to the formation of photochemically regulated quasi-channel, specific for K^+ ion [136]. The interest for this researches soared over the following years and several studies began to investigate this elicited photocurrent in photoswitch-loaded lipid membranes.

Non-peptidic light-gated channels, for instance, were designed by the means of azo-group-containing substituents. Salzer and colleagues developed artificial ion channels, properly modified with azo-compounds to provide light-sensitivity [162]. Furthermore, at the beginning of the 21^{th} century, photosensitive bolaamphiphiles were also tested in giant unilamellar vesicles, i.e. cell-sized vesicles made of lipid

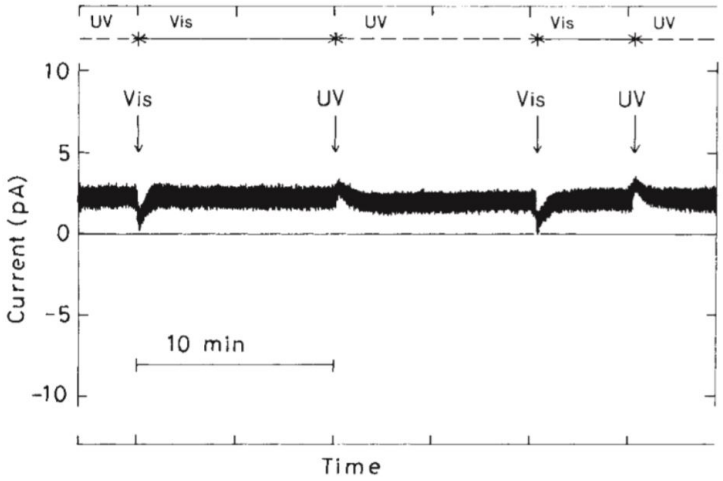

Figura 1.15: Photoelectric response of azobenzene-loaded membranes. *Time dependence of change in direct current on continuous illumination of the modified Black Lipid Membrane (BLM) with ultraviolet ($\lambda = 365nm$) and visible ($\lambda = 450nm$) light. $V_{app} = 10mV$. Ultraviolet ligh (- - -) ; visible light (—). Reproduced from [135].*

which represent a better model for biological and chemical applications w.r.t. a planar membrane or small vesicles. Light-induced shape deformations [163], membrane phase separation [164], and fusion event [165] were investigated in vesicles loaded with azo compounds.

Of interest, light-responsive amphiphilic molecules have also been used to achieve non-specific permeabilization without causing membrane disruption [166]. Azobenzene-modified molecules were explored, for instance, for triggering controlled membrane permeabilization upon visible light irradiation in pH and ionic strength conditions that are biologically relevant.

1.6 Ziapin2

In the context of the reviewed literature, our research group has recently developed and tested *in vitro* and *in vivo* an intramembrane visible light actuator that allows photocontrol of the membrane potential via an optomechanical effect. An amphiphilic azobenzene-derivative, called Ziapin2, has been employed to modulate reversibly the biological signals. Although avoiding covalent bonding with ionic channels, the designed photochromic molecules tend to partition into the cell membrane, where their conformational dynamics is preserved. The results confirm that Ziapin2 photochromic can be used as new membrane-specific optical triggers [12], [18].

1.6.1 Molecular characterization

The designed photoswitch combines a hydrophobic backbone containing the photoactive 4−4 diaminoazobenzene substituted, on one side, with an azepane and, on the opposite side, with alkyl chains that are $\omega-$substituted with cationic groups (pyridinium salts). The combination of the alkyl-substituted azobenzenes with a capping cation enables the formation of amphiphilic species, which are, at least in theory, capable to dwell inside the cell membrane. According to theoretical studies, the *trans*-isomer shows a quasi-planar structure with a dihedral angle between the phenyl rings of 14°, while the *cis* form shows a distorted structure, with a dihedral angle of 46° (Fig. 1.16).

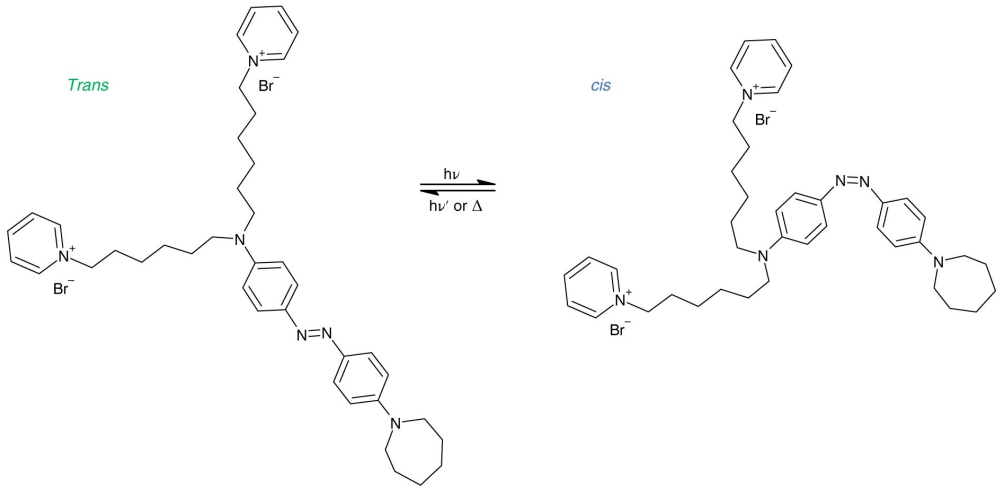

Figura 1.16: Schematics of the isomerisation process in Ziapin2. *Azobenzene molecules undergo reversible trans-to-cis isomerization upon illumination with visible radiation, with the reverse cis-to-trans isomerization driven by either light or slower vibrational cooling. Reproduced by [12]*

Computational studies suggest also that, in vacuum, the *trans*-species present a vertical (i.e. *Franck-Condon* region) dipole active excited state at $430nm$ featuring a $n \rightarrow \pi^*$ character with molecular orbitals delocalized over the azobenzene moiety. On the contrary, the *cis*-species show two vertical dipole active excited states computed at $537nm$ and $367nm$, associated with the $n \rightarrow \pi^*$ and $\pi \rightarrow \pi^*$ transitions,

respectively. According to the theoretical calculations, the absorption spectrum of the *trans*-species in a conductor polarizable continuum environment, such as water, present two dipole active excited states for the *trans*-species, red-shifted w.r.t. the one in vacuum.

1.6.2 UV-Vis spectroscopy

The experimental UV-Vis absorption spectra of the molecules in dimethyl sulfoxide (DMSO), water and sodium dodecyl sulphate (SDS) were analyzed. The latter being indicative of the photochromic behavior of Ziapin2 in the lipid bilayer environment of living-cells [167], since SDS has a strong tendency to spontaneously form mixed vesicles upon the combination with single-tailed surfactants with opposed charged head groups. In DMSO, the absorption spectrum of Ziapin2 presents a vibronic structure with a major peak at 470 nm. A large bathochromic shift (i.e., peak moves towards higher wavelengths) was observed in the UV-Vis absorption spectra, when passing from DMSO to water, accompanied by the vanishing of the vibronic structure. Remarkably, when Ziapin2 molecules were loaded in micelles of SDS, the spectrum showed a reduced spectral shift w.r.t. water and a recovery of the vibronic structure observed in DMSO (Fig. 1.17a).

Also photoluminesce (PL) spectra reveal dramatic changes between the different local environments in both spectral position and relative emission quantum yield (i.e., number of times a specific event occurs per photon absorbed by the system). Upon addition of water to the DMSO solution a new red-shifted and structureless PL band centered at 600 nm develop, affording progressively higher relative intensity than in DMSO. These results, together with scanning electron microscopy images of Ziapin2 molecules in water, suggested the formation of excimer states within micellar aggregates. Remarkably, when SDS is added to the aqueous buffer Ziapin2 emission peaks at 570nm and features a three-fold decrease in the relative emission intensity if compared to the water solution, suggesting that Ziapin2 could reacquire its non-radiative isomerization (Fig. 1.17b).

1.6.3 Photoisomerization dynamics

Two different techniques can be used to prove the isomerization reaction: (1) Steady-state absorption measurements; (2) Time-dependent quenching of *trans*-isomer PL upon illumination and (3) Ultrafast transient absorption.

Ensemble photoisomerization dynamics

Steady-state absorption measurements. In DMSO, under illumination with a blue LED (470nm), Ziapin2 undergoes a *trans*→*cis* isomerization reaction that leads to a *cis*-rich photostationary state with an extracted time constant $\tau = 60\ ms$ and a thermal *cis*→*trans* back relaxation characterized by $\tau = 3s$. The presence of the *cis* species is confirmed by the rising of the two absorption bands at 370 nm and 550 nm in the *cis* form absorption spectrum. The weak absorption band centered at 500 nm accounts for the residual *trans* population (30 %). In water, instead, Ziapin2 photoisomerization results suppressed likely due to the formation of micellar

aggregates that hinder molecular switching. Finally, in SDS the fast photoswitching ability is fully recovered with an extracted time constant equals to DMSO, although the photostationary state contains only 10 % of the *cis*-isomer. Such decreased isomerization yield in SDS compared to DMSO can be likely related to a fraction of molecules remaining in water and forming non-isomerizing aggregates or to a more constrained conformational freedom experienced by Ziapin2 inside the micellar environment than when solubilized in DMSO.

Time-dependent quenching of photoluminescence. The measure of *trans*-isomer PL quenching upon illumination confirms the results obtained from steady-state absorption measurements. The basic idea of this approach is that isomerization competes with radiative recombination and the *cis*-isomer is poorly or non-emitting, thereby a decrease in PL of *trans*-isomer upon illumination is indicative of an ongoing photoisomerization process. In other terms, the PL signal decreases with the increase in the isomerized moiety.
Ziapin2 *trans*-isomer was illuminated blue light (470 nm) to excites its emission and triggers the isomerization. The expected decrease of PL was visible in the excitation spectra acquired from both DMSO and SDS, while no appreciable collective photoconversion was observed in water.

Molecular photoisomerization dynamics

In contrast with the ensemble isomerization process, molecular isomerization event occur in the ps time scale and, thereby, requires ultrafast techniques to be detected, such as transient absorption (TA). In a TA experiment, the pump pulse brings population to the excited state, while a broadband probe pulse interrogates this state and tracks its temporal evolution. Transient absorption spectra at early delay-times for DMSO, water, and SDS show three main features: (1) a positive peak centered at $470-500nm$ that can be attributed to ground-state bleaching

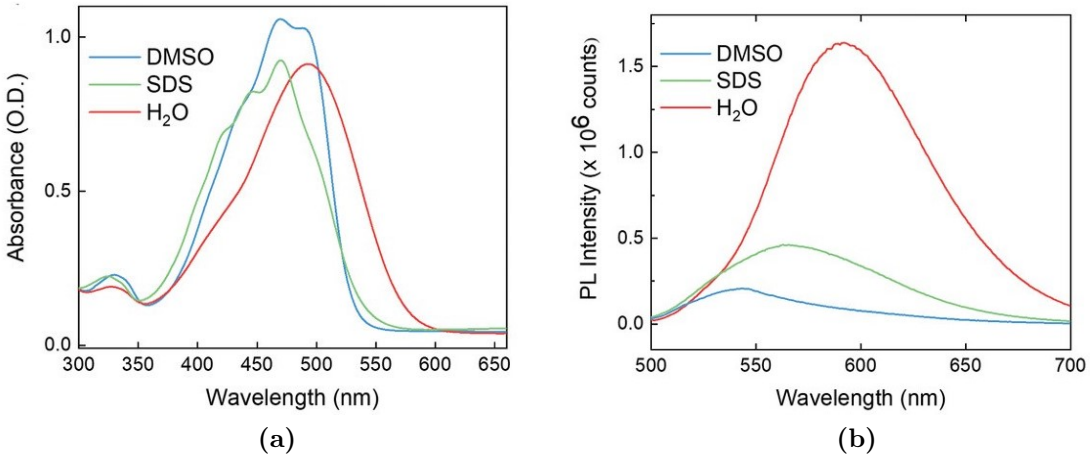

Figura 1.17: Spectral features of Ziapin2. *(a) UV-VIS and (b) Photoluminescence (PL) spectra of Ziapin2 in DMSO, SDS, and water. PL spectra were normalized to both lamp intensity and ground-state absorption, to obtain a relative PL quantum yield among the three solutions. Reproduced by [18]*

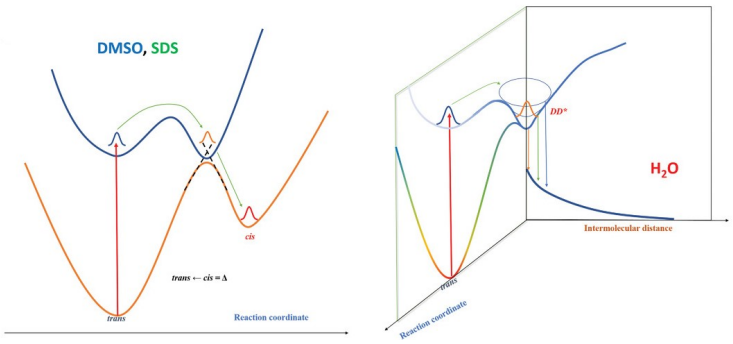

Figura 1.18: Photodynamics of Ziapin2. *Sketch of the photodynamics in DMSO and SDS (left) and water (right) as suggested by the transient absorbption data and global analysis. (left) Photoisomerization; (right) Photoinduced formation of excimers within the micellar aggregates. Reproduced by [18]*

($S_0 \rightarrow S^*$, PB); (2) another positive peak at $570 - 610nm$ that can be linked to stimulated emission ($S^* \rightarrow S_0$, SE) and (3) a negative feature at around $700nm$ due to photoinduced absorption from excited states ($S^* \rightarrow S_n$, PA).

Two components can be identified, with different kinetics and decay associated spectra. In DMSO and SDS, the photodynamics is well consistent with the isomerization reaction: the first component represents the *trans* isomer that decays into a second component ($\tau = 6\ ps$ and $12\ ps$ for DMSO and SDS, respectively), which in turn indicates the long-living *cis* isomer metastable state (thermal *cis* $\rightarrow$ *trans* relaxation lifetimes of 3 ns and 6 ns for DMSO and SDS, respectively). Conversely, in water, the first component evolves rapidly ($\tau = 2\ ps$) into a second red-shifted component (about 30 nm) with a relatively short lifetime ($\tau = 20\ ps$). Interestingly, in this case, the first component can be related to the *trans* isomer that decays in the excimeric red-shifted state (second component) via vibrational relaxation. The second component is assigned to the excimer state (Fig. 1.18) [18].

1.6.4 Ziapin2 *in vitro* and *in vivo*

To date, Ziapin2 biological effect has been assessed *in vitro*, in both HEK-293 cells [18] and hippocampal neurons [12]. Additionally, the effectiveness of the molecule in eliciting neuronal activity was also verified *in vivo*, through the injection of Ziapin2 in the somatosensory cortex of mice and the modulation of its cortical activity with light. Remarkably, the monitoring of cortical activity was possible up to 7 days after injection, without any inflammatory reaction to the surgery.

Localization. 3D z-stack and time-lapse confocal imaging on live HEK-293 cells and primary hippocampal neurons loaded with 25 μM Ziapin2 confirmed the affinity of the molecule for lipid bilayers and a fluorescence time-to-plateau of about 7 min. In primary hippocampal neurons, colocalization studies showed that Ziapin2 is prevalently ($\sim 60\%$) present at the level of lipid rafts.

w.r.t. long-term applicability, confocal imaging indicated that $\sim 30\%$ of the initial Ziapin2 labeling was preserved on the plasma membrane 7 days after loa-

ding. Remarkably, this reduced membrane Ziapin2 concentration caused a partial reduction of the light-evoked effect.

Photoisomerization. A micro-PL set-up was used to verify that photoisomerization was partially retained in Ziapin2-loaded HEK-293 cells, thanks to the fraction of Ziapin2 molecules that dwell in the plasma membrane and remain protected by water and therefore do not aggregate (Note that this was in accordance with the results obtained from SDS). Although the estimated average relaxation time is tremendously increased, probably due to a more disordered environment, PL decay confirmed an initial fast decay comparable with the relaxation times of Ziapin2 in DMSO and SDS.

Electrophysiology. According to patch-clamp techniques, photostimulation induce a significant light-induced change in the resting plasma membrane potential (V_m). Whole-cell recordings, carried out in current-clamp mode ($I = 0$) in response to 20 and 200 ms visible light pulses (470 nm, 50 mW/mm^2), demonstrate that photoisomerization determines an initial hyperpolarization of the V_m that appeared immediately at the light onset, and returned slowly to the physiological resting values after a small rebound depolarization that occurred at the light offset.

Another important consideration focuses on the effect of Ziapin2 molecules on AP modulation. Firstly, the addition of Ziapin2 in dark caused a partial suppression of the spontaneous activity of hippocampal neurons (due to an increase in the rheobase) and a slowdown of the rising and repolarizing slopes. Second, light stimulus elicited a significant increase in AP frequency and restored the original rising slopes and peak amplitudes.

According to computational studies, these effects could be caused by a light-induced change in membrane thickness and, thereby, in membrane capacitance (Fig. 1.19). Molecular dynamics simulations showed that Ziapin2 molecules in *trans* conformations could anchor to the opposite leaflets of the membrane or lipid rafts and form dimers via backbone interaction. This way the lipid heads could be pulled towards the center of the bilayer, decreasing the membrane thickness and leading to an increase in membrane capacitance. Conversely, after photoisomerization to *cis* conformation, the hydrophobic tails of opposed molecules would be too far from each other to dimerize and the membrane thickness could return to its unperturbed state, with a significant drop in the membrane capacitance.
To verify this hypothesis, our group measured the capacitance of Ziapin-loaded HEK-293 cells and primary hippocampal neurons. In both conditions, a significant increase in capacitance was observed (i.e., from 32.4 $\pm$ 1.7 pF to 53.3 $\pm$ 6.0 pF in hippocampal neurons). As expected, upon illumination (i.e., after photoisomerization to *cis* conformation), the increased capacitance returned towards basal levels. Voltage-clamp experiments in primary hippocampal neurons confirmed the occurrence of light-induced transient capacitive current. These results were associated with the patch-clamp measurements. Indeed, a sudden decrease in membrane capacitance upon illumination determined an outward current responsible for the membrane hyperpolarization peaking after light onset and followed by a delayed rebound depolarization and AP firing.

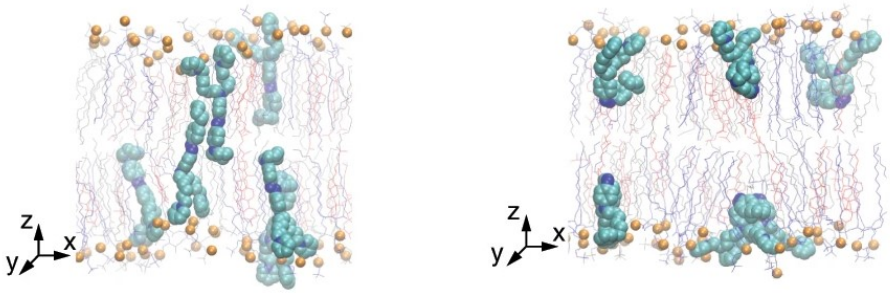

Figura 1.19: Ziapin2-loaded membranes. *Molecular dynamics simulations show that Ziapin2 in trans conformation (left) anchored to the opposite leaflets of the membrane can dimerize via backbone interaction. This results into a local depression of the membrane, which in turn results into a capacitance increase. On the other hand, upon illumination, when Ziapin2 photoisomerizes to cis conformation (right), the azepane-substituted aniline of opposed molecules are too far from each other and do not dimerize, leaving the membrane thickness unperturbed. Reproduced by [12]*

Capitolo 2

Experimental Procedures

2.1 Cellular model

2.1.1 iPSC-CMs

The experiments were performed using a cellular model of human adult CMs, derived from human pluripotent stem cells (PSCs). Needless to say that direct biopsy of cardiac tissue from patients causes irreversible injury and thus cannot be performed at this stage of preliminary research. To overcome this limit, over the last decades other strategies have been used to obtain a suitable model of cardiac cells for the *in vitro* screening (e.g. use of heterologous cells). Among them, the use of PSCs has shown significant advantages. There are two different types of PSCs: embryonic stem cells derived from human embryos and induced pluripotent stem cells (iPSCs) derived from adult somatic cells. Remarkably, the use of embryonic stem cells for cell screening applications is still highly limited due to the ethical issues related to human embryo manipulation. On the contrary, the capability to reprogram an adult somatic cell back to a pluripotent state, presented in 2006 by Takahashi and Yamanaka [168], enables the high-throughput screening process without going through ethical concerns.

Of note, iPSCs have been successfully differentiated into functional cardiovascular-relevant cells, including cardiomyocytes [169]. Nevertheless, compared to adult human CMs, those derived from human PSCs display a fetal-like sarcomeric organization (i.e., absence of transverse tubules and intercalated disks; shorter sarcomeres) and metabolism (i.e., fewer mitochondria; glycolysis-based energy production). Furthermore, hiPSC-CMs exhibit distinct electrophysiological characteristics (i.e., diverse repertoire of ion channel densities; longer action potentials) and reduced force of contraction, due to an abnormal *excitation-contraction coupling* and calcium handling. In that regard, in hiPSC-CMs diverse components of calcium dynamic processes are missing. The absence of transverse tubules (T-tubules), for instance, alters the organization of L-type calcium channels, which in adult CMs are responsible for the inward calcium current that triggers the calcium release from the SR by activating RyR 2. Such abnormal architecture generates slower calcium dynamics and alters the physiological *excitation-contraction coupling* (Fig. 2.1). To overcome these major limits, an extensive research field has developed new techniques for the maturation of hiPSC-CMs. A comprehensive review on recent advances in the field

of cardiomyocytes maturation and their implications for regenerative medicine can be found in [170], [171].
Differentiation of hiPSC-CMs to a mature stage supports the development of some characteristic typical of adult CMs: the differentiated cells show an elongated shape together with an organized sarcomere structure and primordial T-tubule, which lead to physiological calcium handling. However, despite the increased level of maturation reached by mature hiPSC-CMs, these cells are still mononucleated and lack to achieve a complete functional maturation [172], [173].

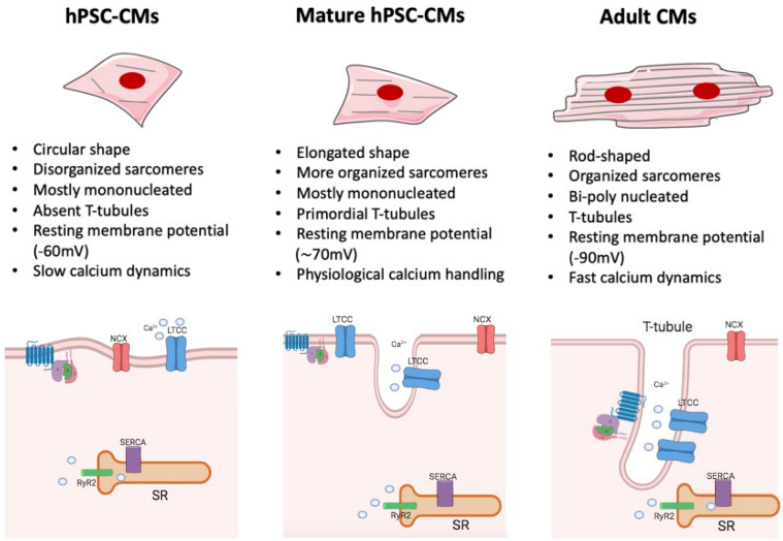

Figura 2.1: Maturation features of hiPSC-CMs. *The figure shows a schematic representation of structural and functional features of hPSC-CMs (left), mature hPSC-CMs (central), and adult human CMs (right). Some of the most relevant changes are listed. hiPSC-CMs (left) are mostly mononucleated, showing a circular shape and a disorganized sarcomeres structure compared to their adult counterpart (right). NCX, sodium–calcium exchanger; RYR2, ryanodine receptor 2; SR, sarcoplasmic/endoplasmic reticulum; LTCC, L-type calcium channel. Reproduced from [171]*

2.1.2 Differentiation protocol

hiPSCs have been generated from our collaborators at *Humanitas Research Hospital* from healthy volunteers' skin fibroblasts either through lentiviral-mediated overexpression of the four *Yamanaka vectors* or using the CytotuneiPS-2.0 Sendai Reprogramming kit (*Thermo Scientific*). The protocol used for hiPSCs generation and differentiation is described in [174], [175]. Briefly, cardiac induction and generation of hiPSC-CMs were achieved, using a chemically defined serum-free protocol, which was based on activation (*CHIR99021*) and inhibition (*IWR1*) of the *Wnt pathway* in *RPMI-B27* medium. The experiments of this thesis were conducted with CMs differentiated from two different control iPSC lines between the 18^{th} and the 35^{th} passage in culture. Importantly, employed cell lines are regularly tested for being free of major chromosomal abnormalities by karyotype analysis.

In terms of plating density, cells were seeded onto the material with 50-70% cellular confluence. hiPSC-CMs were used for the experiments 25-30 days after spontaneous contracting activity started, a differentiation stage at which they

express the repertoire of sarcomeric proteins, calcium regulators and ionic channels necessary for their correct functionality.

2.2 Ziapin2

2.2.1 Synthesis

Ziapin2 was synthesized from our collaborators at Laboratory of Synthesis of Organic Functional and Nanostructured Materials of Politecnico di Milano. The molecules were obtained by reduction of the commercially available Disperse Orange 3 followed by the substitution of the primary amines with an excess of 1,6-dibromohexane (Paragraph 1.6.1). Two different solvents were used, namely DMSO and water. In both final solutions, the concentration of the photoswitch Ziapin2 was 2 mM.

2.2.2 Incubation protocol

Ziapin2 solutions were diluted at a concentration of 5μM and 25 μM in the cell medium (Ziapin2/DMSO only 5 μM was used; while both 5 μM and 25 μM were used for Ziapin2/H_2O). This loading solution was used with hiPSC-CMs cells. The internalization process was performed incubating for 7 minutes at 37° C and 5% CO_2 with Ziapin-2 and washed two times into a glucose-free Krebs-Ringer buffer (KRH).This rinsing operation with an extracellular solution was performed to discard uninternalized azo-compounds. Of note, the incubation process and the washing operations have been performed trying to limit the light hitting the Ziapin-loaded cells.

2.3 Photostimulation

The light source for excitation was provided by a Cyan emitting LED coupled to the fluorescence port of the microscope (*Nikon Eclipse Ti* epifluorescence inverted microscope). A 20x objective was used for video acquisition with an illuminated spot area of 0.92 mm^2. For electrophysiology, instead, a 40x objective was employed with an illuminated spot area of 0.23 mm^2. The cyan LED was characterized by maximum emission wavelength at 470 nm and a photoexcitation density of 50 mW/mm^2.

2.3.1 Contractility analysis

The functionality of hiPSC-CMs was primarily evaluated with optical microscopy. In detail, contraction behavior was characterized by video recordings of beating cells during enlightenment. Videos were acquired using a camera embedded with a *Nikon Eclipse Ti* epifluorescence inverted microscope. Standard *FITC* filter set was employed to limit the collection of led light (470nm), which could alter the video processing.

The acquisition was performed with *MetaFluor Analyst* (*Molecular Devices Corporation*) software. The parameters of exposure time, number of frames and interval time were optimized to increase the frame rate. In more detail, *Stream Mode* was used with an Exposure Time equals to 60 ms and 2500 acquired frames to obtain a three-minutes video with an average frame rate of 14 fps. *Time-Lapse Mode*, instead, was used with an Exposure Time of 60 ms and an Interval Time of 100 ms to acquire 1200 frames, this to obtain three-minutes video with an average frame rate of around 6.25 fps. Once collected, the frames were uploaded as a stack in *ImageJ* and saved as .avi file.

The contraction behavior was evaluated in hiPSC-CMs loaded with Ziapin2, both with $DMSO$ or H_2O vehicles. For each solvent, two different stimulation protocols were used.

- *Single Stimulation Protocol:* 60s brightfield, 60s Light (470 nm Pulsed Mode), 60s brightfield.
- *Double Stimulation Protocol:* 60s brightfield, 60s Light (470 nm Pulsed Mode), 120s brightfield, 60s Light (470 nm Pulsed Mode), 60s brightfield.

For each ROI/cell, the contraction rate (CR) was computed at rest, within the 60s before the light stimulus is turned on (*Pre*); during the light pulses period (*Light*); and after stimulation, within the following 60s (*Post*). Likewise, for the second stimulation protocol.
The CR Modulation was computed as follow:

$$\Delta CR_{Pre,Light} = CR_{Light} - CR_{Pre} \tag{2.1}$$

$$\Delta CR_{Pre,Post} = CR_{Post} - CR_{Pre} \tag{2.2}$$

Matlab-code for contraction rate estimation

The CR of hiPSC-CMs was obtained using a custom-built tracking algorithm, implemented in *MATLAB R2020a*. The basic idea of the code is to track a set of feature points across the video frames to estimate a model of the cell motion in the video and exploit this information to compute the CR. The rationale behind this choice is that, during a contraction, the leading edges of a cell retract towards the cell body, and this movement can be recorded using *features* tracking. The algorithm counts the number of contraction within a certain running observation window (ROW) and derives the contraction frequency by dividing the number of contraction for the duration of the ROW. The algorithm is divided into three main parts:

1. User-assisted region of interest (ROI) definition
2. Tracking algorithm
3. CR estimation

User-assisted ROI definition The first step of the code is the user selection of an isolated cell or a cluster of cells, the so-called ROI. This step permits to deal even with videos that present multiple clusters of hiPSC-CMs, which contract with a different CR. In that regard, the code enables the selection of multiple ROIs at once and, then, compute the CR for each one. Once the ROI has been defined, the coordinates of the bounding box that delineate the ROI are extracted. The area is further divided into subregions by a set of concentric rectangles. In that way, even if the initial ROI, defined by the user, contains other objects that contract differently and could potentially negatively affect the tracking process, the use of multiple subregions reduce the box dimension, removing the surrounding objects and preventing the erroneous estimate of the CR.

Tracking algorithm The following steps are executed considering only one subregion at a time. The *Kanade-Lucas-Tomasi* (KLT) *algorithm* [15]–[17], [176] is used to track a set of *features* across the video frames and estimate the geometric transformation that explains the movement of the feature points between one frame and the subsequent one. Common *features* used in tracking are corners, or windows with a high spatial frequency content, or regions where some mix of second-order derivatives is sufficiently high. In this custom-built code, a set of *features* is detected using the *minimum eigenvalue algorithm* developed by Shi and Tomasi [17]. The basic idea of this algorithm is to select those image *features* that allow the reliable resolution of the motion field equations. In other words, the quality of image *features* is monitored during tracking by using a measure of feature dissimilarity that quantifies the change of appearance of a feature between the first and the current frame. When dissimilarity grows too large the feature should be abandoned (a more exhaustive explanation of the *KLT tracking algorithm* is provided in Appendix 4.3).
For each *feature* in the frame at time t, the point tracker attempts to find the corresponding point in the current frame at time t+τ (Fig. 2.2c). Once identified, the motion field (simple pure *translation*, or more complex *affine motion field* to consider even rotation and scale) is computed. This process is repeated for all points within the ROI and an average geometric transformation between the old points and the new points is estimated. At each time point, this estimated geometric transformation is applied to the bounding box that delineates the region (or subregion) of interest and its area value is measured.

Intuitively, if the bounding box is properly localized around the cell, the feature points detected with the *minimum eigenvalue algorithm* [17] would be localized on the cell body. Thus, when the cell contracts the feature points will move towards the cell body and the geometric transformation estimated will shrink the bounding box, finally resulting in a decrease of its area value.

Contraction rate estimation Once the features of each subregion have been tracked across the video frames and the area of the bounding box has been computed, the local minima of the area are detected (Fig. 4.1c). As explained above, each minimum represent a contraction. The computed number of minima is then divided by the time period (in s) to estimate a measure of CR (in Hz).

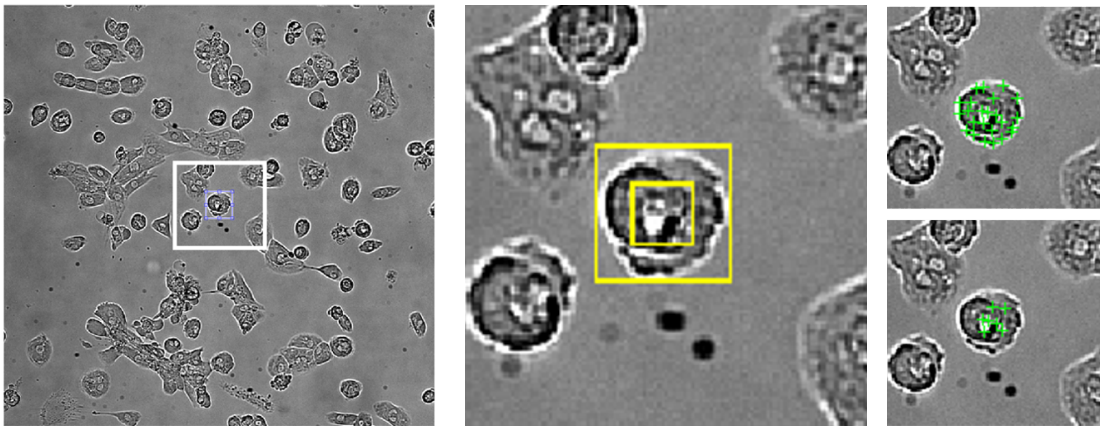

(a) (b) (c)

Figura 2.2: Features detection and tracking algorithm. *(a) The user is asked to define a region of interest (ROI) within the image: blue box. In white is indicated the magnification used for (b) and (c). (b) The user-defined ROI is subdivided into concentric subregions: yellow bounding boxes. (c) For each subregion, a set of feature points (green markers) are detected and tracked across the video frames. Features detected for the #1 subregion (above) and for the #2 subregion (below). A geometric transformation is estimated at each time point solving the equations that describe the motion field of the image between frame at time point t and frame at time point t+τ. The estimated geometric transformation is then applied to the yellow bounding box, that is reduced or magnified accordingly. The box area is computed for each frame to extract the beating signal.*

The CR was computed on different ROWs to estimate the CR before, during and after the light stimulus. To this end, a function was written to retrieve automatically from the video recordings the time points at which the led light was turned on and off (Fig. 4.1a). The code computes the mean intensity of the gray-scale image and its derivative. The maxima of its derivative represent the time points at which the mean intensity is increased and, thereby, can be associated with the instant at which the light is turned on. The other way around, the minima in the derivative represents the time points at which the mean intensity value decreases and thereby can be used to estimate the instant at which the light is turned off. When a led Pulse Mode was used, the first local maximum and the last local minimus were selected as the time points at which the light stimulus began and ended, respectively. Some cells show a more pronounced contraction than others, thus the computed displacement can change from ROI to ROI. As a consequence the trace of the bounding box area can present minima (area when cell is contracted) that are much more distant from the mean value than others. This implies that the value of prominence defined to identify the minima in the box area value cannot be defined *a priori* and user-assisted definition of prominence must be considered. In brief, the code detects the minima of the box area using a default value of prominence equals the standard deviation (SD) of the area over the video period times a certain multiplicative factor. Then, a figure window opens showing the box area values over time and the identified minima. From this plot, the user can see whether all the box area minima are correctly selected or not. If this is not the case, the user can change the value of the multiplicative factor. The figure window appears again. The process continues till the defined prominence value enables to identify all the

minima points.
Importantly, this user-assisted stage is also crucial to rule out some cells from subsequent analysis. Indeed, if the box area trace is too noisy, the user can choose to discard this ROI from the analysis.

Statistical analysis

Statistical analysis were performed in *Origin 8.0* (*OriginLab Corporation*). Since CRs were computed for the same cell over three time points, the CR should be treated as a dependent variable subjected to repeated measurements. Thus, a One-Way Anova Repeated Measures statistical test was performed to compare the obtained values pre, during and post light stimulus. Each time, the assumptions necessary to apply this statistical analysis of variance were checked.

When the Mauchly's Test returned that sphericity could not be assumed, proper corrections to the degrees of freedom were made to obtain a valid F-ratio[1]. When the analysis returned that the CRs were not rated equally, a post-hoc Tukey's test was performed to assess which pair of elements were statistically different. The Tukey's test computes all the differences between the time points (x_{diffi}), and then derives the sample mean ($\bar{x}_{diff}$), reported as Mean Diff.

2.3.2 Electrophysiology

Standard patch-clamp recordings were performed using *Axopatch 200B* amplifier (*Axon Instruments*) coupled to an inverted microscope (*Nikon Eclipse Ti*). Data were acquired with *pClamp-10* software (*Axon Instruments*) and processed with *Clampfit* (*Axon Instruments*). hiPSC-CMs were measured in whole-cell configuration with freshly pulled glass pipettes (3–6 $M\Omega$), filled with the following intracellular solution [mM]: 12 KCl, 125 $K-Gluconate$, 1 $MgCl-2$, 0.1 $CaCl_2$, 10 $EGTA$, 10 $HEPES$, 10 $ATP-Na_2$. The extracellular solution contained [mM]: 135 $NaCl$, 5.4 KCl, 5 $HEPES$, 10 $Glucose$, 1.8 $CaCl_2$, 1 $MgCl_2$. Only single hiPSC-CMs cells were selected for recordings. Membrane currents were low pass filtered at 2 kHz and digitized with a sampling rate of 10 kHz (*Digidata 1440 A*, Molecular Devices).

Membrane Potential Modulation

Current-clamp mode (I=0) was used to assess changes in the membrane potential during light stimulus. Three different stimulation protocols were used.

- *20 ms:* 200 ms Dark, 20 ms Light (470 nm *Continuous Mode*), 10 s Dark.
- *200 ms:* 200 ms Dark, 200 ms Light (470 nm *Continuous Mode*), 10 s Dark.
- *10000 ms:* 10 s Dark, 10 s Light (470 nm *Continuous Mode*), 10 s Dark.

[1] Sphericity is considered to be violated when $Prob > Chi_{squared}$ results smaller than 0.05. If sphericity is violated, several methods can be used to correct the within-subjects tests (e.g. the Greenhouse-Geisser correction can be used when ε is smaller than 0.75; the Huynh-Feldt is used for ε greater than 0.75).

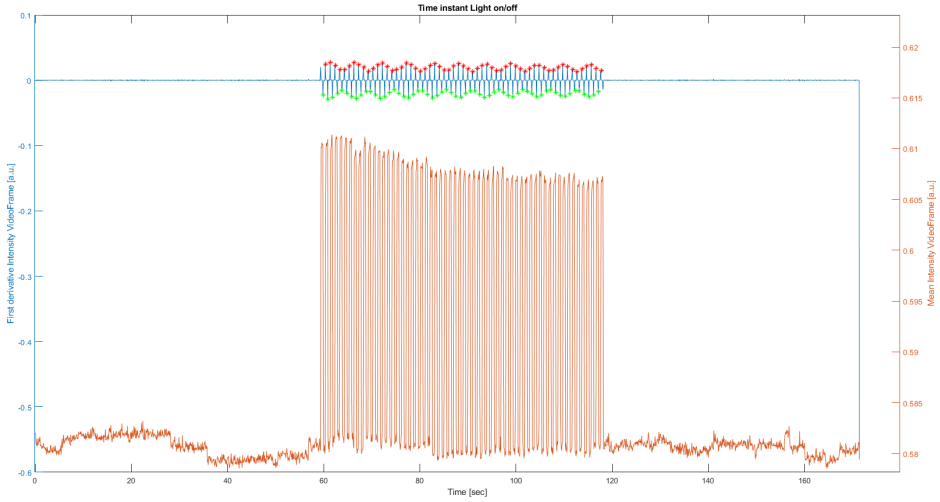

(a)

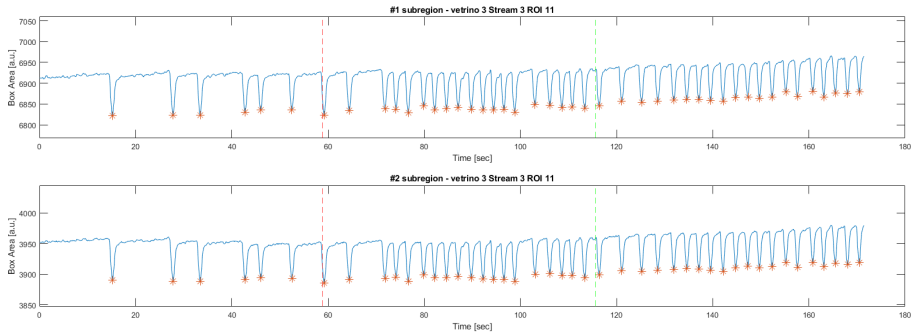

(b)

Figura 2.3: Contraction rate estimation. *(a) The mean intensity value of the gray-scale image (blue) is plotted as function of video frames. The intensity of the image increases when light is turned on and decreases when light is turned off. To identify the respective time instants the derivative of the light intensity (orange) is computed and the maxima peaks (red marker) and minima points (green marker) are detected. When a Pulse Mode was used the first maximum and the last minimum where considered as light onset and offset, respectively. (b) The CR is estimated as the ratio between the number of local minima in the Box Area divided by the time window. The measurements are computed for pre-stimuli condition (before the red line, that represent the time instant at which the light is turned on), during the light stimuli (between the red line and the green one), and post-stimuli (after the green line, that represents the time point at which the light stimuli is turned off). The subregions are used to verify the reliability of the estimate.*

The modulation of membrane potential was recorded and analysed. The value of the hyperpolarization and depolarization peaks elicited by light onset were extracted, as shown in Fig. 2.4. The V_m modulation is computed as:

$$V_m = V_{m,peak} - V_{m,resting} \tag{2.3}$$

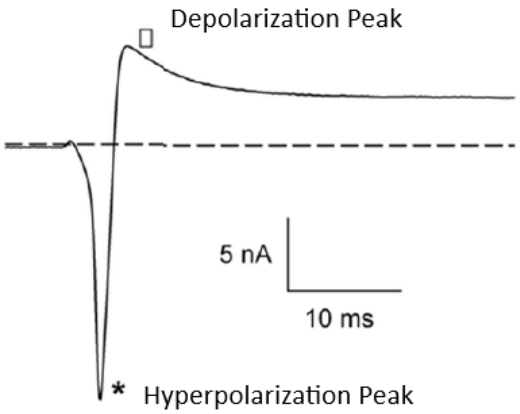

Figura 2.4: Hyperpolarization and depolarization peaks. *The figure shows an example of the electrophysiological signal recorded with a patch-clamp technique. The trace represents the modulation of membrane potential over time. The first negative peak corresponds to the hyperpolarization peak, while the second positive peak is commonly referred to as depolariozation peak.*

Firing activity

The aforementioned light stimulation protocols were used also to verify light-induced generation of APs. hiPSC-CMs that were not spontaneously beating, were enlighted with a specific stimulation protocol five times (i.e. five sweeps). Each time the number of elicited APs was extracted for every single cell, together with the time between light onset and AP upstroke.
Additionally, the *10000 ms* condition was applied to both spontaneously beating or not-spontaneously beating cells to evaluate the effects of the light stimulus on the firing rate.

Membrane Capacitance

Capacitance measurements were performed using the *two-sinusoids approach*. A dual-frequency stimulus was used for estimating membrane capacitance (f_1 = 195.3125 Hz, f_2 = 2 f_1, T = 5.12 ms, A = 10 mV). Two holding potentials were tested: 0 mV and 20 mV. Cells were clamped at resting potential, setting I = 0. Compensation for pipette capacitance was performed. The extraction of capacitance from the measurement is done period-by-period (5.12 ms). The theoretical response to the double-frequency stimulation is calculated in the complex (phasors) domain, as reported by [177], [178].

Briefly, a cell recorded under patch-clamp may be modeled as an equivalent circuit with three unknowns: the passive membrane resistance (R_m), the membrane

capacitance (C_m) and the access resistance of the patch pipette (R_a) (Fig. 2.5) [178].
The equivalent circuit diagram shows that the sum of the current through the cell and the compensation circuit is equal to the current through the current sensor, I_{sensor}.

$$I_{sensor} = V_{sensor}Y_{cell} + (V_{sensor} - V_{comp})Y_{comp} \tag{2.4}$$

where Y indicates the *admittance*. Thus, Y_m is the conductance of the compensation circuit, and Y_{cell} is the conductance of cell/pipette combination. Since V_{comp} is proportional to V_{sensor} ($2V_{sensor}$), the equation 2.4 can be simplified and the measured conductance Y_m can be derived.

$$Y_{cell} - Y_{comp} = I_{sensor}/V_{sensor} = Y_m \tag{2.5}$$

Division of the current[2] by the magnitude of the driving voltage gives the measured conductance, Y_m. Likewise, the conductance of the compensation circuitry Y_{comp} can be directly read from the amplifier. Thus, the cell conductance Y_{cell} is computed. The total *admittance* of the equivalent circuitry composed by cell and pipette can be written as:

$$Y_{cell}(\omega) = \frac{\frac{1}{R_a}(j\omega C_m + \frac{1}{R_m})}{\frac{1}{R_a} + \frac{1}{R_m} + j\omega C_m} \tag{2.6}$$

Dividing the real and imaginary parts of the admittance, it follows:

$$Y_{cell}(\omega) = A + jB = \frac{(1 + j\omega C_m R_m)}{(R_a + R_m + j\omega C_m R_a R_m)} \tag{2.7}$$

where $A = Re(Y_{cell})$, $B = Im(Y_{cell})$.

For each period of the measurements, the values of Cm, Rm and Rs that better fit the data are computed.

Statistical analysis

Statistical analysis were performed in *Origin 8.0* (*OriginLab Corporation*). Mann-Withney U test was performed to assess the significant difference among two populations of data (e.g. to compare the hyperpolarization and depolarization peaks w.r.t. controls).
On the other hand, when the light-induced variation of the firing rate was to be assessed, the Friedman/Dunn's test was performed. This was done since the modulation of the firing rate occurs on the same cell, thus a simple t-test might be not completely appropriate. The Friedman test is a non-parametric statistical test developed to detect differences in treatments across multiple test attempts. The assumptions necessary to apply these statistical tests were checked.

[2]The *in-phase* component of the current, or Real part, as well as the *out-of-phase* component, or Imaginary part, are computed using a lock-in amplifier implemented in Hardware or in Software.

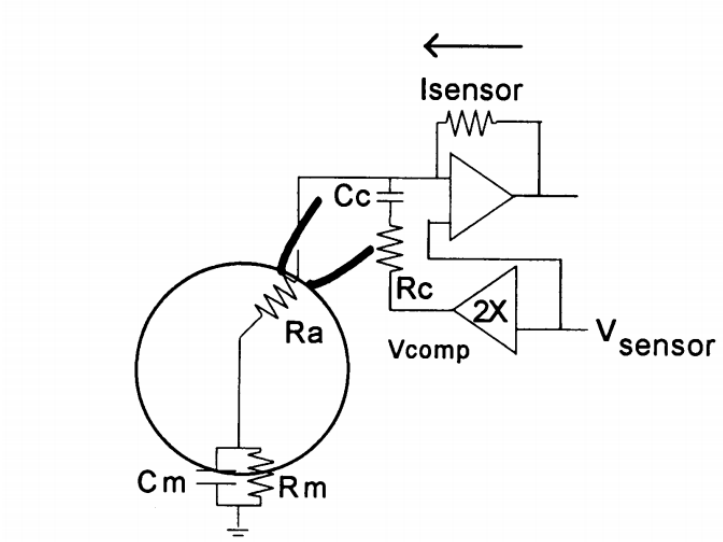

Figura 2.5: Equivalent circuit diagram of a patch-clamped cell. *The cell under study is characterized by a passive membrane resistance (R_m) and membrane capacitance (C_m) and is recorded through a patch pipette having an access resistance (R_a). The current to the patch electrode may be delivered through the current sensor (I_{sensor}) or through the compensation circuit characterized by resistor, R_c, and capacitor C_c. The reference voltage is V_{sensor}. Reproduced from [178]*

2.4 Localization assay

hiPSCs-CMs at day 20 after spontaneous contraction start, were plated on *Mattek* dishes the day before the localization experiment. At the acquisition day, cells were incubated with Ziapin2/DMSO (5 μM) for 7 minutes at 37°C. Then cells were washed with PBS 1X and treated with ER probe (Cell Navigator Live cell endoplasmic reticulum (ER), AAT Bioquest catalog number: 22636), for 30 minutes at 37°C. After that, hiPSCs-CMs were washed three times. Multiple images were acquired with a *Leica TCS SP8 STED 3X* fluorescence microscope and a 63x oil objective. The photochromic molecule, Ziapin2, was excited with a 488 nm laser and the emission spectra were collected in 560-640 nm band. The ER probe, instead, was excited with a 590 nm laser and emission recorded for 620-700 nm. Data were collected with a *HyD SMD 1* detector.
The experiments were conducted at *Humanitas Research Hospital*.

Capitolo 3

Results

The characterization of the cardiac cell model to the light-induced isomerization of Ziapin2 was investigated following three main lines: the analysis of the CR, the electrical activity and the localization of the photoswitch once loaded in hiPSC-CMs.

3.1 Contractility Analysis

Regarding the CR analysis, optical microscopy was exploited to evaluate the effects of Ziapin2 on the cell contraction behavior. To this end, cells were incubated with the molecular photoswitches and, then, video recorded at room temperature during a light stimulation protocol. Video processing enabled the estimation of CR over the stimulation period.

3.1.1 Single stimulation protocol

The *single stimulation* protocol included:

- 60 s only brightfield on;
- 60 s pulsed blue light (470 nm) at 1 Hz;
- 60 s only brightfield on.

For each ROI, the CR was computed at rest, within the 60 s before the light stimulus is turned on (*Pre*); during the light pulses period (*Light*); and after stimulation, within the following 60 s (*Post*).

Ziapin2/DMSO

The following results were obtained using hiPSC-CMs loaded with Ziapin2/DMSO (5 μM), the protocol is explained at Paragraph 2.2.2.
Fig. 3.1 reports three representative beating signals of Ziapin2-loaded hiPSC-CMs during light stimulus. The red line in the plots corresponds to the light onset and the green line to the light offset. Noticeably, a marked increment of CR upon illumination is observed.

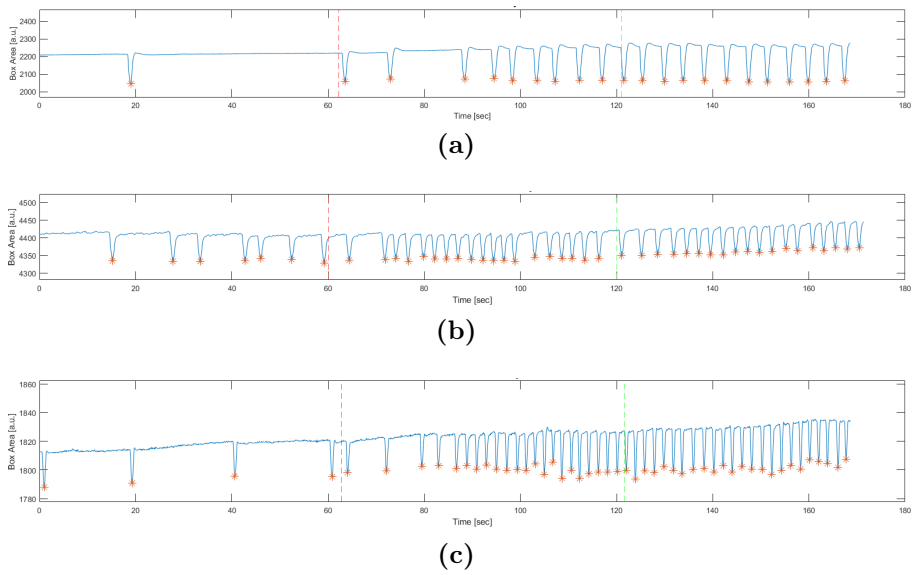

Figura 3.1: Ziapin2-loaded hiPSC-CMs beating signals during light stimuli. *Each trace represent the beating signals recorded from a Ziapin2-loaded hiPSC-CM upon illumination. Beating signal is computed as the area of the box surrounding a cell over the stimulation period (470 nm; 50 mW/mm^2; room temperature). Dashed red line: light onset. Dashed green line: light offset. Orange star: minimum of beating signal, i.e. single contraction. For a complete explanation see Paragraph 2.3.1.*

Full descriptive statistics of collected data are reported in Tab. 3.1. From descriptive statistic, the CR trend across the three time points was computed and plotted in Fig. 3.2a as mean ± s.e.m.

The line chart shows an upward trend, which continues with a less prominent slope even after the light stimulus offset (*Post*). The statistical analysis returned that the mean CR at the three time points in *Ziapin2/DMSO* are not rated equally ($F(df_{time} = 1.34 , df_{error} = 167.56) = 20.49$; p-value = 9.6561 e-7). Precisely, the *post-hoc* Tukey's test reported a statistically significant difference between *Pre* ↔ *Light* and *Pre* ↔ *Post*. Complete Tukey's test outcomes for *Ziapin2/DMSO* condition are reported in Tab. 3.2.

To assess whether the increase in the CR was gradual or instantaneous the light-stimulus (*Light*) and the post-stimulus (*Post*) time windows were divided into two sub-intervals. The CR trend of these sub-intervals is shown in Fig. 3.2b. *Light'* indicates the first 30 *s* after light onset, while *Light"* refers to the second 30 *s* after light onset. The same for *Post'* and *Post"*. As expected, the ascending trend is

Tabella 3.1: Contraction rate in Ziapin2/DMSO-loaded hiPSC-CMs: descriptive statistics for a single stimulation protocol (5μM). *The results are reported in Hz. Ziapin2/DMSO, n = 126*

	Mean	SD	s.e.m.	Minimum	Median	Maximum	IQR
Pre	0,295	0,169	0,015	0	0,302	0,707	0,222
Light	0,332	0,145	0,013	0,051	0,324	0,681	0,204
Post	0,347	0,150	0,013	0,019	0,340	0,713	0,207

confirmed also in the subintervals analysis.

Tabella 3.2: Contraction rate in Ziapin2/DMSO-loaded hiPSC-CMs: statistical analysis for a single stimulation protocol (5μM). *Results of the pairwise comparison test or Tukey's test, i.e. One-Way Anova Repeated Measures post-hoc test. Ziapin2/DMSO (5 μM), n = 126*

Pairs	Mean Diff.	Std. Error	DF	|t| value	Prob. > |t|
Pre ↔ Light	-0.037	0.008	250	6.242	4.5 e-5
Pre ↔ Post	-0.052	0.008	250	8.799	0
Light ↔ Post	-0.015	0.008	250	2.557	0.169

Remarkably, the CRs of those cells, that were not spontaneously beating before light stimulus, raise from 0 Hz to an average value of 0.28 Hz (mean ± s.e.m. $0,283 \pm 0,067 Hz$, n = 8) during *Light* condition, and 0.32 Hz (mean ± s.e.m. $0,324 \pm 0,076 Hz$, n = 8) one minute after light offset (*Post*). The time between light onset and the first contraction event was estimated for these spontaneously-not-beating cells. Interestingly, the estimated time-to-first-contractions were almost equals among the different cells. The mean delay oscillates around a mean value of 1.36 s. (mean ± s.e.m. $1,36 \pm 0,051 s$, n = 8).

To further investigate this behavior, the estimated CR was plotted on a Cartesian plane (Fig. 3.3). Each point on the scatterplots represents a cell, and the coordinates are given by the CR at rest and the CR during the stimulus (Fig. 3.3a) or post stimulus (Fig. 3.3b). The two scatterplots show that the majority of the points lie near the bisector, except for a cluster of cells which shows a more pronounced light-induced increase of CR. Remarkably, the hiPSC-CMs that belong to this highly-responding cluster of cells present a low resting CR. The CR modulation during the light stimulus and post stimulus is computed for each cell respectively as $(CR_{Light} - CR_{Pre})$ and $(CR_{Post} - CR_{Pre})$. The relative frequency histograms are reported in Fig.3.4. More than 60% of cells show a positive raise in the CR from resting condition to light stimulation. This percentage increased to 70%, when the CR_{Post} and CR_{Pre} are compared.

Two control experiments were performed. Firstly, the same light stimuli protocol was applied to hiPSC-CMs in the absence of Ziapin2, in order to assess whether the observed effects on the CR were due to a general light-induced effect (e.g. overheating) or to the presence of Ziapin2. Second, Ziapin2/DMSO-loaded hiPSC-CMs were recorded for three minutes without light stimuli to see if the CR changes over time. This latter condition was used to verify if Ziapin2 has an effect on the

Tabella 3.3: Control conditions in Ziapin2/DMSO-loaded hiPSC-CMs. *Mean ± s.e.m. CR estimated over the three time points. Data are reported in Hz. Ziapin2/DMSO (5 μM): n = 126; Ziapin2/DMSO Ctrl: n = 25; Light Ctrl: n=43.*

	Ziapin2/DMSO	Ziapin2/DMSO Ctrl	Light Ctrl
Pre	0,295 ± 0,015	0,149 ± 0,016	0,233 ± 0,009
Light	0,332 ± 0,013	0,146 ± 0,015	0,226 ± 0,010
Post	0,347 ± 0,013	0,14778 ± 0,016	0,225 ± 0,009

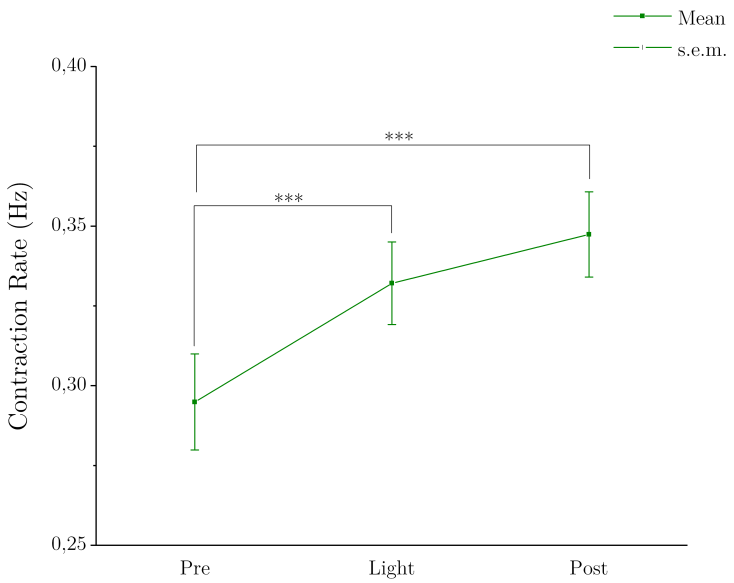

(a)

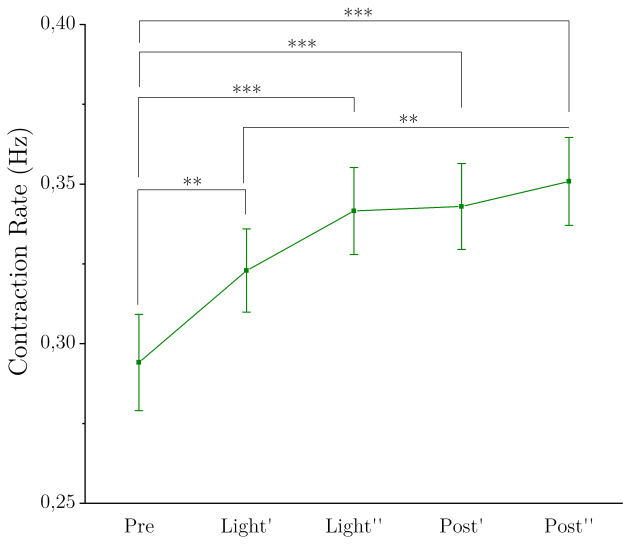

(b)

Figura 3.2: Light-induced contraction rate trend in Ziapin2/DMSO-loaded hiPSC-CMs: single stimulation protocol (5μM). *(a) The line chart shows the mean CR of optically stimulated Ziapin2-loaded hiPSC-CMs at rest (Pre), during light stimulus (Light) and after light offset (Post). (b) The minute of stimulation and the minute following the light offset were divided into two sub-intervals. One apostrophe indicates the first 30 s of the specific period; two marks refer to the second 30 s. The mean value is obtained as average of the analyzed ROIs. Ziapin2/DMSO (5 μM), n = 126. Statistical tests: One-Way Anova Repeated Measures. * P <0.05; ** P<0.005; *** P<0.0005.*

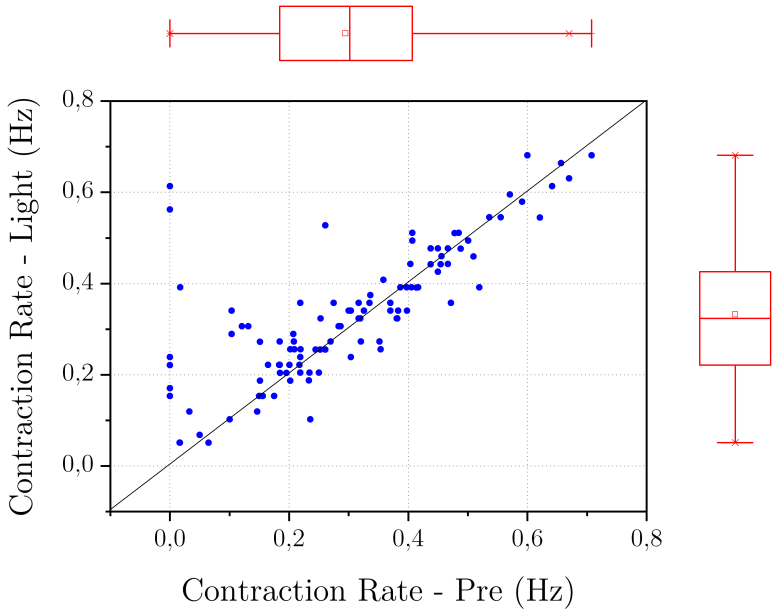

(a)

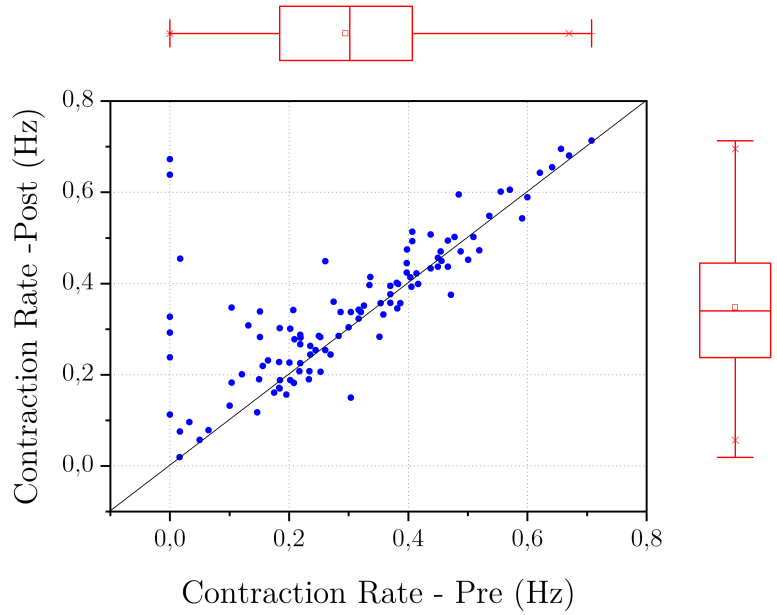

(b)

Figura 3.3: ***Light-induced contraction rate modulation in Ziapin2/DMSO-loaded hiPSC-CMs as function of resting condition (5μM).*** *Each point of the scatterplot corresponds to a ROI, ideally a cell. The scatter diagram uses as Cartesian coordinates, the values of estimated CR at rest (Pre) and (a) during the light stimulus (Light) or (b) after it (Post). Ziapin2/DMSO (5 μM), n = 126*

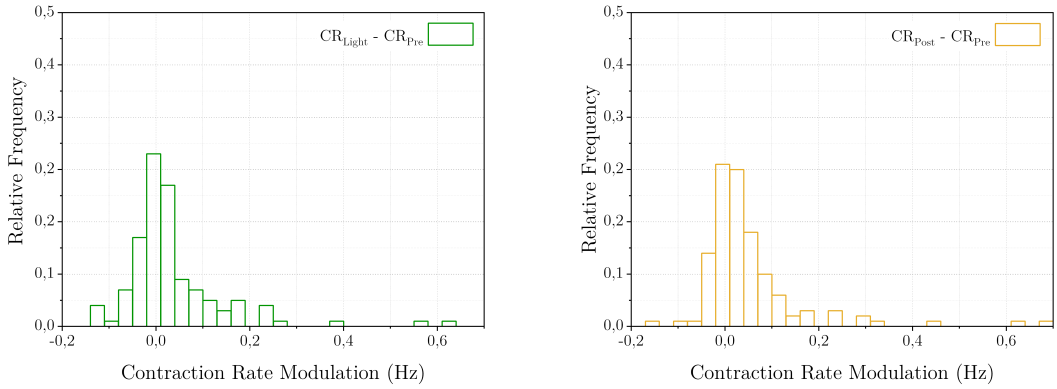

Figura 3.4: Relative frequency histogram of light-induced contraction rate modulation in Ziapin2/DMSO-loaded hiPSC-CMs (5µM). *Contraction rate modulation is intended as* ΔCR*. Light:* $(CR_{Light} - CR_{Pre})$*; Post:* $(CR_{Post} - CR_{Pre})$*. Ziapin2/DMSO (5* μM*),* $n = 126$

contraction behavior by itself or not. It is worth to be mentioned that this control might be not comprehensive, given that the brightfield, used for video microscopy, might partially elicit the photoisomerization of Ziapin2 or other optically-triggered phenomena. Data for the two control conditions are reported in Tab 3.3. Note that in *Ziapin2/DMSO Ctrl* the light was never turned on and, thus, the terms *Pre*, *Light*, *Post* are meaningless. In this condition, the three time points should

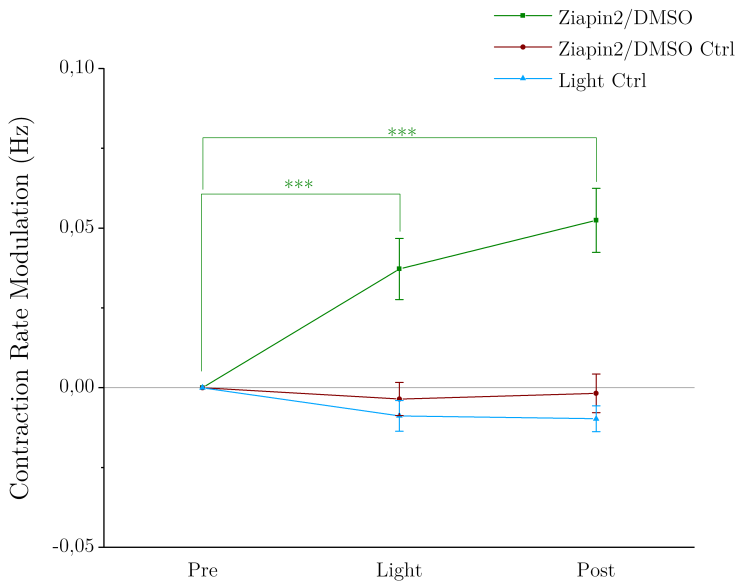

Figura 3.5: Light-induced contraction rate modulation in Ziapin2/DMSO-loaded hiPSC-CMs. *Contraction rate modulation is intended as* ΔCR*. Pre:* $(CR_{Pre} - CR_{Pre})$*; Light:* $(CR_{Light} - CR_{Pre})$*; Post:* $(CR_{Post} - CR_{Pre})$*. Ziapin2/DMSO (5* μM*):* $n = 126$*; Ziapin2/DMSO Ctrl:* $n = 25$*; Light Ctrl:* $n=43$*. Statistical tests: One-Way Anova Repeated Measures. * P <0.05; ** P<0.005; *** P<0.0005.*

be considered as *0-60 s*, *60-120 s*, *120-180 s*. This condition simply evaluate the variation over a three-minutes-period of the CR of Ziapin2-loaded hiPSC-CMs in the absence of a light stimulus.

Fig. 3.5 shows the modulation of the CR for the optically stimulated Ziapin2-loaded hiPSC-CMs (*Ziapin2/DMSO*) and the two control conditions (*Light Ctrl*, *Ziapin2/DMSO Ctrl*). Looking at the chart, it seems likely that in the two control conditions the CR is almost constant over the three minutes of recording. Accordingly, no significant difference is detected between the three time points in the two controls (One-way Anova Repeated Measures P>0.05).

Ziapin2/H_2O (5 μM)

As mentioned above, the hiPSC-CMs CR analysis was performed also with Ziapin2/H_2O (5 μM), using the same loading procedure and stimulation protocols. Tab. 3.4 shows the descriptive statistics of CR estimate of Ziapin/H_2O-loaded hiPSC-CMs.

Tabella 3.4: Contraction rate in Ziapin2/H_2O-loaded hiPSC-CMs: descriptive statistics for a single stimulation protocol (5μM). *The results are reported in Hz. Ziapin2/H_2O (5 μM): n = 203*

	Mean	SD	s.e.m.	Minimum	Median	Maximum	IQR
Pre	0,201	0,081	0,006	0,042	0,205	0,399	0,119
Light	0,208	0,077	0,005	0,051	0,219	0,412	0,110
Post	0,204	0,070	0,005	0,023	0,203	0,360	0,091

Conversely from Ziapin2/DMSO, loading the cell with Ziapin2/H_2O (5) provides a much lower effect. The line chart in Fig. 3.6a shows a slight increase during light stimulus, that decrease shortly after the light offset (*Post*). The One-Way Anova Repeated Measures analysis returned a statistically significant difference between the CR during the light stimulus and the resting condition (F(DF_{time} = 2, DF_{error} = 404) = 3.233 ; p-value = .040). Precisely, the *post-hoc* Tukey's test reported a statistically significant difference at level .03 between *Pre* ↔ *Light*. Complete Tukey's test outcomes for this condition are reported in Tab. 3.5.

The sub-intervals CR is shown in Fig. 3.6b. Dividing the three-minutes periods in sub-intervals, the line chart confirm the presence of a modest gradual increase in CR during the light stimulus.

Tabella 3.5: Contraction rate in Ziapin2/H_2ODMSO-loaded hiPSC-CMs: statistical analysis for a single stimulation protocol (5μM). *Results of the pairwise comparison test or Tukey's test, i.e. One-Way Anova Repeated Measures post-hoc test. Ziapin2/H_2O (5 μM): n = 203*

Pairs	Mean Diff.	Std. Error	DF	|t| value	Prob. > |t|
Pre ↔ Light	-0,008	0,003	404	3,594	0,031
Pre ↔ Post	-0,004	0,003	404	1,700	0,453
Light ↔ Post	-0,004	0,003	404	1,895	0,374

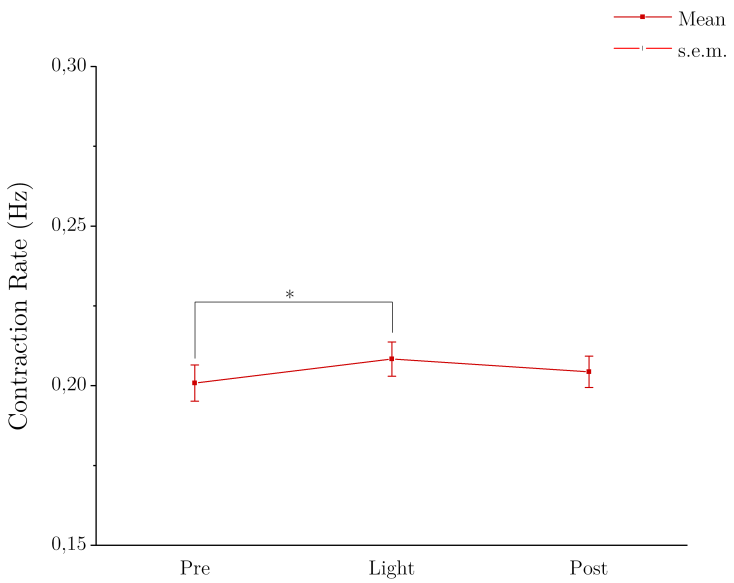

(a)

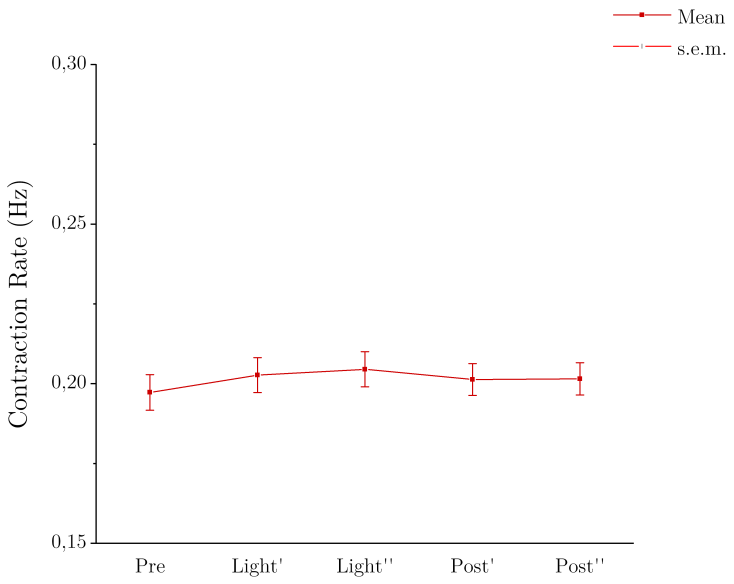

(b)

Figura 3.6: Light-induced contraction rate trend in Ziapin2/H_2O-loaded hiPSC-CMs: single stimulation protocol (5μM). *(a) The line chart shows the mean CR of optically stimulated Ziapin2-loaded hiPSC-CMs at rest (Pre), during light stimulus (Light) and after light offset (Post). (b) The minute of stimulation and the minute following the light offset were divided into two sub-intervals. One apostrophe indicates the first 30 s of the specific period; two marks refer to the second 30 s. The mean value is obtained as average of the analyzed ROIs. Ziapin2/H_2O (5 μM): n = 203. Statistical tests: One-Way Anova Repeated Measures. * P <0.05; ** P<0.005; *** P<0.0005.*

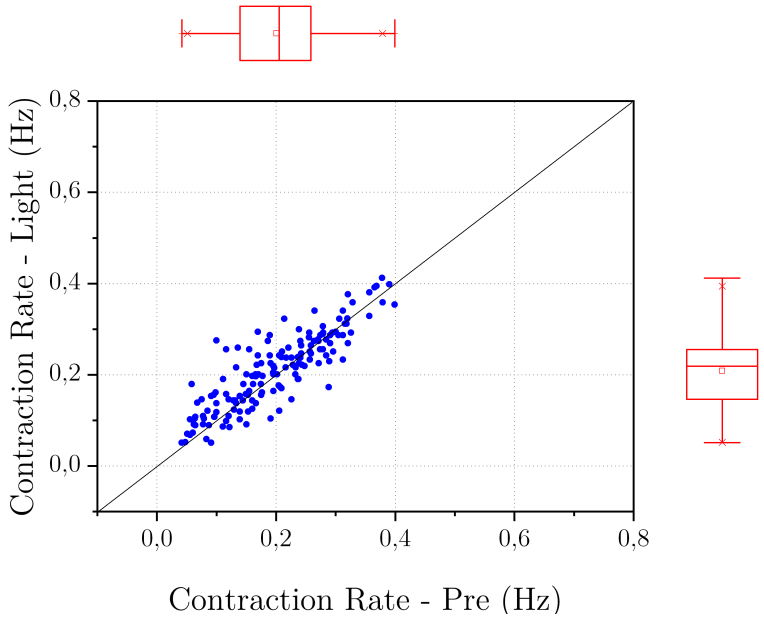

(a)

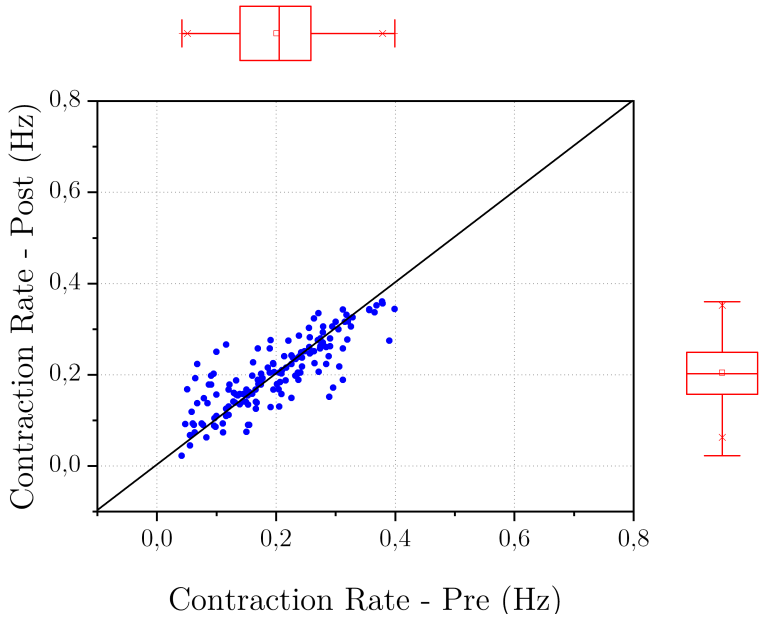

(b)

Figura 3.7: Light-induced contraction rate modulation in Ziapin2/H_2O-loaded hiPSC-CMs as function of resting condition (5μM). *Each point of the scatterplot corresponds to a ROI, ideally a cell. The scatter diagram uses as Cartesian coordinates, the values of estimated CR at rest (Pre) and (a) during the light stimulus (Light) or (b) after it (Post). Ziapin2/H_2O (5 μM): n = 203*

The scatterplot diagrams (Fig. 3.7) show that there is a cluster of cells for low resting CR that stand out from the rest of the cells. The cells that belong to

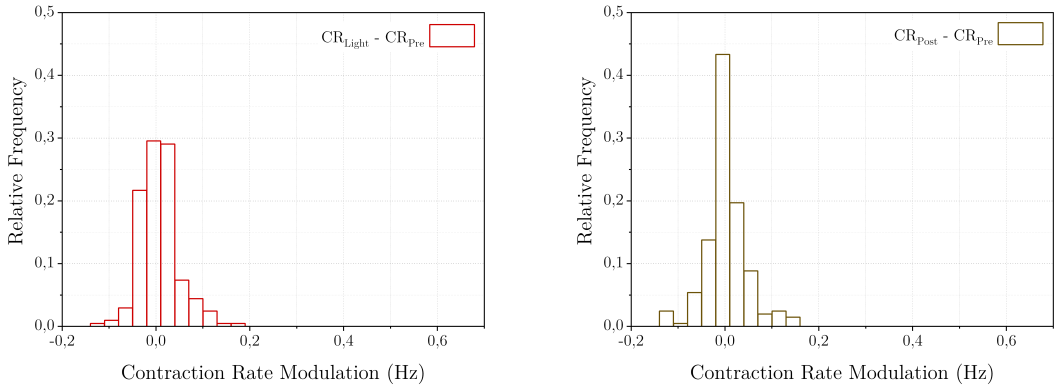

(a) **(b)**

Figura 3.8: Relative frequency histogram of light-induced contraction rate modulation in Ziapin2/H_2O -loaded hiPSC-CMs (5μM). *Contraction rate modulation is intended as ΔCR. Light: ($CR_{Light} - CR_{Pre}$); Post: ($CR_{Post} - CR_{Pre}$). Ziapin2/H_2O (5 μM): n = 203*

this cluster increase their CRs slightly more w.r.t. the others. This is even more evident in 3.7b, where the CR after the light offset is plotted as function of the resting contraction frequency. Despite this cluster of cells, the histogram reporting the relative frequency of the CR modulation (or ΔCR) show an almost normal distribution around 0 Hz that differ from the right-skewed distributions observed for Ziapin2/DMSO (Fig. 3.4). This time, about half of cells increase their CR during light stimulus and post light stimulus. Most of the cells, that do not increase their CR, simply do not change the contraction frequency.

Tabella 3.6: Control conditions in Ziapin2/H_2O-loaded hiPSC-CMs. *Mean ± s.e.m. CR estimated over the three time points. Data are reported in Hz. Ziapin2/H_2O (5 μM): n = 203; Ziapin2/H_2O Ctrl: n = 53; Light Ctrl: n=43.*

	Ziapin2/H_2O	**Ziapin2/H_2O Ctrl**	**Light Ctrl**
Pre	0,201 ± 0,006	0,255 ± 0,023	0,233 ± 0,009
Light	0,208 ± 0,005	0,244 ± 0,021	0,226 ± 0,010
Post	0,204 ± 0,005	0,239 ± 0,020	0,225 ± 0,009

The results were compared to the two control conditions. As for Ziapin2/DMSO, the same light stimuli protocol was applied to hiPSC-CMs in the absence of Ziapin2, in order to assess whether the observed effects on the CR were due to a general light-induced effect (e.g. overheating) or to the photo-induced isomerization of Ziapin2. Second, Ziapin2/H_2O-loaded hiPSC-CMs were recorded for three minutes without light stimuli to see if the CR changes over time. The CR estimates for the three treatments are reported in Tab 3.6. Note that, as mentioned above, in *Ziapin2/H_2O Ctrl* the light was never turned on and, thus, the terms *Pre*, *Light*, *Post* should be considered as *0-60 s*, *60-120 s*, *120-180 s*. The reported values show that there is a small increase in the mean CR estimate in Ziapin2/H_2O, that it is not observed in the control conditions. On the contrary, the control values tend to decrease slightly over the three-minutes acquisition (Fig. 3.9). This descending

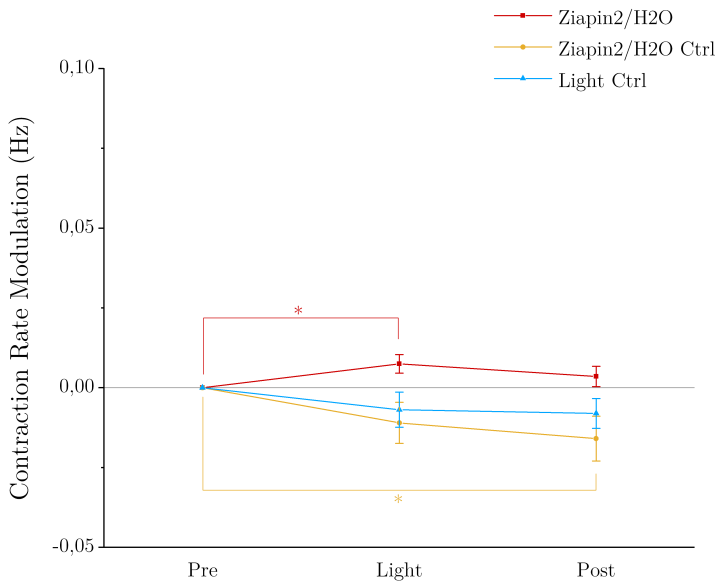

Figura 3.9: Light-induced contraction rate modulation in Ziapin2/H_2O-loaded hiPSC-CMs. *Contraction rate modulation is intended as ΔCR. Pre: ($CR_{Pre} - CR_{Pre}$); Light: ($CR_{Light} - CR_{Pre}$); Post: ($CR_{Post} - CR_{Pre}$). Ziapin2/H_2O (5 μM): n = 203; Ziapin2/H_2O Ctrl: n = 53; Light Ctrl: n=43. Statistical tests: One-Way Anova Repeated Measures. * P <0.05; ** P<0.005; *** P<0.0005.*

trend is striking for the Ziapin2/H_2O Ctrl condition, which shows that the mean CR modulation post light stimulus is significantly different from the modulation at rest *Pre*, that means the zero modulation (One-way Anova Repeated Measures P<0.05).

Ziapin2/H_2O (25 μM)

To explore whether the reduced CR modulation was due to a different amount of molecules internalized by cells, the *single stimulation* protocol was repeated on hiPSC-CMs loaded with Ziapin2/H_2O (25 μM). The following results are referred to this loading condition (Tab. 3.7).

Tabella 3.7: Contraction rate in Ziapin2/H_2O-loaded hiPSC-CMs: descriptive statistics for a single stimulation protocol (25 μM). *The results are reported in Hz. Ziapin2/H_2O (25 μM): n = 202*

	Mean	SD	s.e.m.	Minimum	Median	Maximum	IQR
Pre	0,159	0,099	0,007	0	0,156	0,396	0,154
Light	0,176	0,089	0,006	0,017	0,170	0,398	0,136
Post	0,184	0,094	0,007	0,018	0,179	0,415	0,137

As shown in Fig. 3.10a, a higher concentration of Ziapin2/H_2O restores the sharp increase observed with Ziapin2/DMSO. The line chart, together with the sub-interval diagram 3.10b, show an upward trend of the mean CR during the three-

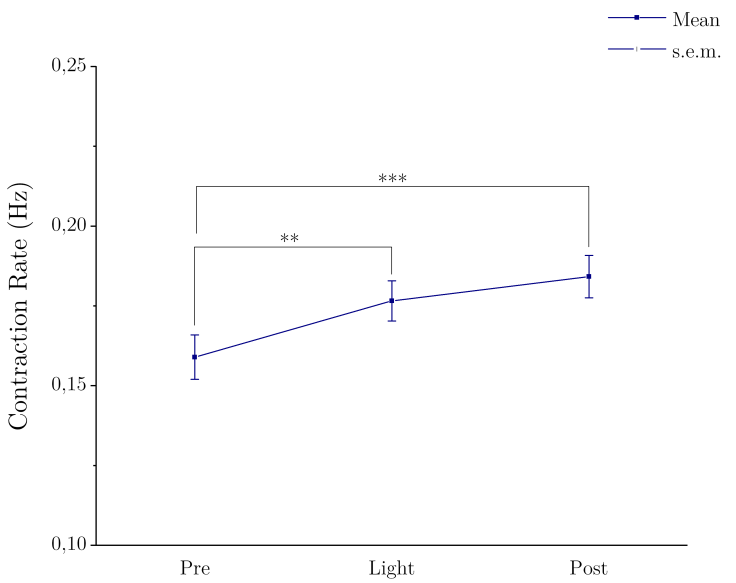

(a)

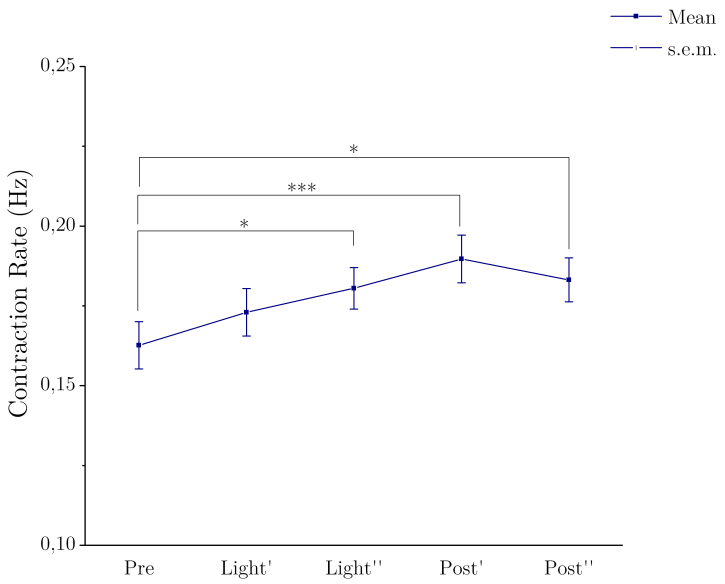

(b)

Figura 3.10: Light-induced contraction rate trend in Ziapin2/H_2O-loaded hiPSC-CMs: single stimulation protocol (25 μM). *(a) The line chart shows the mean CR of optically stimulated Ziapin2-loaded hiPSC-CMs at rest (Pre), during light stimulus (Light) and after light offset (Post). (b) The minute of stimulation and the minute following the light offset were divided into two sub-intervals. One apostrophe indicates the first 30 s of the specific period; two marks refer to the second 30 s. The mean value is obtained as average of the analyzed ROIs. Ziapin2/H_2O (25 μM): n = 202. Statistical tests: One-Way Anova Repeated Measures. * P <0.05; ** P<0.005; *** P<0.0005.*

minutes protocol. To be more precise, the mean CR starts to increase when the pulsed blue light is applied (*Light*) and the increment continues during the first 30 *s* after the light offset (*Post'*). Interestingly, the mean CR begins to decrease after 30 *s* from the light onset. This drop in the mean CR is different from what was observed in Ziapin2/DMSO condition (Fig. 3.2b). One-Way Anova Repeated Measures analysis returned that the three time points are ranked differently ($F(DF_{time} = 1.56, DF_{error} = 314.25) = 11.70$; p-value = 7.10 e-5). Precisely, the *post-hoc* Tukey's test reported a statistically significant difference between *Pre* $\leftrightarrow$ *Light*, as well as, *Pre* $\leftrightarrow$ *Post*. Complete Tukey's test outcomes are reported in Tab. 3.8.

Tabella 3.8: Contraction rate in Ziapin2/H_2O-loaded hiPSC-CMs: statistical analysis for a single stimulation protocol (25 μM). *Results of the pairwise comparison test or Tukey's test, i.e. One-Way Anova Repeated Measures post-hoc test. Ziapin2/H_2O (25 μM): n = 202*

Pairs	Mean Diff.	Std. Error	DF	|t| value	Prob. > |t|
Pre $\leftrightarrow$ Light	-0,018	0,005	402	3,298	0,003
Pre $\leftrightarrow$ Post	-0,025	0,005	402	4,714	1,007 e-5
Light $\leftrightarrow$ Post	-0,008	0,005	402	1,426	0,472

The scatterplot diagrams (Fig. 3.12) present a highly-responding cluster of cells for low initial CR. Note that the distribution of the CR in both scatterplots is less spread than in Ziapin2/DMSO (Fig. 3.3). In Fig. 3.11 are reported the histogram reporting the relative frequency of the CR modulation (or ΔCR). The increments are distributed around zero, whit about 60% of the cells showing a positive increment w.r.t. the initial condition.

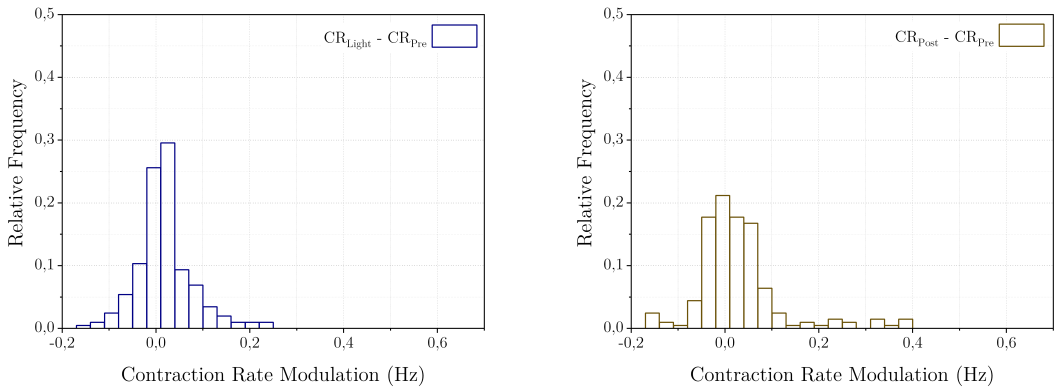

(a) **(b)**

Figura 3.11: Relative frequency histogram of light-induced contraction rate modulation in Ziapin2/H_2O-loaded hiPSC-CMs (25 μM). *Contraction rate modulation is intended as ΔCR. Light: ($CR_{Light} - CR_{Pre}$); Post: ($CR_{Post} - CR_{Pre}$). Ziapin2/H_2O (25 μM): n = 202*

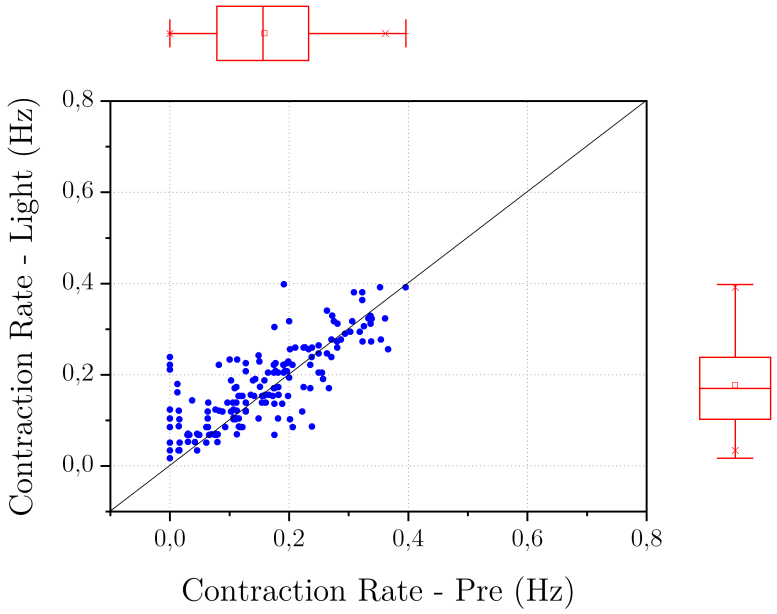

(a)

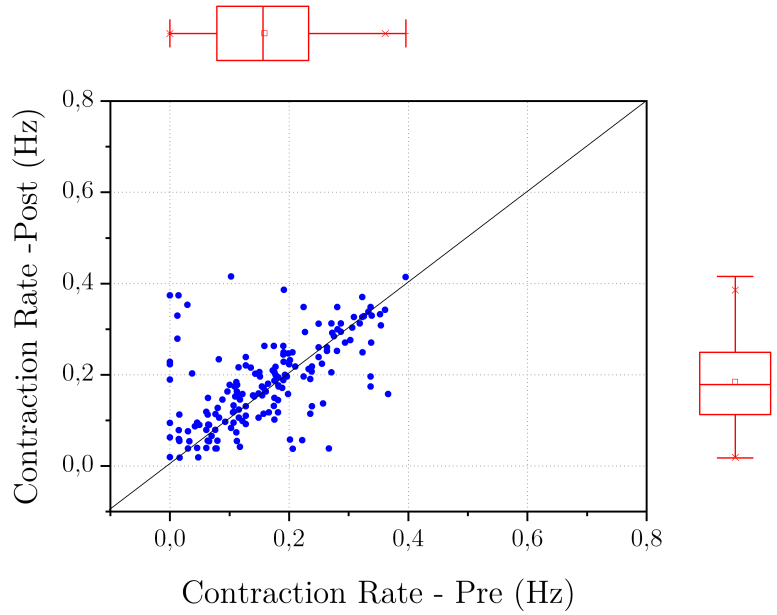

(b)

Figura 3.12: ***Light-induced contraction rate modulation in Ziapin2/H_2O -loaded hiPSC-CMs as function of resting condition (25 μM).*** *Each point of the scatterplot corresponds to a ROI, ideally a cell. The scatter diagram uses as Cartesian coordinates, the values of estimated CR at rest (Pre) and (a) during the light stimulus (Light) or (b) after it (Post). Ziapin2/H_2O (25 μM): $n = 203$*

3.1.2 Double stimulation protocol

In order to verify whether the light-induced effects were preserved even after the first light stimuli or not, a *double stimulation* protocol was performed. The overall stimulation included:

- 60 s only brightfield on;
- 60 s pulsed blue-light (470 nm) at 1 Hz;
- 60 s only brightfield on.
- 60 s only brightfield on;
- 60 s pulsed blue-light (470 nm) at 1 Hz;
- 60 s only brightfield on.

For each ROI, the CR was computed at rest, within the 60 s before the light stimulus is turned on (*Pre*); during the first light pulses time window (*Light*); after the stimulation, within the following 60 s (*Post*) and within the next 60 s (*Post"*); during the second light pulses period (*Light 2*); and after this second stimulation, within the following 60 s (*Post 2*).

Ziapin2/DMSO

The following results were obtained using hiPSC-CMs loaded with Ziapin2/DMSO. Descriptive statistics of the collected CR over the six-minutes protocol are reported in Tab. 3.9. The trend of the CR is visually represented in Fig. 3.13. As expected from the previous analysis with *single stimulation* protocol, there is a noticeable raise in the CR after the blue light onset. The trend proceed in the first minute after the light offset, but decrease shortly after (*Post"*). When the light stimulus is applied again (*Light 2*), the CR increases again to a value that exceed on average the previous peak value. The statistical analysis returned that the CR means are statistically different ($F(DF_{time} = 2.47, DF_{error} = 231.99) = 10.890$; p-value = 6.020 e-6).

In particular, the results obtained from the pairwise comparison, carried out with the *post-hoc* Tukey's test, suggest that the mean for the *Pre* condition differs

Tabella 3.9: Contraction rate in Ziapin2/DMSO-loaded hiPSC-CMs: descriptive statistics for double stimulation protocol (5μM). *The results are reported in Hz. Ziapin2/DMSO (5 μM): n = 95*

	Mean	SD	s.e.m.	Minimum	Median	Maximum	IQR
Pre	0,287	0,153	0,016	0	0,3	0,621	0,214
Light	0,317	0,134	0,014	0,051	0,324	0,613	0,170
Post	0,332	0,136	0,014	0,057	0,339	0,643	0,197
Post"	0,304	0,126	0,013	0	0,311	0,562	0,176
Light 2	0,326	0,122	0,013	0,053	0,308	0,571	0,154
Post 2	0,337	0,131	0,013	0,054	0,348	0,622	0,188

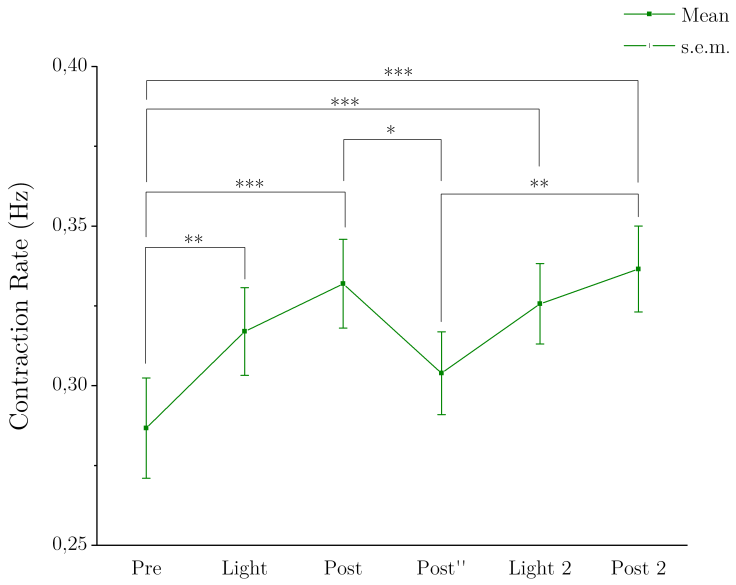

Figura 3.13: Light-induced contraction rate trend in Ziapin2/DMSO-loaded hiPSC-CMs: double stimulation protocol (5μM). *The line chart shows the mean CR of optically stimulated Ziapin2-loaded hiPSC-CMs at rest (Pre), during first light stimulus (Light), after first light stimulus offset (Post and Post"). during the second light stimulus (Light 2) and after the second light stimulus offset (Post 2). The mean value is obtained as average of the analyzed ROIs. Ziapin2/DMSO (5 μM): n = 95. Statistical tests: One-Way Anova Repeated Measures. * P <0.05; ** P<0.005; *** P<0.0005.*

Tabella 3.10: Contraction Rate in Ziapin2/DMSO-loaded hiPSC-CMs: statistical analysis for double stimulation protocol (5μM). *Results of the pairwise comparison test or Tukey's test, i.e. One-Way Anova Repeated Measures post-hoc test. Ziapin2/DMSO (5 μM): n = 95*

Pairs	Mean Diff.	Std. Error	DF	|t| value	Prob. > |t|
Pre ↔ Light	-0,030	0,008	470	5,315	0,003
Pre ↔ Post	-0,045	0,008	470	7,935	5,0 e-7
Pre ↔ Post"	-0,017	0,00806	470	3,023	0,270
Pre ↔ Light 2	-0,039	0,008	470	6,834	2,7 e-5
Pre ↔ Post 2	-0,050	0,008	470	8,746	1,6 e-8
Light ↔ Post	-0,00149	0,008	470	2,620	0,433
Light ↔ Post"	0,013	0,008	470	2,292	0,169
Light ↔ Light 2	-0,009	0,008	470	1,519	0,892
Pre ↔ Post 2	-0,020	0,008	470	3,431	0,149
Post ↔ Post"	0,028	0,008	470	4,913	0,007
Post ↔ Light 2	0,006	0,008	470	1,101	0,971
Post ↔ Post 2	-0,005	0,008	470	0,811	0,993
Post" ↔ Light 2	-0,022	0,008	470	3,811	0,078
Post" ↔ Post 2	-0,033	0,008	470	5,724	8,5 e-4
Light 2 ↔ Post 2	0,012	0,008	470	1,913	0,755

from both *Light* mean, *Post* mean, *Light 2* mean and *Post 2* mean. Additionally, significant difference is also detected between *Post* and *Post"*, which confirm that the CR is decreasing significantly during the second minutes after the light offset. Finally, significant difference is detected between *Post"* and *Post 2* means. The latter demonstrating that the light effects are still significant even after the first light stimulus. The results of the Tukey's test are reported in Tab. 3.10.

Ziapin2/H_2O (5 μM)

The following results were obtained using hiPSC-CMs loaded with Ziapin2/H_2O. Descriptive statistics of the collected CR over the six-minutes protocol are reported in Tab. 3.11. The trend of the CR is visually represented in Fig. 3.14. The line chart shows a partial increase of CR during the first light stimulus, followed by a sharp decrease in the CR at the light offset. The CR, then, increases again during the second stimulation protocol. Noticeably, since the mean CR before the administration of the second light stimulus (*Post"*) is lower than the resting CR (*Pre*), the increase during the second stimulation is not sufficient to reach the initial mean CR.

Tabella 3.11: Contraction rate in Ziapin2/H_2O-loaded hiPSC-CMs: descriptive statistics for double stimulation protocol (5μM). *The results are reported in Hz. Ziapin2/H_2O (5 μM): n = 124*

	Mean	SD	s.e.m.	Minimum	Median	Maximum	IQR
Pre	0,196	0,076	0,007	0,051	0,191	0,399	0,120
Light	0,208	0,071	0,006	0,051	0,216	0,381	0,110
Post	0,201	0,068	0,006	0,074	0,193	0,344	0,097
Post"	0,159	0,055	0,005	0,054	0,152	0,290	0,084
Light 2	0,165	0,059	0,005	0,045	0,153	0,309	0,088
Post 2	0,171	0,058	0,005	0,046	0,170	0,314	0,077

One-way Anova Repeated Measures was performed to assess whether there was a statistically significant difference between mean CRs over the six-minutes period. The analysis returned that the CR means are not rated equally (F(DF_{time} = 4.31, DF_{error} = 530.33) = 56.197; p-value = 7.219 e-42). As expected the pairwise comparison, carried out with the *post-hoc* Tukey's test (Tab. 3.12), highlights a significant difference among all the time points inter-stimulation (e.g. CR_{Pre} is significantly different from $CR_{Post''}$, CR_{Light2}, CR_{Post2}). Besides that, what is more interesting to observe is that the modest increment observed during the second stimulation protocol is significant.

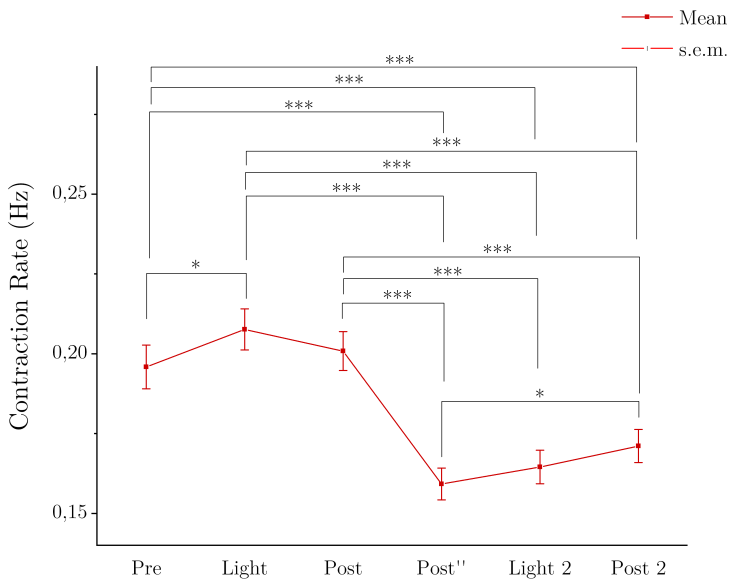

Figura 3.14: Light-induced contraction rate trend in Ziapin2/H_2O-loaded hiPSC-CMs: double stimulation protocol (5μM). *The line chart shows the mean CR of optically stimulated Ziapin2-loaded hiPSC-CMs at rest (Pre), during first light stimulus (Light), after first light stimulus offset (Post and Post"). during the second light stimulus (Light 2) and after the second light stimulus offset (Post 2). The mean value is obtained as average of the analyzed ROIs. Ziapin2/H_2O (5 μM): n = 124. Statistical tests: One-Way Anova Repeated Measures. * P <0.05; ** P<0.005; *** P<0.0005.*

Tabella 3.12: Contraction rate in Ziapin2/H_2O-loaded hiPSC-CMs: statistical analysis for double stimulation protocol (5μM). *Results of the pairwise comparison test or Tukey's test, i.e. One-Way Anova Repeated Measures post-hoc test. Ziapin/H_2O (5 μM): n = 124*

Pairs	Mean Diff.	Std. Error	DF	|t| value	Prob > |t|
Pre ↔ Light	-0,012	0,004	615	4,249	0,033
Pre ↔ Post	-0,005	0,004	615	1,794	0,802
Pre ↔ Post"	0,037	0,004	615	13,297	4,393 e-9
Pre ↔ Light 2	0,031	0,004	615	11,366	6,825 e-9
Pre ↔ Post 2	0,025	0,004	615	8,986	1,640 e-8
Light ↔ Post	0,007	0,004	615	2,455	0,508
Light ↔ Post"	0,048	0,004	615	17,545	0
Light ↔ Light 2	0,043	0,004	615	15,615	1,142 e-9
Pre ↔ Post 2	0,037	0,004	615	13,235	4,467 e-9
Post ↔ Post"	0,042	0,004	615	15,090	1,644 e-9
Post ↔ Light 2	0,036	0,004	615	13,160	4,556 e-9
Post ↔ Post 2	0,030	0,004	615	10,780	7,627 e-9
Post" ↔ Light 2	-0,005	0,004	615	1,930	0,748
Post" ↔ Post 2	-0,011	0,004	615	4,310	0,029
Light 2 ↔ Post 2	-0,007	0,004	615	2,380	0,544

Ziapin2/H_2O (25 μM)

The following results were obtained using hiPSC-CMs loaded with Ziapin2/H_2O (25 μM). Descriptive statistics of the collected CR over the six-minutes protocol are reported in Tab. 3.13. The trend of the CR (Fig. 3.13) shows a marked raise in the CR after the blue light onset. This ascending trend proceeds slightly after the light offset, but it decreases dramatically after two minutes from light offset (*Post"*). Interestingly, despite the sharp decrease observed in the mean CR upon light offset, when the light stimulus is administered for the second round (*Light 2*), the CR increases again with a significant difference between *Post"* and *Post 2*.

Tabella 3.13: Contraction rate in Ziapin2/H_2O-loaded hiPSC-CMs: descriptive statistics for double stimulation protocol (25μM). *The results are reported in Hz. Ziapin2/DMSO (25 μM): n = 179*

	Mean	SD	s.e.m.	Minimum	Median	Maximum	IQR
Pre	0,165	0,097	0,007	0	0,160	0,396	0,141
Light	0,176	0,087	0,006	0,017	0,170	0,392	0,135
Post	0,186	0,092	0,007	0,019	0,180	0,415	0,146
Post"	0,150	0,073	0,005	0,012	0,143	0,350	0,109
Light 2	0,155	0,073	0,005	0	0,150	0,358	0,107
Post 2	0,164	0,075	0,006	0,021	0,172	0,382	0,115

The One-Way Anova Repeated Measure statistical test returned a statistically significant difference among the mean CR over the six-minutes protocol (F(DF_{time} = 1, DF_{error} = 178) = 15,546; p-value = 1,156 e-4). The pairwise comparison, carried out with the *post-hoc* Tukey's test (Tab. 3.14), highlights the presence of a significant difference among the mean CR during the first stimulation and the second one (e.g. CR_{Post} was found to be significantly different from $CR_{Post''}$, CR_{Light2}, CR_{Post2}). Additionally, a significant difference is observed between the pre-stimulus condition and the post-stimulus, either for the first stimulation round or for the second round.

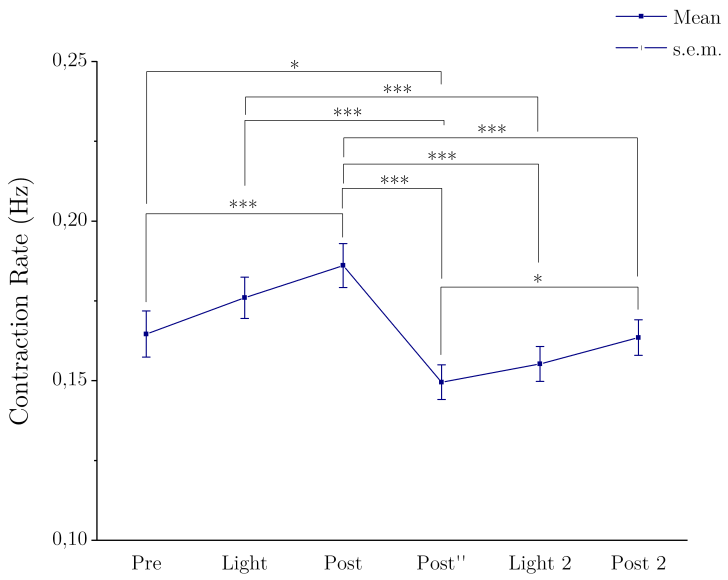

Figura 3.15: Light-induced contraction rate trend in Ziapin2/H_2O-loaded hiPSC-CMs: double stimulation protocol (25μM). *The line chart shows the mean CR of optically stimulated Ziapin2-loaded hiPSC-CMs at rest (Pre), during first light stimulus (Light), after first light stimulus offset (Post and Post"). during the second light stimulus (Light 2) and after the second light stimulus offset (Post 2). The mean value is obtained as average of the analyzed ROIs. Ziapin2/H_2O (25 μM): n = 179. Statistical tests: One-Way Anova Repeated Measures. * P <0.05; ** P<0.005; *** P<0.0005.*

Tabella 3.14: Contraction rate in Ziapin2/H_2O-loaded hiPSC-CMs: statistical analysis for double stimulation protocol (25μM). *Results of the pairwise comparison test or Tukey's test, i.e. One-Way Anova Repeated Measures post-hoc test. Ziapin2/DMSO (25 μM): n = 179*

Pairs	Mean Diff.	Std. Error	DF	|t| value	Prob. > |t|
Pre ↔ Light	-0,011	0,005	890	3,344	0,170
Pre ↔ Post	-0,021	0,005	890	6,321	1,288 e-4
Pre ↔ Post"	0,015	0,005	890	4,435	0,022
Pre ↔ Light 2	0,009	0,005	890	2,757	0,373
Pre ↔ Post 2	0,001	0,005	890	0,324	1
Light ↔ Post	-0,010	0,005	890	2,98	0,285
Light ↔ Post"	0,026	0,005	890	7,778	7,382 e-7
Light ↔ Light 2	0,021	0,005	890	6,100	2,578 e-4
Pre ↔ Post 2	0,012	0,005	890	3,667	0,100
Post ↔ Post"	0,037	0,005	890	10,756	3,769 e-9
Post ↔ Light 2	0,031	0,005	890	9,077	0
Post ↔ Post 2	0,023	0,005	890	6,644	4,461 e-5
Post" ↔ Light 2	-0,006	0,005	890	1,678	0,843
Post" ↔ Post 2	-0,014	0,005	890	4,111	0,043
Light 2 ↔ Post 2	-0,008	0,005	890	2,433	0,519

3.2 Electrophysiology

To further investigate the light-evoked effects of Ziapin2 on hiPSC-CMs behavior, the following experiments focused on the evaluation of the modulation of cell membrane properties during the light stimulus.

3.2.1 Membrane potential

hiPSC-CMs were incubated with Ziapin2/H_20 according to the protocol described at Paragraph 2.2.2. Light stimuli were then administered to cells to observe light-evoked membrane voltage modulation. Three different light stimuli periods were used: 20 ms, 200 ms, 10000 ms. The membrane voltage was monitored before the light stimulus administration, during, and after. Remarkably, for the patch-clamp assays, the light stimulus was in continuous mode instead of pulsed mode, as for the CR analysis.

Patch-clamp recordings show a biphasic modulation of the membrane potential characterized by an early hyperpolarization followed by a delayed depolarization of similar amplitude. Two representative traces are reported in Fig. 3.16. The hyperpolarization peak and depolarization peak were extracted from these traces.

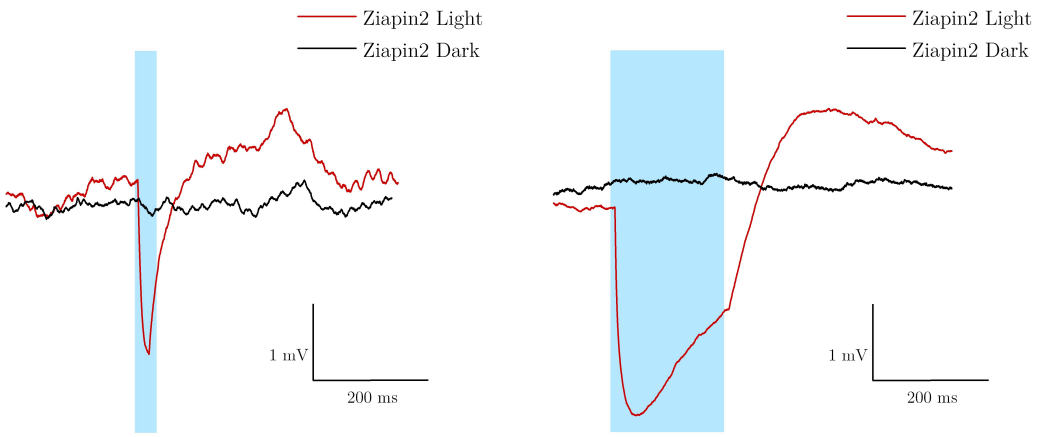

(a) **(b)**

Figura 3.16: Light-induced membrane potential variation of Ziapin2-loaded hiPSC-CMs. *Representative whole-cell current-clamp traces recorded from hiPSC-CMs loaded with Ziapin2/H_2O (5 μM) in dark (black) and upon illumination (red). Cyan shaded areas represent (a) the short (20 ms) and (b) the long (200 ms) visible light pulses. Every trace is obtained as an average of 20 consecutive sweeps.*

The observed V_m modulation is compared to a control condition. Mean ± s.e.m. for hyperpolarization and depolarization peaks in the different conditions are reported in Tab. 3.15 and visually represented in Fig. 3.17a. Statistical analysis returned a statistically significant difference between the mean V_m modulation in Ziapin2-loaded cells and non-treated cells for both hyperpolarization and depo-

Tabella 3.15: Light-induced biphasic modulation of membrane potential in Ziapin2-loaded hiPSC-CMs: hyperpolarization and depolarization peaks. *Mean ± s.e.m. for hyperpolarization (Hyp) and depolarization (Dep) peaks in hiPSC-CMs treated with Ziapin2 (Ziapin2) and not treated or water-treated (Ctrl). Data are reported in mV. Ziapin2: n = 16 (20ms); 17 (200ms); 24 (10000ms). Light Ctrl: n = 20 (20ms); 20 (200ms); 20 (10000ms).*

	Hyp		Dep	
	Ziapin2	**Light Ctrl**	**Ziapin2**	**Light Ctrl**
20 ms	-1,401 ± 0,148	-0,092 ± 0,066	0,943 ± 0,475	0,069 ± 0,049
200 ms	-1,545 ± 0,454	-0,083 ± 0,032	1,023 ± 0,709	0,049 ± 0,022
10000 ms	-1,604 ± 0,627	-0,032 ± 0,069	1,030 ± 0,727	0,012 ± 0,060

larization peaks and independently from the light stimulus duration (P<0.0001, Mann-Withney U test). The pairwise comparison is reported in Tab. 3.16.

Tabella 3.16: Light-induced biphasic modulation of membrane potential in Ziapin2-loaded hiPSC-CMs: statistical analysis. *Results of the Mann-Withney test. Ziapin2: n = 16 (20ms); 17 (200ms); 24 (10000ms). Light Ctrl: n = 20 (20ms); 20 (200ms); 20 (10000ms)*

	Pairs	Z	Asymp. Prob>|U|
20 ms Hyp	**Ziapin2 ↔ Light Ctrl**	-5,078	3,8 e-7
20 ms Dep	**Ziapin2 ↔ Light Ctrl**	4,855	1,2 e-6
20 ms Hyp	**Ziapin2 ↔ Light Ctrl**	-5,166	2,4 e-7
200 ms Dep	**Ziapin2 ↔ Light Ctrl**	5,013	5,3 e-7
1000 ms Hyp	**Ziapin2 ↔ Light Ctrl**	-5,639	1,7 e-8
1000 ms Dep	**Ziapin2 ↔ Light Ctrl**	5,026	5,0 e-7

W.r.t. peak latency, the hyperpolarization peaks occur within 50 *ms* from light onset. The box plots in Fig 3.17b show that the mean value is slightly larger with 200 *ms* light stimuli rather than 20 *ms* or 10000 *ms*. A similar trend is obtained for the depolarization peak, that occurs around 350 *ms* after the light onset. Of note, the statistical analysis returns a significant difference only between the time-to-hyperpolarization obtained with the short light pulse w.r.t. the two longer stimulation periods (P<0.00001, Mann-Withney U test. 20 *ms*: n = 16; 200 *ms*: n = 17; 10000 *ms*: n = 24).

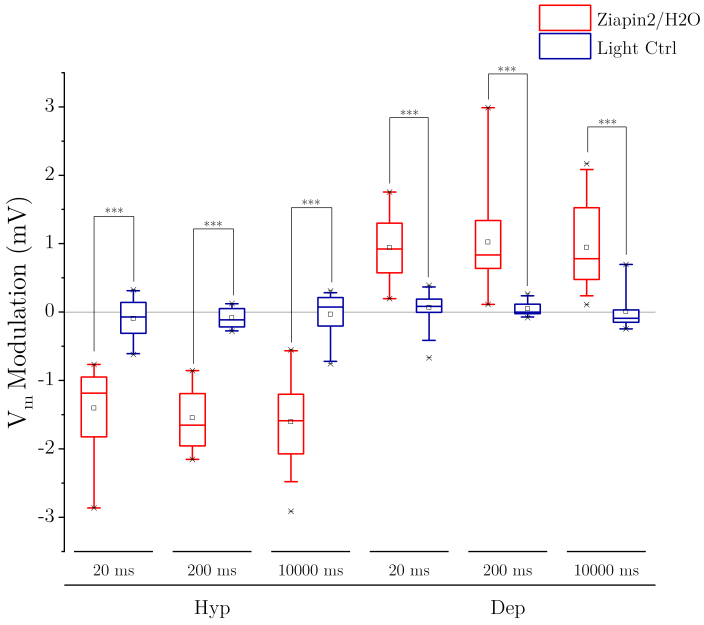

(a)

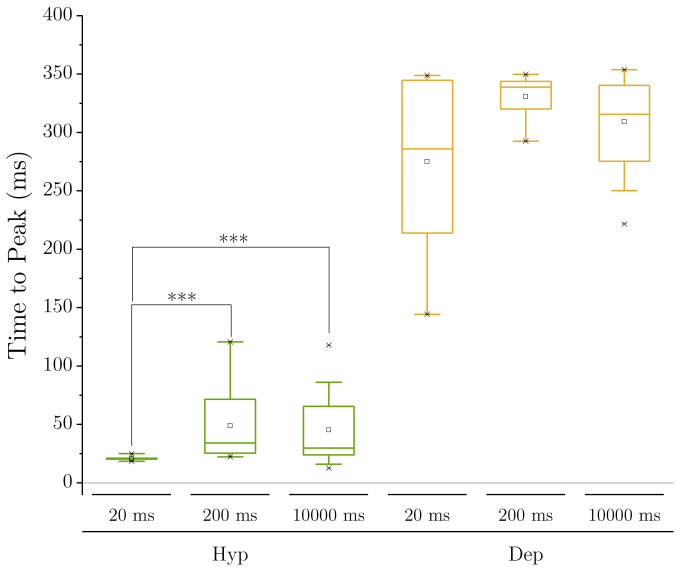

(b)

Figura 3.17: Light-induced biphasic modulation of membrane potential in Ziapin2-loaded hiPSC-CMs. *Box plots of the peaks hyperpolarization and peak depolarization changes in hiPSC-CMs exposed to Ziapin2/H_2O and subjected to 20/200/10000 ms light stimulation. Ctrl (dark-blue) indicates the values recorded for hiPSC-CMs exposed to the same protocol, in the absence of Ziapin2. (b) Time-to-peak hyperpolarization and depolarization as a function of the light stimulus duration. Ziapin2: n = 16 (20 ms); 17 (200 ms); 24 (10000 ms). Water-treated hiPSC-CMs or Light Ctrl: n = 20 (20 ms); 20 (200ms); 20 (10000 ms). Statistical tests: Mann-Withney U test. * P <0.05; ** P<0.005; *** P<0.0005.*

3.2.2 Firing activity

Since a depolarization peak above a certain threshold triggers the generation of an AP, the following analysis examined the capability of light stimulation to elicit AP in Ziapin2-loaded hiPSC-CMs acutely. To this end, the three different stimulation protocols were tested: 20 ms, 200 ms, 10000 ms. This time the light stimuli were administered to cells five times (i.e., five sweeps), and each time the firing activity was monitored for 10 s after the light onset. A representative AP of hiPSC-CMs is shown in Fig. 3.18.

For the 20ms and 200ms protocols, the analyzed cells were not spontaneously beating before administering the light stimulus. In both protocols, it is observed that more than half of cells generate one AP in at least one sweep (20ms: 77%, n=15; 200ms: 70%, n=15). The percentages of responding cells as function of the stimulation sweep are reported in Tab. 3.17. Overall, the percentage of responding cells does not decrease across the different stimulation cycles.
Tab. 3.17 indicates also the time between light onset and the AP upstroke (20 ms: 2,996 $\pm$ 0,653 s; 200 ms: 2,636 $\pm$ 0,597 s). No statistical difference was observed in time-to-AP values among the two light stimulus protocols (P $>$ 0.05, Mann-Withney U test).

The 10000 ms protocol, instead, was used to investigate the firing rate during the stimulation protocol (Fig. 3.19). This time, the firing activity of the cells was recorded in both spontaneously beating or not beating cells. The firing rate peaks during the light phase of the 10 s stimulus and slightly decreases after light offset (mean firing rate $\pm$ s.e.m. *Pre*: 0,044 $\pm$ 0,0154 Hz; *Light*: 0,188 $\pm$ 0,0203 Hz; *Post*: 2,30932 $\pm$ 0,0289 Hz). A statistically significant difference is identified with the Friedmann/Dunn's test ($\chi^2(2) = 21,568$, $P > \chi^2 = 2,073e-5$. $Prob_{Pre-Light} = 1,279e-5$ Friedman/Dunn's test). The results of the *post-hoc* test are reported in Tab. 3.18. The analysis returns a statistically significant difference between the mean firing rate in *Pre* and *Light* condition. A comparable

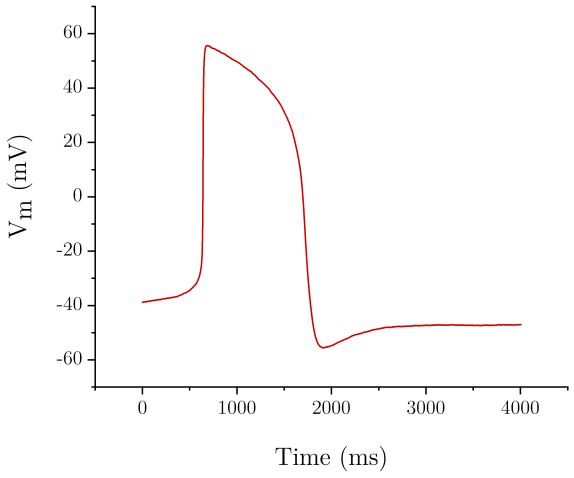

Figura 3.18: Action potential trace of optically stimulated Ziapin2-loaded hiPSC-CMs. *Representative AP trace recorded from hiPSC-CMs loaded with Ziapin2/H_2O (5 μM) upon illumination.*

Tabella 3.17: Light-induced firing activity modulation in Ziapin2-loaded hiPSC-CMs. *Percentage of responding cells independently on the sweep (% Responding) and as a function of the stimulation sweep. The latter being the number of cells that spike at that specific sweep number, no matter whether they have already fired in the previous sweep.*

	20 ms	**200 ms**
Total cells	15	15
Responding cells	10	9
% Responding	76.9 %	69.2 %
% Responding at sweep 1	40 %	55.5 %
% Responding at sweep 2	30 %	37.5 %
% Responding at sweep 3	60 %	62.5 %
% Responding at sweep 4	44.4 %	50 %
% Responding at sweep 5	20 %	62.5 %
Time to AP (mean ± s.e.m.)	2,996 ± 0,653 s	2,636 ± 0,597 s

trend is observed also in Ziapin2-loaded hiPSC-CMs, previously hyperpolarized (membrane potential V_m mean ± s.e.m. = -46,987 ± 5,727 mV, n=3) to abolish the spontaneous light-independent firing.
To verify whether the increment is larger when the cells are firing at a low rate or not firing at all, the variation of the firing rate as function of the resting spiking frequency has been plotted in Fig. 3.20. The bar plot suggests that the lower the initial firing rate of the cell, the higher the increment in spike frequency.

Tabella 3.18: Light-induced firing Rate in Ziapin2/DMSO-loaded hiPSC-CMs: statistical analysis. *Results of the pairwise comparison test or Dunn's test. Ziapin2, n = 22*

Pairs	**Sum Rank Diff**	**Z**	**Prob.**
Pre ↔ Light	-30,5	4,598	1,3 e-5
Pre ↔ Post	-19	2,864	0,0125
Light ↔ Post	11,5	1,734	0,249

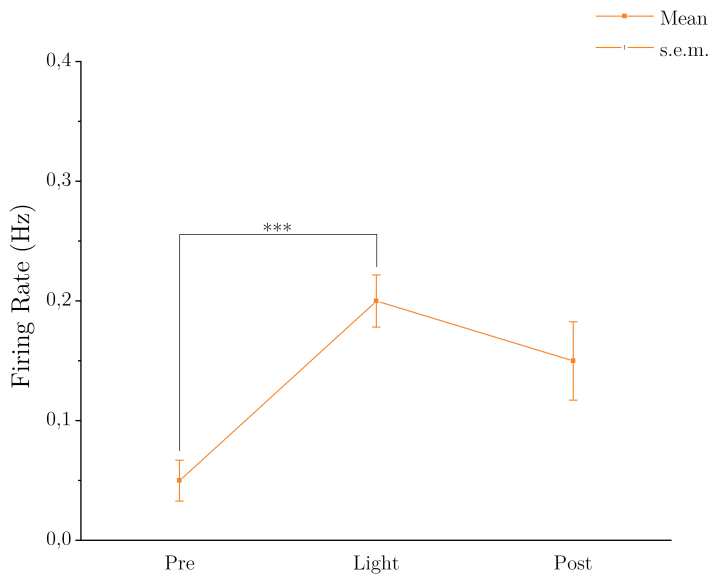

Figura 3.19: Light-induced firing rate trend in optically stimulated Ziapin2-loaded hiPSC-CMs. *The graph shows the AP frequency Pre, during (Light) and Post light stimulus. The firing rate is extracted only for the* 10000*ms condition. Statistical tests: Friedman/Dunn's test. * P <0.05; ** P<0.005; *** P<0.0005. Ziapin2-loaded hiPSC-CMs: n = 22*

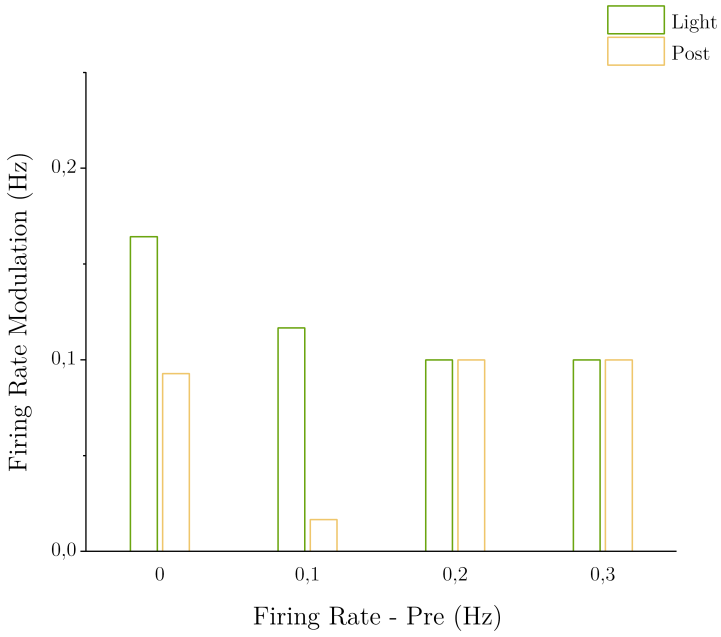

Figura 3.20: Light-induced firing activity modulation in Ziapin2-loaded hiPSC-CMs as function of resting condition. *The bar plot shows the increment in firing rate (ΔFR) as function of the resting firing rate. Light: ($FR_{Light} - FR_{Pre}$); Post: ($FR_{Post} - FR_{Pre}$). n = 8*

3.2.3 Membrane capacitance

The membrane capacitance of Ziapin2-loaded hiPSC-CMs was investigated in both dark and light conditions. The box plots of the capacitance values are reported in Fig. 3.21. As observed the capacitance remains almost constant upon illumination. To be more precise, a decrease of less than 0.5 % is measured between *Dark* and *Light* condition (mean decrease ± s.e.m.: 0,083 ± 0.011 pF).

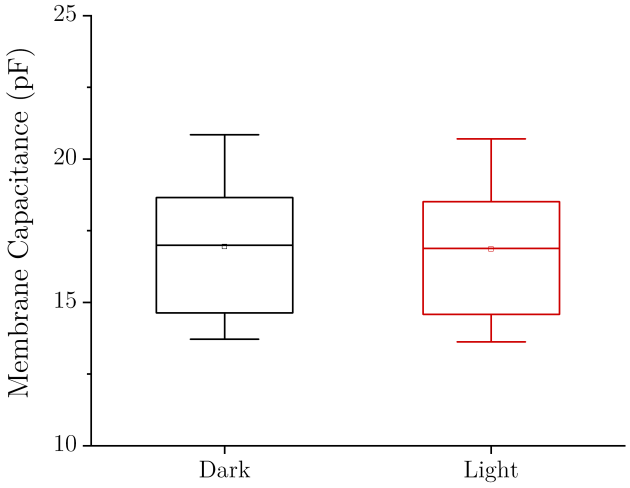

Figura 3.21: Light-induced membrane capacitance modulation by Ziapin2-loaded in hiPSC-CMs. *Box plots of the peak capacitance changes after the exposures of hiPSC-CMs to Ziapin2 (5 μM in H_2O) in dark (dark-blue) and light condition (light-blue). The same hiPSC-CMs were recorded when loaded with Ziapin2 and during light stimulus (470 nm; 50 mW/mm^2).*

3.3 Localization assay

Ziapin2 localization was investigated with a colocalization assay. Given the spontaneous photoluminescence of Ziapin2 no probe was used to mark it, while a specific probe was adopted to mark the ER. Few representative fluorescence images are reported in Fig. 3.22. The confocal images show that both fluorescence signals originate from a perinuclear zone with a partial overlap between the two. However, it can be noticed that the signal coming from the ER probe seems much more distributed over the cell body w.r.t. the highly-localized signal of Ziapin2. In Fig. 3.22f, for instance, the signal emitted by Ziapin2 clearly originates from a vesicle-like structure.

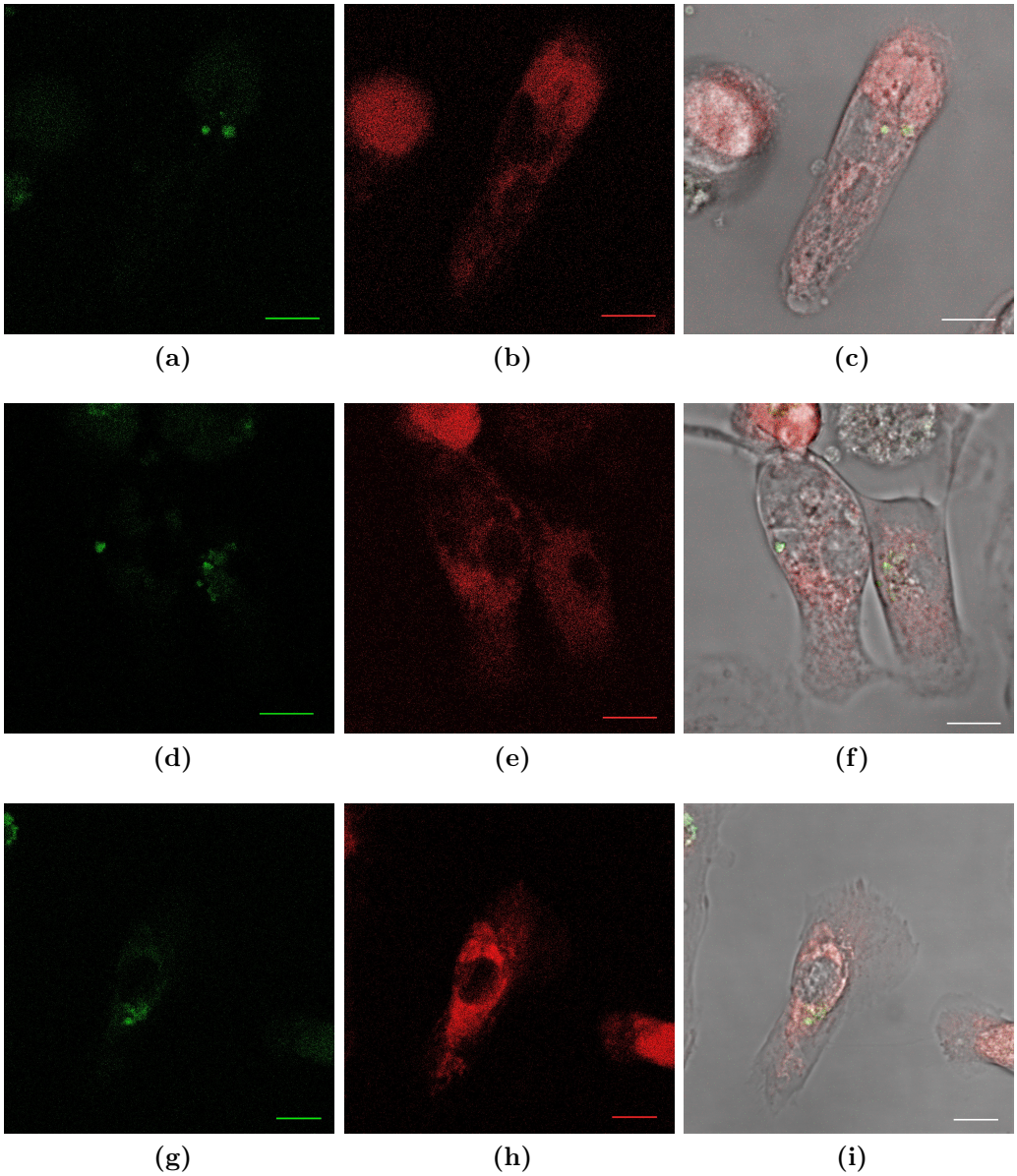

Figura 3.22: Colocalization Experiments in Ziapin2-loaded hiPSC-CMs. *Confocal 3D-z-stack representative images of Ziapin2 fluorescence (green) in hiPSC-CMs and its colocalization with endoplasmatic reticulum probe (red). Scale bar = 10 µm*

Capitolo 4

Discussion

The primary goal of this study was the characterization of the functional response of Ziapin2-loaded hiPSC-CMs to light. To this end, the cell contractility was studied to monitor the presence of a certain modulation in the CR upon illumination. Additionally, preliminary electrophysiological and localization assays were performed to speculate about the biological mechanism responsible for a functional response. Although the viability of Ziapin2-loaded cardiac cells was not evaluated during this study, the results obtained previously on primary hippocampal neurons and Hek293 confirmed the absence of any change in cell death induced by Ziapin2 treatment, both acutely or 7 days after the exposure [12]. Furthermore, the results obtained during the contractility analysis and the electrophysiological experiments provide sufficient evidence for Ziapin2-loaded hiPSC-CMs acute viability. Thus, it can be assumed that overall Ziapin2 does not provoke any adverse reaction also in hiPSC-CMs. However, further experiments should be performed to confirm this claim in the medium-long culture period.

4.1 Contractility Analysis

The first experimental phase of this thesis work aimed to investigate the response of optically stimulated Ziapin2-loaded hiPSC-CMs in terms of contraction behavior. Of note, this analysis was conducted on hiPSC-derived cardiac cells loaded with Ziapin2 using two different vectors, namely DMSO and water. Ziapin2/DMSO had already been used in primary hippocampal neurons [12] and Hek293 [18]. On the contrary, water-based Ziapin2 had been tested only in Hek293 and no study on excitable cells has been conducted yet. The choice of exploring this solvent was dictated by the potentialities offered by water w.r.t. DMSO (i.e., DMSO can cause toxicity effects at high concentration).

4.1.1 Single stimulation protocol

The first set of experiments used a single stimulation (i.e., one single illumination period) protocol to assess whether light stimulus could modulate the CR of Ziapin2-loaded hiPSC-CMs or not.

Ziapin2/DMSO

When Ziapin2/DMSO was used at $5\mu M$, a significant increase in the mean contraction frequency was observed during the light stimulus and shortly after the light offset (Fig. 3.2). The fact that this ascending trend continued even after the light was turned off suggests that the biological response triggered during light stimulus requires a certain amount of time to be compensated.
Interestingly, data showed a greater CR increment in those cells that were beating slowly or not beating at all before light onset.

Of note, the controls showed no evident increase of the CR during light stimulus, neither with light stimulus in the absence of the photoswitch nor in the presence of the photochromic molecule without visible light excitation. Though the trend was not comparable, the attentive reader could have noticed that the mean CR for the two control conditions was lower than the average value measured in optically stimulated Ziapin2-loaded hiPSC-CMs. This can be explained considering two principal aspects. The first one is the role of environment and temperature on the contraction process [10], [14]. Indeed, it cannot be ruled out that the room temperature was lower during the control experiments and that this environmental effect slowed the cell CR. A second important remark is that, although generated with the same differentiation protocol, hiPSC-CMs show a dramatic variability [171]. This means that each batch could have somehow different mean CR and that, thereby, only the variation w.r.t. the resting condition could be compared (Fig. 3.5).

Ziapin/H_2O

A slight increment in the mean CR upon illumination was also observed when hiPSC-derived CMs were loaded with Ziapin2/H_2O 5 μM. However, in this condition, the raise was much less prominent than DMSO and the trend showed an instantaneous decrease after the light offset, which was not present in Ziapin2/DMSO (Fig. 3.10). Another observation that is worth to be done is that the distribution of the CRs was less spread in Ziapin2/H_2O rather than Ziapin2/DMSO (i.e., the CR ranged from 0 to 0.4 Hz in Ziapin2/H_2O and from 0 to 0.8 Hz in Ziapin2/DMSO). Given that the experiments were performed during autumn, while Ziapin2/DMSO experiments was performed in summer, the more concentrated distribution of Ziapin2/H_2O could be associated with a lower room temperature during Ziapin2/H_2O study. Indeed, a lower temperature is known to reduce the CR [10], [14].

Importantly, no ascending trend was observed in the control conditions (i.e., Ziapin2 Ctrl: only molecules without stimulus; Light Ctrl: only stimulus without molecules). Instead, the Ziapin2 control condition, where cells were loaded with Ziapin2/$H2O$ but no light stimulus was applied, shows a descending trend over the three-minutes period. This is interesting since it might be that the modest increase, observed in mean CR when light stimulus was administered to Ziapin2-loaded cells, is the result of a two-events overlap: the first event that causes the CR decrease observed in the control, and the second associated with the photoisomerization of the molecular photoswitch that increases the CR. Further studies should be

performed to validate this preliminary hypothesis.
An alternative idea that had been proposed to justify the reduced effect observed in Ziapin2/H_2O is that the identified differences were due to the state of Ziapin2 within the two vehicles. Indeed, it is known from previous studies [18] that Ziapin2 tends to aggregate in water while no aggregates are observed in DMSO. This implies that, when Ziapin2 is diluted in H_2O, an important fraction of molecules is aggregated and likely not able to load the cells. The lower amount of functional molecules available in Ziapin2/H_2O could also explain the immediate decrease in the CR after light offset. If a lower fraction of molecules loads the cell, the biological response elicited by light might be less striking and thus it will deplete faster.

This hypothesis was supported by the results obtained with a higher concentration of Ziapin2/H_2O (25 μM). Indeed, in this case the CR trend resembled the results obtained with Ziapin2/DMSO, with a marked ascending trend of mean CR that proceeds even after light stimulus offset. Despite the increased modulation of the CR, the effects with Ziapin2/H_2O were still lower than Ziapin2/DMSO. In particular, the subintervals analysis suggests that after 30 s from light onset the CR began to decrease in Ziapin2/H_2O (25 μM), as shown in Fig. 3.10b. This result could hint that, also using 25 μM as loading condition, the available molecules are still fewer than in DMSO. Alternatively, a different mechanism between the two solvents could be considered. Of note, either with 5 μM or 25 μM, the results showed that the cells that distinctly responded to light stimulus were those that were beating very slowly before light stimulus stands out from the rest (Fig. 3.12).

4.1.2 Double stimulation protocol

The second part of the contractility analysis wanted to evaluate whether the light-induced effects, observed during the first round, were reproducible over time. For that purpose, a six-minutes *double stimulation* protocol was performed. This time, the same cells were enlightened with two consecutive light stimulus periods, divided by two minutes in brightfield.

Ziapin2/DMSO

In Ziapin2/DMSO-loaded hiPSC-CMs the CR during the second stimulation round showed an ascending trend similar to the first illumination cycle. In detail, the CR increased during the first light stimulus and maintain the obtained frequency shortly after the light offset. After two minutes without light stimulus, however, the contraction frequency was returned back to a lower contraction frequency approaching the initial resting rate. At this point, when a new pulsed blue light stimulus was administered, the CR raised up again, surpassing the frequency peak obtained during the first round (Fig. 3.13). This trend suggests that the light-induced effects are preserved even after the first light stimuli and that a functional response can be triggered multiple times. Additionally, the fact that the CR began to decrease after two minutes from the light offset hints that the triggered effects can be compensated and the CR can return to its initial condition.

Ziapin2/H_2O

The capability of Ziapin2 to elicit a biological response to multiple light stimuli was confirmed also when water was used as solvent for Ziapin2 loading. However, as already presented with the *single stimulation* protocol, the effects triggered in this condition were globally lower and less long-lasting than those seen for Ziapin2/DMSO. To be more precise, when Ziapin2/H_2O at 5 μM was used, the first light stimulus was seen to elicit a slight increase in the mean CR, followed by a sharp decrease upon light offset (Fig. 3.14). This implies that when the second light stimulus is applied, the cells are beating at a much lower rate w.r.t. the resting condition and, despite the increase evoked by the second light stimulus, the CR cannot reach the initial contraction frequency. Interestingly, the dramatic drop after light offset was observed also with the 25 μM condition (Fig. 3.15). Indeed, even if the increment of the mean CR was much more evident in 25 μM rather than 5 μM, the CR after the first light stimulus decreased sharply when the stimulus was removed. This marked drop in the mean CR was not observed with Ziapin2/DMSO. It might be that this prominent decrease is simply related to the fact that the CR began to decrease previously in Ziapin2/H_2O rather than in Ziapin2/DMSO, either when 5 μM or 25 μM were used. However, it would remain to be investigated why the effects last less in Ziapin2/H_2O rather than Ziapin2/DMSO. Further analyses remain to be done to understand whether this early decrease is due to a lower amount of loaded molecules or due to other factors, such as the different solvent used. Is this marked drop somehow related to the CR descending trend observed in the control condition where only Ziapin2/H_2O was used without light stimulus? Is this effect related to the environmental condition? Does this sharp fall occur also in Ziapin2/DMSO, if a longer time period between the first stimulus and the second one is permitted?

4.1.3 Open questions

The conducted contraction behavior analysis suggests that overall the light can induce an increase in the mean CR of Ziapin2-loaded hiPSC-CMs and that this effect can be elicited again when another light stimulus is applied. Despite these promising results, still several questions need to be addressed.

- Is there any difference between DMSO-based or water-based loading solutions? The fact that increasing the molecules concentration in Ziapin2/H_2O 25 μM restored the CR ascending trend strongly supports the idea that the biological response elicited by the two solvents is the same and that the observed variations are only related to a different amount of free molecules that could be easily internalized by the cells. However, some other differences might be present. For instance, one may wonder whether the dramatic drop of the CR observed in Ziapin2/H_2O upon light offset occur also in Ziapin2/DMSO or not. Or even, why does the control for Ziapin2/H_2O shows a descending trend that the control for Ziapin2/DMSO does not present? It might be that DMSO can enhances cell membrane permeability and pore formation [19] and that this property can alter the molecule internalization?

- Are the observed light-induced functional effects related to the Ziapin2 photoisomerization? So far, the absence of a significant response in the control conditions with Ziapin2-loaded hiPSC-CMs and no light stimulus constitutes a preliminary proof-of-concept of photoisomerization causality. However, to ultimately confirm that the observed functional response are due to Ziapin2 photoisomerization further experiments should be performed.
  Firstly, it should be excluded that the observed increase in the CR is not referable to a temperature increase [10]. In this regard, theoretical calculations have shown that the temperature increase given by Ziapin2 energy absorption is absolutely irrelevant, so it seems unlikely that the observed biological response is associated with a heating effect. Secondly, it might be preferable to rule out that the biological response is triggered by a photocatalytic effect initiated by some molecule aggregates rather than Ziapin2 photoisomerization. To verify or deny the truthfulness of this speculative hypothesis, the experiments could be repeated using a light stimulus at different wavelengths. If the amplitude of the biological response peaks at 470 nm, it means that the photoisomerization is actually triggering the CR increase. Alternatively, if the effects are stronger for higher wavelengths, it would be reasonable to assume that Ziapin2 aggregates are actually absorbing the light (i.e., absorbance peak for aggregates 500 nm) and triggering the response.
  Lastly, the occurrence of Ziapin2 photoisomerization reaction could be explored by measuring the time-dependent quenching of *trans* isomer PL upon illumination at 470 nm [18].

- Why do some cells respond distinctly to light stimulus and others do not or even show the opposite behavior? It might be speculated that this is due to the lack of control during the internalization process. This implies that not all cells are surely loaded with the photochromic molecules and that, therefore, if no effects are observed in the contraction behavior of one cell, it might be that this cell has not internalized the molecules and not that the molecule is not triggering a functional response.

- Why, independently from which vector or concentration was used, the cells that respond more distinctly to light were those that were not beating or beating slowly in the resting condition? It could be speculated that this is simply related to the presence of a physiological upper bond in CR of hiPSC-derived cardiac cells due to the low room temperature [10], [14] and to the immaturity of this cellular model [172], [173] that cause the Ca^{2+} transients rise and decline at a substantially slower rate. Thus, when a cell has a higher resting CR, there is less margin for increment; while when it contracts at a lower frequency before light stimulus there is much room for the CR to increase. However, this explanation could not justify why, even in Ziapin2/DMSO where the CR ranged from 0 to 0.8 Hz, the cells that presented an initial CR proximal to 0 Hz were still those that react more. Does it means that those cells that are not beating at rest or beating slowly are those that have internalized the molecules? Is there a relationship between internalization and the low resting CR?

- Could the CR be modulated at a precise frequency? At the moment, despite the increase in the CR during light stimulus, the mean CR during light stimulus (about 0.3 Hz) did not reach the frequency of the pulsed light (1 Hz). However, these results cannot completely rule out the possibility. It might be that the physiological upper bond in CR, hypothesized above, could have also prevented the modulation of the CR with the forcing periodic light stimulus. Further experiments, in controlled temperature or with a lower forcing frequency of light pulses, should be performed in order to ultimately assess this capability.

4.2 Electrophysiology

Parallel to the characterization of the effects elicited by Ziapin2 on the contraction behavior, the electrophysiological properties of optically stimulated Ziapin2-loaded hiPSC-CMs were investigated with patch-clamp techniques. In this case, only the water vector was used, given that it is a more cell-friendly solvent w.r.t. DMSO.

4.2.1 Membrane potential

Whole-cell recordings were carried out in current-clamp mode (I = 0) in response to short (20 ms) and long (200 ms, 10000 ms) pulses of light. The experiments demonstrated the reversible modulation of the membrane potential of Ziapin2-loaded hiPSC-CMs via illumination with visible light (470 nm, 50 mW/mm^2). Indeed, photostimulation of hiPSC-derived cardiac cells, with either short or long light stimuli, generated a significant hyperpolarization of the V_m that occurred immediately at the light onset. After that, the membrane potential showed a modest, but statistically significant, rebound depolarization (Fig. 3.17a). Finally, the membrane potential returned slowly to resting values. Interestingly, the observed biphasic modulation of the membrane potential resembles the light-elicited voltage modulation observed in neurons and Hek293 cells [12], [18]. However, especially in neurons, the V_m modulation was much larger than in hiPSC-CMs. This amplitude difference could be related to the use of Ziapin2/H_2O in hiPSC-CMs and of Ziapin2/DMSO in the other cell lines. Indeed, as aforementioned, Ziapin2 tends to aggregate in water, which implies that only a lower fraction of the molecules in the loading solution can isomerize and trigger a biological response. On the other hand, it cannot be excluded that the differences in the membrane potential modulation between hiPSC-CMs and neurons or Hek293 are linked to a different biological process involved. This last consideration is supported by the results collected from the capacitance measurements and the preliminary localization assay (see Paragraph 3.3).

W.r.t. the time-to-peaks values, the statistical analysis returned a significant difference between short and long stimuli only for the hyperpolarization phase (Fig. 3.17b), while the depolarization delays ranked equally among the three conditions. Indeed, independently from the hyperpolarization delays, the rebound effect raised almost 350 ms after the light onset, either with short or long light stimuli. Note that also with 10000 ms light stimulus duration, the biphasic modulation of membrane potential occurred before light was switched off.From previous studies, it is known that, in DMSO and sodium dodecyl sulphate (SDS)[1], a *cis*-rich photo-stationary state is reached within 200 ms (τ = 60 ms) [18]. Thus, if Ziapin2 isomerization would be the cause of the observed effects, it could be speculated that a short light stimulus (20 ms) triggers the photoisomerization only of a fraction of molecules, while both 200 ms and 10000 ms enable the achievement of the photo-stationary state. This observation provides the basis for few considerations. First, the presence of a functional effect with comparable delays also with a short light stimulus (20 ms)

[1]Sodium dodecyl sulphate is commonly used to mimic bilayer environment

suggests that there is no need that all molecules are photoisomerized to trigger the biological response. Second, the amplitude and the delays of the response is not proportional to the number of molecules isomerized, and thus, to the stimulus duration. Third, once the photo-stationary state is reached, even if the light stimulus continues, no other ensemble response can be elicited. This last remark might be explained considering that at the photo-stationary state a dynamic equilibrium is reached where the amount of molecules which isomerize from *trans* to *cis* is almost equal to the amount of those that isomerize from *cis* to *trans*. The conformational switches of these few molecules are probably insufficient to trigger the biological response. Interestingly, during the contraction experiments the light stimulus duration lasted for a minute and the light-evoked functional effect was visible over all the stimulation period. How is that possible? It might be that the pulsed blue light (500 ms stimulus, 500 ms no stimulus) used in contraction behavior analysis allows a fraction of molecules to return to the *trans* conformation during the 500 ms of no stimulus. This way, a *trans*-rich state is reached again before a new light pulse is administered.

4.2.2 Firing activity

The ability of light stimulation to elicit APs in Ziapin2-loaded hiPSC-CMs was also evaluated. Short and long light stimuli (20, 200 ms) were administered five times to not-beating cells in order to monitor whether the photoswitch isomerization could trigger the generation of at least one AP. About 70% of the cells respond to the stimulus in at least one of the five sweeps, with more than half of cells that respond to the first stimulation cycle (Tab. 3.17). Noticeably, this all-or-nothing variation of the membrane potential was significantly delayed w.r.t. the rebound depolarization peak (350 ms) from light onset. This means that the APs are not generated directly by the initial electrotonic potential. Instead, it seems likely that the elicited spike is caused by another cellular process that occurs in between the two.

A light stimulus of 10000 ms was also used to assess the increase in the firing rate of both spontaneously beating and not-beating cells. The obtained results suggest that light-evoked isomerization of Ziapin2 could increase significantly the firing rate (Fig. 3.19). Moreover, in accordance with the outcomes concerning contraction behavior, those cells that had no AP activity or that had a low firing rate showed a more marked increase in firing frequency, as reported in the histogram of Fig. 3.20. The considerations mentioned above about the possible presence of a physiological upper bond in the CR of hiPSC-CMs at room temperature are easily transferable to the firing frequency, given the well-known *excitation-contraction coupling* that characterizes cardiac cells. One could also speculate also in this case that there is a linkage between molecules loading, low resting firing rate (which implies also low resting CR), and the presence of a distinct response. The whole-cell recordings on cells that were not firing at rest enabled to extract also an estimate of the time delay between light onset and the generation of the first AP. Once again, similar to what was observed for the hyperpolarization peaks, the time required to elicit the first AP in previously-not-beating cells was almost identical in the three light stimulus conditions (no statistically significant difference). This implies that

20 ms of light stimulus are sufficient to elicit the biological response and that, using a longer light stimulus, the triggered response is not significantly different neither in terms of amplitude nor in velocity.

4.2.3 Membrane capacitance

In neurons and Hek293 a V_m biphasic modulation similar to the one detected in hiPSC-CMs was associated with a capacitive current elicited by Ziapin2 photoisomerization [12], [18]. For that reason, the membrane capacitance of hiPSC-CMs was also monitored upon illumination. Surprisingly, the membrane capacitance drop observed in primary hippocampal neurons was more than six times the minimal decrease observed in hiPSC-CMs capacitance [12]. To be more precise, when light stimuli were administered to Ziapin2-loaded hiPSC-CMs, the capacitance values decreased w.r.t. the dark condition of about 0.5%. This result suggests that it is highly unlikely that the detected light-induced functional effects could be linked to a membrane capacitance change, as observed in other cellular models. This argument is further supported by the results obtained from the localization assay (see Paragraph 3.3). Indeed, Ziapin2, rather than dwelling the cellular membrane as observed in neurons, localizes intracellularly in hiPSC-CMs. This discovery makes it even more improbable that Ziapin2 photoisomerization could affect the membrane thickness, causing a capacitance drop upon illumination, as done in primary hippocampal neurons. On the contrary, it is reasonable to posit that another cellular process is involved.

4.3 Localization assay

It is generally accepted that the location of a molecule is closely related to its physiological function. According to this premise, the local information of Ziapin2 was considered to be crucial if only to speculate about the biological mechanism responsible for the observed functional response to enlightenment. To this end, fluorescence microscopy was used, being the gold standard approach in cell biology for the localization of biomolecules residing on cellular structures[2].

As mentioned in the previous Paragraph, surprisingly, the fluorescence images suggested that Ziapin2 did not localize at the cellular membrane, differently from what was observed with primary hippocampal neurons and Hek293 [12], [18]. From previous molecular dynamics simulations, it was assumed that Ziapin2 in *trans* conformation would have entered the lipid bilayer and arranged itself to an equilibrium position with the positively charged pyridine rings at the level of the lipid heads [12]. Additionally, according to the free-energy profile presented in [12], a 0.52 eV energetic barrier for membrane desorption to water was expected to prevent the localization of the photoswitches intracellularly. Conversely from the expectations, fluorescence images showed the presence of Ziapin2 perinuclearly. Four speculations have been proposed to explain this unforeseeable result.

The first argument is that the cellular membrane of hiPSC-CMs might be different from other cell lines in terms of composition. This might be due to the partial immaturity of hiPSC-CMs, that could influence membrane composition and, as a consequence, membrane permeability. However, little is known about the cell membrane composition of hiPSCs and hiPSC-CMs [179] and, therefore, no definitive conclusion can be drawn at present.

It could be also that the use of DMSO as the vehicle for the molecule enhances cell membrane permeability and pore formation [19], favoring the entering of the molecular photoswitch within the cell. However, if DMSO was the cause of the intracellular localization of Ziapin2, it would remain to be clarified why this DMSO-mediated internalization process was not observed in neurons, given that the same solvent was used in [12].

A third idea is that Ziapin2 could be attracted by the lipid bilayer of an intracellular structure and that the presence of this structure might change the free-energy profile, favoring molecule desorption from the membrane. For instance, it could be that hiPSC-CMs possess an intracellular organelle with high affinity for Ziapin2, which is absent in other cellular models or that is closer to the membrane (e.g. SR endomembrane is present only in muscle cells and it is located close to the cell membrane [180]). In this case, the speculation could potentially explain the desorption from the cellular membrane, but then it will remain to be investigated why the molecule is found perinuclearly and not submembraneously. Does this intracellular organelle expand from the cellular membrane to the nucleus? Does the molecule migrate once dwelling into the endomembrane?

The last speculative hypothesis considers that a transport system, specific of hiPSC-CMs and absent in the other investigated cellular models, supports Ziapin2

[2]Fluorescence microscopy makes use of well-characterized markers to assess the position of the target molecules and its colocalization with other organelles or intracellular subunits.

endocytosis. Interesting candidates for this process are caveolae [181], [182]. Caveolae are usually seen as bulb-shape invaginations of the plasma membrane or in complex structures harboring multiple caveolae that can form rosette-like structures [183], [184]. However, several studies clearly show the ability of caveolae to enter the cell by endocytosis. This was demonstrated by the translocation of caveolinis, specific proteins of this unique plasma membrane domain, from the plasma membrane to internal compartments. Caveolae endocytosis has been observed upon SV40 viral infection [185], lipid modification [186], hyperosmotic and heat shock [187], mitosis [188] and cell detachment [189]. For instance, when membrane cholesterol is oxidized, caveolins were seen to be redistributed to the ER and then to the Golgi complex [190], [191]. This means that there could be a signaling factor that favors the migration of the molecules to the perinuclear region once internalized by the means of caveolae endocytosis. What is very exciting of this speculation is that caveolae resemble lipid rafts in terms of composition, both being enriched in cholesterol and certain sphingolipids w.r.t. the surrounding membrane. Given that Ziapin2 was found to colocalize mostly with lipid rafts in primary hippocampal neurons [12], this might provide an explanation to the different localization observed for the two cellular models. It could be that Ziapin2 enters the cellular membrane and stabilizes at caveolae domains, instead of lipid rafts, and that, upon a certain trigger, the caveolae are endocytosed. One may wonder why do this Ziapin2 translocation was not visible in neurons or in Hek293? A possible answer is that caveolae are not uniformly distributed in different mammalian cell types and, eventually, they are highly abundant in mechanically stressed cells (i.e., muscle cells, fibroblasts, endothelial cells, adipocytes [184] and differentiated cells [192]), while virtually absent in neurons and lymphocytes [193]. Further analyses are required to assess the validity of this assumption.

Independently from how Ziapin2 can permeate the membrane, another question remains unsolved: where does it localize? The colocalization assays, performed using an ER probe, showed that the fluorescence signal from Ziapin2 originated from perinuclear regions and that it partially overlapped with an ER marker (Fig. 3.22). It was observed that, while the signal from the ER probe was found to be distributed almost everywhere in the cytosol, the fluorescence signal coming from Ziapin2 was densely concentrated at certain regions close to the nucleus (Fig. 3.22f). Additionally, sometimes the Ziapin2 was seen to be localized in sphere-like structures clearly independent from the ER (Fig. 3.22f).
W.r.t. these micelle-like structures, it could be speculated that these clusters represent micron-sized molecular aggregates. This assumption is supported by previous study where Ziapin2 was seen to aggregate in water, as a result of the amphiphilic nature of the molecule that tends to protect its hydrophobic parts from the water-based environment [18]. Remarkably, the size of these aggregates was seen to be around 1 μm, which is comparable with the dimension of the spherical vesicles observed in the fluorescence images. Additionally, the fact that these aggregates hinder the molecular isomerization and thus favor the radiative decay could explain the high fluorescence signals emitted and it might justify why the fluorescence of the other molecules is underestimated. Further studies must be performed to verify whether this speculation is true and, if it was, clarify the mechanism that brings to the formation of these micelles: do the molecules enter the cellular membrane

already as aggregates? do the clusters generate when the molecules are released by a transport system in the cytosol?
Despite these open questions, something can be said. Admitting that the fluorescent signal emitted by these micron-sized vesicles is related to molecular aggregates, the molecules localized within these micelles will be not able to photoisomerize, as demonstrated by Paternò and coworkers [18]. As a consequence, this fraction of molecules will probably not be responsible for the light-induced effects observed, unless a photocatalytic effect initiated by these molecular aggregates is present. If the effects are due to molecule photoisomerization, there should be another fraction of molecules that is not placed in a water-like environment. In that regard, the aforementioned study has shown that if Ziapin2 dwells in a lipid bilayer, its photoisomerization capability is restored, together with its opto-mechanical effect [18]. Thus, it could be speculated that a fraction of molecules is localized in an intracellular endomembrane and that this free-to-isomerize amount is responsible for the observed light-induced functional effects.
The fact that Ziapin2 fluorescent signal was found to colocalize with the ER probe suggests that the ER endomembrane might be the targeted intracellular bilayer. Notwithstanding this, the ER probe is known to prevent the proper distinction between ER and SR in hiPSC-CMs and therefore both endomembranes are likely. In that regard, it should be recalled here that the difference between ER and SR in cardiac cells is still a matter of debate [180]. The most accepted theory is that the SR and ER form two continuous, but largely distinct membrane systems [194] with different functions. This means that ER plays a role mainly in protein synthesis, modification, secretion, lipid, and steroid synthesis, and partial modulation of Ca^{2+} signaling, while SR is principally responsible for the regulation of Ca^{2+} transport and the control the *excitation–contraction coupling*. Whether the two endomembranes are separated or not, immunolocalization analysis carried out by Pozzan's group on compartmentalization of Ca^{2+} stores demonstrated that the SR-based Ca^{2+} stores are present throughout, but concentrated subsarcolemmally, while ER-based Ca^{2+} stores are concentrated in perinuclearly [195]. This latter observation, together with the presence of a predominant Ziapin2 fluorescent signal in the perinuclear regions, support the hypothesis that Ziapin2 actually colocalizes with the ER membrane compartment.
Even more, the Ziapin2 fluorescence was found to be concentrated in certain regions of the perinuclear space. This means that one could speculate that, though localizing at the ER membrane, the photochromic molecules are more affine to a specific receptor placed on it. Inositol (1,4,5)-trisphosphate receptor (IP_3R) is a promising candidate in these terms. IP_3Rs are cation channels, localized both in the cytoplasm and perinuclearly [180], [196]. Their main responsibility is to mediate Ca^{2+} release from intracellular stores, together with ryanodine receptors, RyRs [197]. For that reason, IP_3Rs are generally described as intracellular Ca^{2+} channels expressed on the ER Ca^{2+} stores [198].They are present both in adult ventricular muscle and in differentiating cardiomyocytes [199]. However, in adult CMs their Ca^{2+} release seems to contribute only marginally to the excitation-induced Ca^{2+} transient, while they seem to play a key role for pacemaker activity in differentiating cardiomyocytes [199]. Indeed, experimental results have provided evidence that the pacemaker mechanism in early embryonic stem cell-derived cardiomyocytes depends on IP_3R-

mediated Ca^{2+} release that is translated into a depolarization of V_m and subsequent activation of voltage-dependent Ca^{2+} channels, causing a significant Ca^{2+} influx ($I_{Ca,L}$) [199]. This might explain the curious correlation between low spontaneous contractility and marked light-induced response observed during the contraction behavior analysis. Additionally, these receptors open following a conformation change initiated by IP_3 binding to the IP_3-binding core [197]. This means that the opto-mechanical effect given by Ziapin2 photoisomerization might be able to equally trigger their activation. In summary, the idea presented here is that Ziapin2 permeates the membrane and localizes in close proximity to the IP_3 receptors on the ER membrane. Then, when optically-stimulated, the photoisomerization of Ziapin2 causes a conformational change in the receptors. Once the channels have been opened, they enable the release of Ca^{2+} in the cytoplasm. This event elicits a certain variation of membrane potential, succeeded by a stronger Ca^{2+} influx ($I_{Ca,L}$) and an AP upstroke. Of note, this speculative hypothesis cannot completely explain the results obtained from the elctrophysiological assay. Thus, several other experiments need to be performed to validate this assumption or identify an alternative biological mechanism.

Conclusions

Main findings

Electrical stimulation is the standard technique for exploring the electrical behavior of heart muscle, but this approach has considerable technical limitations. This thesis work provides evidence for the potential use of molecular photoswitches for optical stimulation of myocardium. The long term goal of this project is to identify new painless and versatile techniques for restoring healthy heartbeats in patients who are requiring implantable devices. In the short-term, the work was finalized to evaluate the functional response elicited by an amphiphilic visible light actuator, Ziapin2, in optically stimulated cardiac cells. To this end, hiPSC-derived CMs were used as cellular model for cardiac cells.

The collected data suggest that optically stimulated Ziapin2-loaded hiPSC-CMs increase their CR upon illumination and that this effect is reversible and repeatable. This functional response was demonstrated either using DMSO or water as solvent for the loading solution. Interestingly, the effects were seen to be much more striking in previously-not-beating cells or in those cells that were beating slowly before light onset. The raise of the CR has been associated with a rapid biphasic modulation of the membrane potential, followed by a delayed generation of an AP. In that regard, patch-clamp experiments have shown that pulses of visible light in Ziapin2-loaded hiPSC-CMs induce a transient membrane potential hyperpolarization, succeeded by a rebound depolarization. Remarkably, the AP firing is delayed w.r.t. this biphasic modulation and, thus, it is probably not directly triggered by the rebound depolarization. Of note, the fact that the light-induced effects observed in V_m resembled that of primary hippocampal neurons and Hek293 [12], [18], had led to believe that the biological mechanism involved could be the same: the *trans*-to-*cis* photoisomerization of Ziapin2 causes a membrane thickening, which in turn triggers a capacitive current. However, the membrane capacitance of hiPSC-CMs did not show any marked change between dark and light conditions (less than 0.5% difference). Thus, it seems likely that the observed functional response is triggered by a mechanism different from the membrane capacitance variation observed in neurons [12]. Co-localization assays provided further confirmation of that. Fluorescence images showed that Ziapin2 did not partition in the plasma membrane, as observed in neurons and Hek293. Instead, it localized intracellularly, probably on ER membrane or in vesicle-like structures proximal to ER. These results confirmed that a different biological pathway must be involved. Further analyses are required to fully understand the mechanism.

In summary, this thesis work demonstrated the reversible modulation of Ziapin2-

loaded hiPSC-CMs CR and membrane potential via illumination with visible light. The involved biological mechanism is still unclear, but it seems likely that it differs from the one previously observed in neurons and Hek293.

Future perspectives

The collected data represents a new proof-of-concept for the use of molecular photoswitch in cardiac cell opto-stimulation. Despite the promising results, several other detailed experiments are needed before the feasibility of optical stimulation of myocardium could be fully confirmed.

Follow-up activities

The next steps will be mainly focused on the comprehension of the mechanism involved that triggers the biological response. To this end, calcium imaging assays will be performed, eventually during video recording through optical microscopy for the simultaneous contraction behavior evaluation. In addition to it, caveolins immunostaining could be performed to verify the hypothesis that Ziapin2 enters the cell through caveolae endocytosis.
Once identified the biological pathway, other measurements could be planned to better characterize the functional behavior both acutely and after few days. In particular, cell contractility should be evaluated in controlled temperature to assess whether pulsed light is able to control the cell CR at a specific frequency. Likewise, it would be necessary to demonstrate that all the enlightened cardiac cells can be excited and contract in phase. This proof would be crucial to consider optical stimulation as an alternative to electrical stimulation for cardiac arrhythmia treatment. For this purpose, optical stimulation of cardiac patch, or laboratory-grown heart tissue, might be considered.

Long-term improvements

Parallel to the characterization of the effects elicited by Ziapin2 in hiPSC-CMs, other more general improvements should be done to optimize the design of light actuators and the equipment required to translate this technique towards the clinical application.
To this end, three principal lines of action have been identified:

- Improved variants of molecular photoswitches with better photosensitivity, long-term stability, and red-shifted absorption spectrum with better tissue penetration would be important to apply optical stimulation of photochromic molecules into animals or humans.
- Optical devices for *in situ* light delivery must be optimized and integrated with wireless power supply and communication units.
- Alternative strategies might be considered to trigger molecular photoswitches isomerization. In this context, ultrasounds represent a promising technology.

One way in which ultrasounds could be combined with molecular photoswitches is by the means of chemiluminescence [200]. The basic principle of this approach is to use ultrasounds to initiate a specific chemical reaction that causes the emission of light at a specific wavelength; and, then, exploit this luminescence to trigger the photoisomerization of the molecular photoswitch. Another hypothesis is the use of ultrasounds to directly trigger the mechano-isomerization of azobenzene-based photochromic molecules [201], [202]. Both approaches would avoid the lateral equipment (e.g. optic fiber) currently required to induce the photoisomerization of photo-sensitive molecules *in situ*, reducing the invasiveness of this technology.

Although the expansion of molecular photoswitches to the cardiac field by our group and others is in very early stages and there is still much room for improvements, this technique has already demonstrated undeniable advantages w.r.t. both conventional electrotherapy and other optical stimulation approaches. Thus, it is worth the effort to further explore this emerging field of research.
Let's *shine a light* on the heart.

Appendix
Optical microscopy for cardiac cells functional characterization

In current practice, the functionality of a CM is primarily measured by analyzing its electrophysiological properties. However, patch-clamp assays, which are the standard reference for high-precision electrical measurements of cells, have an extremely low yield and require the manual operation of a trained electrophysiologist. Likewise, novel high-throughput *in vitro* assays developed to monitor the electrical behavior of cells (e.g., microelectrode arrays or MEAs) have specific design constraints that make their use not straightforward.
On the contrary, the contraction behavior of CMs might be valid alternative aspects of cell physiology, that can be easily monitored with standard optical microscopy. Indeed, video microscopy allows the extraction of several parameters about cell mechanical behavior with a pretty simple experimental assay. This technique is not intended to replace electrophysiology experiments, but rather to support them with a rapid, simple, and cost-effective screening (i.e., it requires only an optical microscope and a camera, which are usually already present in a laboratory).

According to this idea, the first experimental phase of this thesis work exploited optical microscopy to collect functional information about Ziapin2-loaded hiPSC-CMs. To this end, a custom-made software was developed in Matlab for contraction rate estimation from video microscopy, as aforementioned in Paragraph 2.3.1. In this chapter, a brief overview of other methods used in computation biology to assess this problem is presented, together with a more detailed description of the approach used in this project.

Overview of the commonly used methods

Several bright-field based characterization techniques have been proposed over the last decades. These video analysis techniques incorporate various algorithms based on: light intensity changes [203], fast Fourier transform [204], moving texture [205], correlation coefficient w.r.t. a reference frame [206] or motion vectors [207]–[211]. Besides the high number of approaches and the variety of advantages and disadvantages, the motion vectors fields-based algorithms remain the standard procedure for generating beating signals from video recordings of cells.

The basic idea of motion vectors fields based algorithms is the estimation of motion or *displacement* fields from sequences of ordered images (i.e., a video).

To briefly explain it, consider an image sequence and represent it as a function of three variables $I(m, n, t)$, where the space variables m and n as well as the time variable t are discrete and bounded. As an object moves within the scene, the patterns of frames intensities change in a complex way. However, thanks to the *brightness constancy constraint*, a later image taken at time $t + \tau$ can be obtained by moving every point of the frame taken at time t according to a suitable motion field. This amount of motion is in general a function of m, n, t, and τ.
Although there exist several methods for computing the *displacement*, the most commonly used approach in video-based analysis of cardiac cells contractility is the *block-matching algorithm.*

Block-matching algorithm

Block-matching algorithms divide each video frame into analysis regions and compute a degree of similarity, or difference, between these regions in subsequent, or later, video frames. This process allows the calculation of velocity vectors, that provide information about the speed and direction of the motion of each analyzed region. Beating signals are then calculated combining the vector magnitudes for each frame. The basic assumption on which the combination of motion vectors provides information about cell beating behavior is that when a cell contracts, the cellular body is retracted towards the center or a focal point. Likewise, when the cell relaxes, the cellular body goes back to its resting state, causing again a certain movements that can be recorded and computed.

The steps of the process are represented in figure and they can be summarised as follow:

1. Divide a frame at time t into analysis region of a specific size (e.g. square blocks of size $N \times N$)
2. Consider a block of pixels centered at coordinates (m, n)
3. Match it to the corresponding block at the same coordinates (m, n) in the previous $t - \tau$ (or subsequent $t + \tau$) frame
4. Consider a search window of a specific size (e.g. $(N + 2w) \times (N + 2w)$) surrounding the center point (m, n)
5. Move the block of a certain amount $d = (i, j)$ to scan all the search window (*exhaustive step search*)
6. Each time, estimate a certain measure of similarity (or dissimilarity) between the block in the frame at time t and the other
7. Choose the displacement vector $d = (i, j)$ that provides the maximum similarity between the two blocks or the minimum dissimilarity

Note that software parameters, such as N and w are tuned manually for each video according to the specific experimental conditions.

The performed literature review has enabled to identify several video-based algorithms that use block-matching principles to extract the beating signal. Major

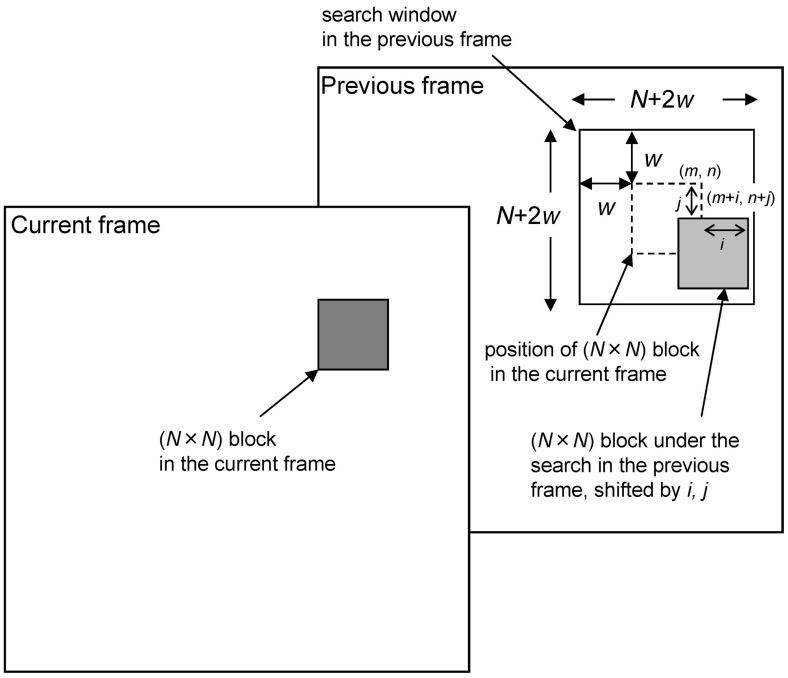

Block-matching algorithm. *The schematics of sequential frames in a search window. Each frame is divided into analysis regions (square blocks of NxN pixels). Then, the current block of pixels is matched to the corresponding block at the same coordinates in the previous (or subsequent) frame within a search window (square window $(N+2w)\times(N+2w)$). The value of w is chosen according to the expected movement, the smaller the displacement, the smaller the needed search window. The best match according to a matching criterion yields the displacement. Reproduce from [208]*

differences among them can be observed in: required camera frame rates, region selection modality that can be both user-assisted or automatic, and matching criteria used to assess the *displacement* field. Concerning the latter one, the most recognized similarity-dissimilarity or correlation measure currently used in block-matching are Mean Square Error (MSE), Mean Absolute Difference (MAD) [211], Minimum Quadratic Difference (MQD) [210], and the variance-normalized cross-correlation function (C) [207].

Consider a $N\times N$ block centered at (m,n) in the current frame and a $N\times N$ block centered at $(m+i,n+j)$ in the subsequent frame at $t+\tau$, the aforementioned criteria can be computed as follow:

$$MSE^{mn}(i,j)=\frac{1}{N^2}\sum_{r=-N/2}^{+N/2}\sum_{s=-N/2}^{+N/2}\left[I_t^{mn}(r,s)-I_{t+\tau}^{mn}(i+r,j+s)\right]^2 \tag{4.1}$$

$$MAD^{mn}(i,j)=\frac{1}{N^2}\sum_{r=-N/2}^{+N/2}\sum_{s=-N/2}^{+N/2}\left|I_t^{mn}(r,s)-I_{t+\tau}^{mn}(i+r,j+s)\right| \tag{4.2}$$

$$MQD^{mn}(i,j)=\sum_{r=-N/2}^{+N/2}\sum_{s=-N/2}^{+N/2}\left[I_t^{mn}(r,s)-I_{t+\tau}^{mn}(i+r,j+s)\right]^2 \tag{4.3}$$

$$C^{mn}(i,j) = \frac{\sum_{r=-N/2}^{+N/2}\sum_{s=-N/2}^{+N/2}\left[I_t^{mn}(r,s) - \bar{I}_t\right]\left[I_{t+\tau}^{mn}(i+r,j+s) - \bar{I}_{t+\tau}\right]}{\sqrt{\sum_{m=-N/2}^{+N/2}\sum_{n=-N/2}^{+N/2}\left[I_t^{mn}(r,s) - \bar{I}_t\right]^2\left[I_{t+\tau}^{mn}(i+r,j+s) - \bar{I}_{t+\tau}\right]^2}} \tag{4.4}$$

where $I_t^{mn}(r,s) = I(m+r, n+s, t)$ indicates the block centered at (m,n) in the current frame; $I_{t+\tau}^{mn}(i+r,j+s) = I(m+i+r, n+j+s, t+\tau)$ corresponds to the block centered at $(m+i, n+j)$ in the previous (or subsequent) frame; $\bar{I}_t$ and $\bar{I}_{t+\tau}$ represent the means of intensity values in the current block and in the previous (or subsequent) one, respectively.

General Remarks

The algorithms mentioned above, as well as many others, clearly show the promises of video microscopy as a valid approach to investigate cardiac cell functionality. However, a few remarks are worth to be mentioned.

- Using the average velocity as a beating signal can be affected by noise when including the non-moving areas near the cell boundaries. A clean-up strategy might be considered to concentrate on CMs motion. Two pre-processing algorithms were tested by [211]: (1) global edge detection to identify cellular regions or (2) a moving foreground detector. Of note, both methods present some limitations since CMs usually have no clear boundaries in brightfield and thus traditional texture or intensity-based segmentation do not work. Likewise, motion-based segmentation might be not trivial when synchronous beating cells have very different trajectories [205].

- When clusters or immature single cells, like hiPSC-CMs, are analyzed multiple beating areas might be present. Average motion vector amplitudes without regard to the directionality of the vectors can result in temporal and spatial information loss. Indeed, it has been demonstrated that under certain conditions, multiple peaks can be embedded within a single peak in an average motion vector displacement trace [212]. To overcome this limitation, expensive high-speed cameras are often required [208].

- Beating signals extracted from average velocity do not provide directional information (i.e., contraction and relaxation peaks are both positive). For a directional signal, a frame of reference would need to be set, as was done by [210], [211].

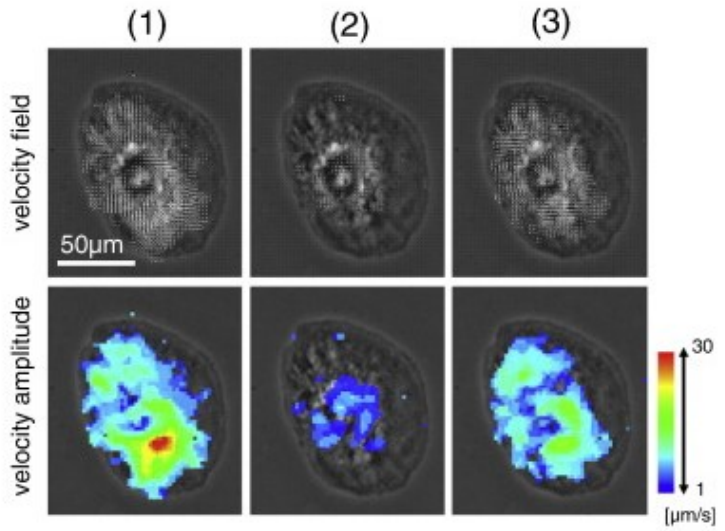

(a)

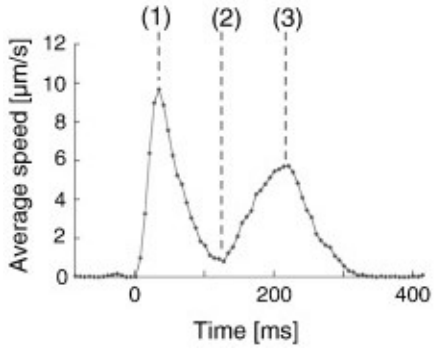

(b)

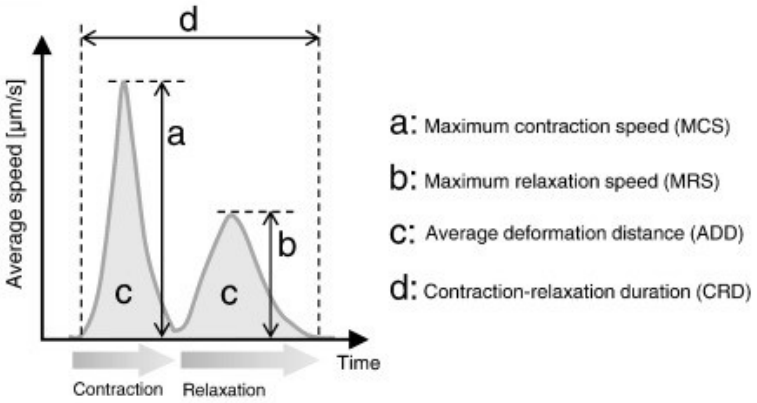

(c)

Motion vectors detected during the contraction and relaxation process of a single cell. *(a) The contractile motion of an hiPSC-CM computed with motion vector analysis. In the upper panels, motion vectors show the velocity field at contraction (1), at the end of contraction, (2) and during relaxation (3). The bottom panels show the visualized amplitude of the velocity field in a heat-map style that corresponds to the upper panels. (b) Example of a motion waveform retrieved averaging the motion vectors at each frame. Points (1) corresponds to the contraction peak and point (3) indicates the relaxation peak. (c) Schematics of a motion waveform of contraction–relaxation obtained with motion vector analysis and the contractile parameters that can be extracted. Reproduce from [209]*

Proposed algorithm

The procedure used in this thesis work for generating beating signals from hiPSC-CMs is slightly different from the algorithms presented above. The basic assumption is the same: during contraction, the cell body retracts towards a focal point, it remains contracted for a while, and then it relaxes. Differently from the aforementioned approaches, in the proposed algorithm the motion vector is not used to compute the average velocity.
The code has been developed to ask the user to define a ROI around a single cell or a cluster of cells that are beating synchronously. The identified region is then divided into concentric subregions and each one is analyzed separately. This is done to assure that the beating signal would be not affected by the noise of surrounding areas. For each subregion, the code tracks across the video frames a set of *feature* points located on the body of the cell. From this tracking process, the algorithm estimates the cell body motion field and exploits this information to translate, rotate, or scale a bounding box centered around the cell. The beating signal is obtained computing the area of this bounding box. When a cell contracts, the algorithm tracks body *features* that retract towards a center point, which means that the estimated geometric transformation would shrink the tracking box, reducing its area. On the contrary, when a cell relaxes, the algorithm tracks body *features* that move radially away from the center point. Consequently, the estimated geometric transformation would scale the tracking box, increasing its size. The minima of the tracking box area represent the cell contractions and their frequency is a good estimator of cell contraction rate.

Three major differences can be highlighted w.r.t. the block-matching algorithms: (1) a differential method is used to retrieve the motion field instead of a block-based one, (2) *features* are tracked instead of blocks, and (3) the beating signal is computed as the area of the tracking box rather than as the average motion.

Kanade-Lucas-Tomasi tracking algorithm

The traditional image registration problem can be characterized as follows: given two images $I(\mathbf{x})$ and $J(\mathbf{x})$, where $\mathbf{x}$ is a vector of coordinates in two images, the registration problem requires to find the disparity vector δ that minimizes some measure of the difference between $\mathrm{I}(\mathbf{x} + \delta)$ and $\mathrm{J}(\mathbf{x})$, with $\mathbf{x}$ that change in some region of interest. Several methods have been developed to deal with image registration problems and retrieve motion fields. Among these, *optical flow* methods are one of the most widely used approaches in computer vision. The two basic assumptions of *optical flow* methods are *brightness constancy* and *spatial coherence*. *Brightness constancy* means that the brightness/intensity of a point in $I(\mathbf{x})$ is the same in $J(\mathbf{x})$. *Spatial coherence*, instead, means that there is a very small movement of a point in two consecutive frames. From this two statement the *optical flow* equation can be easily retrieved:

$$\begin{cases} J(x,y) = I(x+u, y+v) \\ I(x+u, y+v) = I(x,y) + \frac{\partial I}{\partial x}u + \frac{\partial I}{\partial y}v + \mathcal{O} \end{cases} \tag{4.5}$$

It follows:

$$I_t - \nabla I \cdot [u\ v] = 0 \tag{4.6}$$

where $\mathcal{O}$ indicates higher-order terms that can be neglected for small motion fields and I_t corresponds to the time derivative of the image at $\mathbf{x}$. The system presents two unknowns and only one equation.

In 1981, Bruce D. Lucas and Takeo Kanade [15] developed a differential method to solve the optical flow problem stated above. The *Lucas-Kanade* method assumes that the flow is essentially constant in a local neighborhood of the pixel under consideration, and solves the basic optical flow equation for all the pixels in that small neighborhood. When this algorithm is applied in tracking, it is commonly referred to as the *Kanade-Lucas-Tomasi tracking algorithm* due to the ausiliar *feature* extraction procedure proposed by Jianbo Shi and Carlo Tomasi in 1993.

The algorithm approach according to [15]–[17] is summarized below.

Displacements Estimation Tomasi and Kanade have shown that *pure translation* motion fields are more suitable rather than *affinity models* when small *displacements* are expected from frame to frame. Indeed, the danger of over-parametrizing the system might outweigh the advantages of a more accurate model [15], [16]. Accordingly, since the *pure translation* considers a *displacement* vector $\delta = \mathbf{d}$), the resulting local image model is:

$$J(x) = I(x - d) + n(x) \tag{4.7}$$

where $J(x) = I(x, y, t+\tau)$, $I(\mathbf{x}-\mathbf{d}) = I(x-\xi, y-\eta, t)$ and the displacement vector $d = (\xi, \eta)$. The noise is indicated by the term $n(x)$.
The displacement vector $\mathbf{d}$ is then chosen to minimize the residue error, which is defined by the following double integral over the given window W:

$$\varepsilon = \int_W [I(\mathbf{x} - \mathbf{d}) - J(\mathbf{x})]^2 w d\mathbf{x} \tag{4.8}$$

In Eq. 4.8, w is a weighting function. It can be set as a Gaussian-like function to emphasize more the central area of the window or dependent on the image intensities to de-emphasize particular regions.

The registration problem can be posed as the minimization of the error residue defined by the equation, which means finding $\mathbf{d}$ that minimize the *dissimilarity* between $J(x)$ and $I(x - d)$. When images are taken at near time instants the intensities' patterns are similar, since the scene is expected to be only slightly different between the two frames. In these cases, the displacement vector is small and the intensity function can be approximated by its Taylor series truncated to the linear term:

$$I(\mathbf{x} - \mathbf{d}) = I(\mathbf{x}) - \mathbf{g} \cdot \mathbf{d} \tag{4.9}$$

where the image gradient $\mathbf{g}$ is defined as

$$\mathbf{g} = \left(\frac{\partial I}{\partial x}, \frac{\partial I}{\partial y} \right)^T \tag{4.10}$$

As a consequence, the residue defined in Eq.4.8 can be written as

$$\varepsilon = \int_W [I(\mathbf{x}) - \mathbf{g} \cdot \mathbf{d} - J(\mathbf{x})]^2 w d\mathbf{x} = \int_W [h - \mathbf{g} \cdot \mathbf{d}]^2 w d\mathbf{x} \tag{4.11}$$

where $h = I(x) \quad J(x)$.

Differentiating the Eq.4.11 w.r.t. $\mathbf{d}$ and setting the result equal to zero yields the following vector equation:

$$\frac{\partial \varepsilon}{\partial \mathbf{d}} = 0 \tag{4.12}$$

$$\int_W [h - \mathbf{g} \cdot \mathbf{d}] \ \mathbf{g} \ w \ dA = 0 \tag{4.13}$$

Since $(\mathbf{g} \cdot \mathbf{d})\mathbf{g} = (\mathbf{g}\mathbf{g}^T)\mathbf{d}$, and $\mathbf{d}$ is assumed to be constant within the small window W, Eq.4.13 can be written as:

$$(\int_W \mathbf{g}\mathbf{g}^T \ w \ dA)\mathbf{d} = \int_W h \ \mathbf{g} \ w \ dA \tag{4.14}$$

The matrix notation is:

$$G\mathbf{d} = \mathbf{e} \tag{4.15}$$

where the coefficient matrix is the symmetric, 2×2 matrix

$$G = \int_W \mathbf{g}\mathbf{g}^T \ w \ dA = \begin{vmatrix} g_x^2 & g_x g_y \\ g_y g_x & g_y^2 \end{vmatrix} \tag{4.16}$$

and the right-hand side is the two-dimensional vector

$$\mathbf{e} = \int_W (I - J) \ \mathbf{g} \ w \ dA = \int_W (I - J) \begin{vmatrix} g_x \\ g_y \end{vmatrix} \ w \ dA \tag{4.17}$$

To sum up, the tracking procedure requires to:

1. Estimate the gradient for every pair of adjacent frames and computing their second order moment to compute the 2 x 2 matrix G
2. Multiply the difference between the two frames with the gradient computed above to retrieve the vector **e**.
3. Solve the system reported in Eq.4.15 to obtain a measure for the displacement **d**.

.

Solving the optical flow equation, the tracker tracks each point from the previous to the current frame: *forward tracking*. After that, the same point is projected back to the previous frame. The forward-backward error is computed. The feature is retained for the following frame analysis only if the bidirectional error is below a certain fixed threshold. This allows eliminating points that could not be reliably tracked.

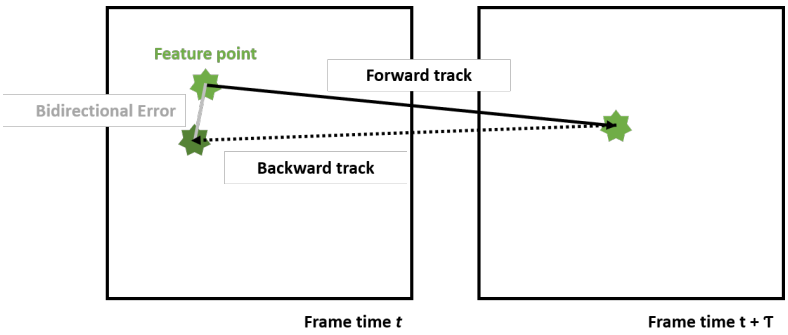

Kanade-Lucas-Tomasi feature-tracking algorithm. *The algorithm steps can be summarized as follow: (1) identify the feature points in a frame at time t (green start); (2) solve the optical flow equation and estimate the displacement of the feature point (forward tracking); (3) track the same point back to the previous frame; (4) compute the bidirectional error; (5) retain the feature point if the forward-backward error is below a certain threshold.*

Features Selection Of note, not all parts of an image contain motion information. For instance, only the vertical component of motion can be determined for a horizontal intensity edge and only the horizontal component of motion can be determined for a vertical intensity edge. This problem is called the *aperture problem*.

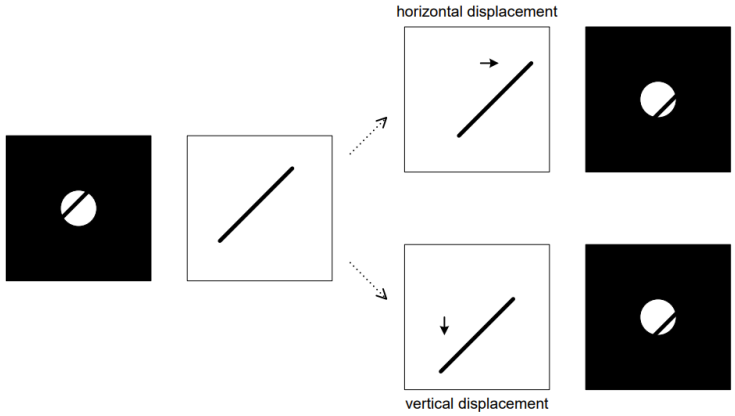

Aperture problem. *When observing a moving structure through a small aperture, different physical motions appear indistinguishable: (top-right) bar with horizontal displacement seen through aperture, (bottom-right) bar with vertical displacement seen through aperture. Reproduce from [213]*

Thus, *feature* windows must be selected based on some measure of *texturedness* or *cornerness*, since this kind of *features* contains complete motion information. Over the last decades, researchers have proposed to track corners [214], or windows with a high standard deviation in the spatial intensity profile [215] or with the presence of zero crossings of the Laplacian of the image intensity [216]. These *features* are intuitive, but not always optimal for the tracking algorithm to produce reliable results.

On the contrary, the *features* proposed by C. Tomasi and T. Kanade in 1993 are *good* by construction [16]. The basic principle is that a window can be tracked

from frame to frame if system 4.15 represents good measurements and if it can be solved reliably. That means that the 2 x 2 coefficient matrix G of the system must be both above the image noise level and well-conditioned [15], [16].
The noise requirement implies that both eigenvalues of G must be large. Two small eigenvalues mean a roughly constant intensity profile within a window. A large and a small eigenvalue correspond to a unidirectional pattern. Two large eigenvalues can represent corners, salt-and-pepper textures, or many other patterns.
The conditioning requirement means that the eigenvalues of G cannot differ by several orders of magnitude. This condition is normally satisfied, since the intensity variations in a window are bounded by the maximum allowable pixel value, thus the greater eigenvalue cannot be arbitrarily large.
In practice, given $\lambda 1$, $\lambda 2$ the two eigenvalues of G, a window is regarded as good when

$$min(\lambda 1, \lambda 2) > \lambda \tag{4.18}$$

where λ is a predefined threshold, chosen halfway in-between the eigenvalues for a region of approximately uniform brightness and the eigenvalues for a well-known *feature*, such as a corner or a highly textured region. This *feature* selection method maximizes the quality of tracking, and is therefore optimal by construction, as opposed to more *ad hoc* measures of *texturedness*.

Features Quality Monitoring A *feature* with a high texture content, obtained according to the method described previously, can still be a bad *feature* to track. For instance, the tracked *feature* can be associated with a point that does not exist in the real world[3], making that *feature* useless or even harmful to the displacement estimate. On the contrary, the algorithm proposed by Shi and Tomasi, and adopted in this work, use a measure of dissimilarity to monitor the *features*' quality along the tracking process [17]. Remarkably, due to a large number of frames through which a given *feature* can be tracked, the dissimilarity measure would not work well with a pure *translation model*. On the contrary, an *affine motion field* should be considered.

In this case:

$$\delta = \mathbf{D}\mathbf{x} + \mathbf{d} \tag{4.19}$$

where

$$\mathbf{D} = \begin{vmatrix} d_{xx} & d_{xy} \\ d_{yx} & d_{yy} \end{vmatrix} \tag{4.20}$$

A point $\mathbf{x}$ in the first image I moves to point $A\mathbf{x} + d$ in the second image J, with $A = 1 + \boldsymbol{D}$ and 1 is the 2 x 2 identity matrix.

The measure of *dissimilarity* can be written as follow:

$$\varepsilon = \int_W [I(A\mathbf{x} + \mathbf{d}) - J(\mathbf{x})]^2 \; w \; d\mathbf{x} \tag{4.21}$$

[3]For instance, branches of a tree at different depths and orientations can create intersections in the image. Any selection criterion would pick the intersection as a good *feature* to track, though this point does not correspond to a physical point in the world and thus it will not be tracked easily and reliably.

To minimize the residual as computed in Eq. 4.21, ε is differentiated w.r.t. the unknown matrix $\boldsymbol{D}$ and the displacement vector d and set the result to zero. The resulting system is then linearized by the truncated Taylor expansion:

$$I(Ax + \mathbf{d}) = I(x) + \mathbf{g}^T(\mathbf{u}) \tag{4.22}$$

Combining the differential of Eq.4.21 w.r.t. $\boldsymbol{D}$ and $\mathbf{d}$ with the linearization of Eq.4.22, a linear 6 x 6 system can be retrieved. Solving it, the unknown coefficients of $\boldsymbol{D}$ and $\mathbf{d}$ can be computed. These estimates enable to obtain a measure of the dissimilarity (Eq.4.21). Finally, good and bad *features* can be discriminated considering the affine motion dissimilarity as a function of the video frames. When the dissimilarity exceeds the mean dissimilarity value, the feature should be discarded.

Validation

To validate the video-based algorithm for cell contractility evaluation several methods can be used. Calcium measurements and current clamp measurements during video recording are two widely used approaches for combined functionality verification [209]. The former verify that the fluorescence oscillations are consistent with the motion vector oscillations. The latter, instead, evaluate the coherence between membrane properties and contractility behavior [210], [211].
Another strategy is to assess the validity of the algorithm using different sets of synthesized pair of images. In this case, the user already known the target intensity displacement fields and can verify that the algorithm returns the same results [207].
The first-line validation, however, can be easily be performed manually. A trained user can count the number of beats (contraction–relaxation cycles) that are visible in the video and then verify that the counted number corresponds to the number of contractions estimated by the algorithm [211].

This user-based validation method has been used to assess the validity of the proposed algorithm for contraction rate estimation. The approach was selected due to its simplicity and since it provides rapid confirmation without the need to perform more complex experiments.

Further Improvements

The results obtained confirm that video microscopy offers several advantages for cardiac cells characterization w.r.t. more complex experimental assays.
However, the algorithm proposed can be improved for following analysis. Further improvements could be:

- Avoid manually selected definition of ROIs. The process could be ideally automatized to detect cell bodies. Possible methods vary from the simple edge-detection of motion-based segmentation approaches [211] to the more complex pixel clustering method [205]. Noticeably, these automatic strategies are not always reliable due to the high variability of cells and the difficulties in setting software parameters. Thus, overall, one might prefer to spend more time selecting the analysis regions rather than obtain unexpected results.

- Reduce computational time. This version of the code repeats the tracking process for each subarea of the initially defined ROI (see Paragraph 2.3.1). This is done to avoid that surrounding areas affect the measures of cell contraction rate. However, it comes at the cost of dramatically increasing the computational cost. Other solutions could be exploited to clean up the signal and enhance the signal to noise ratio. Three cleaning algorithms have been explored by [211]: amplitude-based cleaning, vector-based cleaning, and frequency domain cleaning. If effective these cleaning procedures would allow avoiding subareas analysis, finally resulting a faster video processing. The *features* belonging to a single pre-processed ROI would be tracked. This will reduce computational time while keeping the measurements accurate.

- Extract other contractility measures. At the moment, the code assesses only the contraction rate of cardiac cells, but other functional properties might be extracted. For instance, a measure of contraction variability within the *running observation window* could provide enhanced information about cell behavior. Likewise, a measure of average velocity could be also added.

Acronyms

AF	Atrial Fibrillation
AP	Action potential
APD	Action Potential Duration
ARP	Absolute Refractory Period
ATP	Adenosin Triphospate
ATPase	Adenosin Triphosphatase
AzoTAB	Azobenzene Trimethylammonium Bromide
ChR2	Channelrodopsin 3
CMC	Cardiomyocytes
CR	Contraction Rate
DAD	Delayed After-Depolarization
DF	Degree of Freedom
DMSO	Dimethyl Sulfoxide
EAD	Early After Depolarization
ECG	Electrocardiogram
ER	Endoplasmatic Reticulum
ERP	Effective Refractory Period
GJ	Gap Junction
iPSC	HumanInduced Pluripotent Stem Cell
ICD	Implantable Cardioverter Defibrillator
IR	Infrared Radiation
KLT	Kanade-Lucas-Tomasi
KRH	Krebs-Ringer Buffer

PA	Photoinduced Absorption
PB	Photobleaching
PL	Photoluminescence
PSC	Pluripotent Stem Cell
RyR2	Ryanodine Receptor 2
RMP	Resting Membrane Potential
ROI	Region of Interest
ROW	Running Observation Window
RRP	Relative Refractory Period
SCD	Sudden Cardiac Death
SD	Standard Deviation
SDS	Sodium Dodecyl Sulfate
SE	Stimulated Emission
s.e.m.	Standard Error of the Mean
SNP	Super Normal Period
SR	Sarcoplasmatic Reticulum
S-ICD	Subcutaneous Implantable Cardioverter Defibrillator
TA	Transient Absorption
TMP	Transmembrane Potential
ULV	Upper Limit Vulnerability
VF	Ventricular Fibrillation
w.r.t.	With Respect To

References

[1] H. G. Mond e A. Proclemer, "The 11th world survey of cardiac pacing and implantable cardioverter-defibrillators: Calendar year 2009–a world society of arrhythmia's project", *Pacing and clinical electrophysiology*, vol. 34, n. 8, 2011.

[2] R. G. Hauser, D. L. Hayes, L. M. Kallinen, D. S. Cannom, A. E. Epstein, A. K. Almquist, S. L. Song, G. F. O. Tyers, S. C. Vlay e M. Irwin, "Clinical experience with pacemaker pulse generators and transvenous leads: An 8-year prospective multicenter study", *Heart Rhythm*, vol. 4, n. 2, 2007.

[3] A. S. Manolis, T. Maounis, S. Koulouris e V. Vassilikos, "
real life" longevity of implantable cardioverter-defibrillator devices", *Clinical Cardiology*, vol. 40, n. 9, 2017.

[4] J. Baumert, C. Schmitt e K. Ladwig, "Psychophysiologic and affective parameters associated with pain intensity of cardiac cardioverter defibrillator shock discharges", *Psychosomatic medicine*, vol. 68, n. 4, 2006.

[5] P. Sasse, *Optical pacing of the heart: The long way to enlightenment*, 2011.

[6] P. M. Boyle, T. V. Karathanos e N. A. Trayanova, "Cardiac optogenetics: 2018", *JACC Clinical Electrophysiology*, vol. 4, n. 2, 2018.

[7] P. Sasse, M. Funken, T. Beiert e T. Bruegmann, "Optogenetic termination of cardiac arrhythmia: Mechanistic enlightenment and therapeutic application?", *Frontiers in physiology*, vol. 10, 2019.

[8] T. Bruegmann, D. Malan, M. Hesse, T. Beiert, C. J. Fuegemann, B. K. Fleischmann e P. Sasse, "Optogenetic control of heart muscle in vitro and in vivo", *Nature methods*, vol. 7, n. 11, 2010.

[9] T. Bruegmann, P. M. Boyle, C. C. Vogt, T. V. Karathanos, H. J. Arevalo, B. K. Fleischmann, N. A. Trayanova, P. Sasse et al., "Optogenetic defibrillation terminates ventricular arrhythmia in mouse hearts and human simulations", *The Journal of clinical investigation*, vol. 126, n. 10, 2016.

[10] F. Lodola, V. Vurro, S. Crasto, E. Di Pasquale e G. Lanzani, "Optical pacing of human-induced pluripotent stem cell-derived cardiomyocytes mediated by a conjugated polymer interface", *Advanced healthcare materials*, vol. 8, n. 13, 2019.

[11] R. Parameswaran, K. Koehler, M. Y. Rotenberg, M. J. Burke, J. Kim, K. Jeong, B. Hissa, M. D. Paul, K. Moreno, N. Sarma et al., "Optical stimulation of cardiac cells with a polymer-supported silicon nanowire matrix", *Proceedings of the National Academy of Sciences*, vol. 116, n. 2, 2019.

[12] M. L. DiFrancesco, F. Lodola, E. Colombo, L. Maragliano, M. Bramini, G. M. Paternò, P. Baldelli, M. Dalla Serra, L. Lunelli, M. Marchioretto et al., "Neuronal firing modulation by a membrane-targeted photoswitch", *Nature Nanotechnology*, vol. 15, n. 4, 2020.

[13] D. M. Bers, "Cardiac excitation–contraction coupling", *Nature*, vol. 415, n. 6868, 2002.

[14] C. S. Chung e K. S. Campbell, "Temperature and transmural region influence functional measurements in unloaded left ventricular cardiomyocytes", *Physiological reports*, vol. 1, n. 6, 2013.

[15] B. D. Lucas, T. Kanade et al., "An iterative image registration technique with an application to stereo vision", 1981.

[16] C. Tomasi e T. Kanade, "Shape and motion from image streams: A factorization method", *Proceedings of the National Academy of Sciences*, vol. 90, n. 21, 1993.

[17] J. Shi e C. Tomasi, "Good features to track", in *1994 Proceedings of IEEE conference on computer vision and pattern recognition*, IEEE, 1994.

[18] G. M. Paternò, E. Colombo, V. Vurro, F. Lodola, S. Cimò, V. Sesti, E. Molotokaite, M. Bramini, L. Ganzer, D. Fazzi et al., "Membrane environment enables ultrafast isomerization of amphiphilic azobenzene", *Advanced Science*, vol. 7, n. 8, 2020.

[19] M. De Menorval, L. M. Mir, M. L. Fernández e R. Reigada, "Effects of dimethyl sulfoxide in cholesterol-containing lipid membranes: A comparative study of experiments in silico and with cells", *PloS one*, vol. 7, n. 7, 2012.

[20] N. Magome, G. Kanaporis, N. Moisan, K. Tanaka e K. Agladze, "Photocontrol of excitation waves in cardiomyocyte tissue culture", *Tissue Engineering Part A*, vol. 17, n. 21-22, 2011.

[21] S. R. Frolova, O. Gaiko, V. A. Tsvelaya, O. Y. Pimenov e K. I. Agladze, "Photocontrol of voltage-gated ion channel activity by azobenzene trimethylammonium bromide in neonatal rat cardiomyocytes", *Plos one*, vol. 11, n. 3, 2016.

[22] S. R. Frolova, V. S. Gorbunov, N. S. Shubina, A. M. Perepukhov, S. G. Romanova e K. I. Agladze, "Stilbene derivative as a photosensitive compound to control the excitability of neonatal rat cardiomyocytes", *Bioscience reports*, vol. 39, n. 1, 2019.

[23] F. Riefolo, C. Matera, A. Garrido-Charles, A. M. J. Gomila, R. Sortino, L. Agnetta, E. Claro, R. Masgrau, U. Holzgrabe, M. Batlle et al., "Optical control of cardiac function with a photoswitchable muscarinic agonist", *Journal of the American Chemical Society*, vol. 141, n. 18, 2019.

[24] S. Khurshid, S. H. Choi, L. Weng, E. Y. Wang, L. Trinquart, E. J. Benjamin, P. T. Ellinor e S. A. Lubitz, "Frequency of cardiac rhythm abnormalities in a half million adults", *Circulation: Arrhythmia and Electrophysiology*, vol. 11, n. 7, 2018.

[25] *Prevention and treatment of arrhythmia*, American Heart Association. (accessed: 04.2020).

[26] *Arrhythmia*, National Heart, Lung, and Blood Institute. (accessed: 04.2020).

[27] *Patient care health information - diseases conditions*, Mayo-Clinic. (accessed: 04.2020).

[28] S. G. Priori, C. Blomström-Lundqvist, A. Mazzanti, N. Blom, M. Borggrefe, J. Camm, P. M. Elliott, D. Fitzsimons, R. Hatala et al., "2015 esc guidelines for the management of patients with ventricular arrhythmias and the prevention of sudden cardiac death: The task force for the management of patients with ventricular arrhythmias and the prevention of sudden cardiac death of the european society of cardiology (esc) endorsed by: Association for european paediatric and congenital cardiology (aepc)", *Ep Europace*, vol. 17, n. 11, 2015.

[29] R. Mehra, "Global public health problem of sudden cardiac death", *Journal of electrocardiology*, vol. 40, n. 6, 2007.

[30] B. L. Wilkoff, B. D. Williamson, R. S. Stern, S. L. Moore, F. Lu, S. W. Lee, U. M. Birgersdotter-Green, M. S. Wathen, I. C. Van Gelder, B. M. Heubner et al., "Strategic programming of detection and therapy parameters in implantable cardioverter-defibrillators reduces shocks in primary prevention patients: Results from the prepare (primary prevention parameters evaluation) study", *Journal of the American College of Cardiology*, vol. 52, n. 7, 2008.

[31] M. Zabel, R. Willems, A. Lubinski, A. Bauer, J. Brugada, D. Conen, P. Flevari, G. Hasenfuß, M. Svetlosak, H. V. Huikuri et al., "Clinical effectiveness of primary prevention implantable cardioverter-defibrillators: Results of the eu-cert-icd controlled multicentre cohort study", *European Heart Journal*, vol. 2020, 2020.

[32] P. Alter, S. Waldhans, E. Plachta, R. Moosdorf e W. Grimm, "Complications of implantable cardioverter defibrillator therapy in 440 consecutive patients", *Pacing and Clinical Electrophysiology*, vol. 28, n. 9, 2005.

[33] V. A. Ezzat, V. Lee, S. Ahsan, A. W. Chow, O. Segal, E. Rowland, M. D. Lowe e P. D. Lambiase, "A systematic review of icd complications in randomised controlled trials versus registries: Is our 'real-world'data an underestimation?", *Open Heart*, vol. 2, n. 1, 2015.

[34] J. B. Van Rees, M. K. De Bie, J. Thijssen, C. J. W. Borleffs, M. J. Schalij e L. Van Erven, "Implantation-related complications of implantable cardioverter-defibrillators and cardiac resynchronization therapy devices: A systematic review of randomized clinical trials", *Journal of the American College of Cardiology*, vol. 58, n. 10, 2011.

[35] R. A. Sham'a, P. Nery, M. Sadek, D. Yung, C. Redpath, M. Perrin, B. Sarak e D. Birnie, "Myocardial injury secondary to icd shocks: Insights from patients with lead fracture", *Pacing and Clinical Electrophysiology*, vol. 37, n. 2, 2014.

[36] G. Magyar-Russell, B. D. Thombs, J. X. Cai, T. Baveja, E. A. Kuhl, P. P. Singh, M. M. B. Barroso, E. Arthurs, M. Roseman, N. Amin et al., "The prevalence of anxiety and depression in adults with implantable cardioverter defibrillators: A systematic review", *Journal of psychosomatic research*, vol. 71, n. 4, 2011.

[37] D. Ummarino, "Optogenetic control of cardiac rhythm", *Nature Review Cardiology*, vol. 14, 2017.

[38] F. Di Maria, F. Lodola, E. Zucchetti, F. Benfenati e G. Lanzani, "The evolution of artificial light actuators in living systems: From planar to nanostructured interfaces", *Chemical Society Reviews*, vol. 47, n. 13, 2018.

[39] L. Samaranch, W. San Sebastian, A. P. Kells, E. A. Salegio, G. Heller, J. R. Bringas, P. Pivirotto, S. DeArmond, J. Forsayeth e K. S. Bankiewicz, "Aav9-mediated expression of a non-self protein in nonhuman primate central nervous system triggers widespread neuroinflammation driven by antigen-presenting cell transduction", *Molecular Therapy*, vol. 22, n. 2, 2014.

[40] J. Loscalzo. MCGraw-Hill Medical, 2017.

[41] S. Rohr, "Arrhythmogenic implications of fibroblast-myocyte interactions", *Circulation: Arrhythmia and Electrophysiology*, vol. 5, n. 2, 2012.

[42] S. I. Assaad, P. M. Heerdt e G. J. Crystal, "Cardiovascular physiology: Cellular and molecular regulation", in *Pharmacology and Physiology for Anesthesia*, Elsevier, 2019.

[43] Z. Issa, J. M. Miller e D. P. Zipes, "1 - molecular mechanisms of cardiac electrical activity", in *Clinical Arrhythmology and Electrophysiology: A Companion to Braunwald's Heart Disease*, Elsevier, cur., Third Edition, 2019.

[44] S. Dhein, T. Seidel, A. Salameh, J. Jozwiak, A. Hagen, M. Kostelka, G. Hindricks e F. Mohr, "Remodeling of cardiac passive electrical properties and susceptibility to ventricular and atrial arrhythmias", *Frontiers in physiology*, vol. 5, 2014.

[45] W. C. De Mello, "Intercellular communication in cardiac muscle.", *Circulation research*, vol. 51, n. 1, 1982.

[46] F. Sheikh, R. S. Ross e J. Chen, "Cell-cell connection to cardiac disease", *Trends in cardiovascular medicine*, vol. 19, n. 6, 2009.

[47] *Cardiac arrhythmias*, Textbook of Cardiology. (accessed: 04.2020).

[48] M. Baruscotti, A. Barbuti e A. Bucchi, "The cardiac pacemaker current", *Journal of molecular and cellular cardiology*, vol. 48, n. 1, 2010.

[49] J. R. Balser, "Structure and function of the cardiac sodium channels", *Cardiovascular research*, vol. 42, n. 2, 1999.

[50] D. L. Kunze, A. E. Lacerda, D. L. Wilson e A. M. Brown, "Cardiac na currents and the inactivating, reopening, and waiting properties of single cardiac na channels.", *The Journal of general physiology*, vol. 86, n. 5, 1985.

[51] J. R. Hume, W. Giles, K. Robinson, E. F. Shibata, R. D. Nathan, K. Kanai e R. Rasmusson, "A time-and voltage-dependent k+ current in single cardiac cells from bullfrog atrium.", *The Journal of general physiology*, vol. 88, n. 6, 1986.

[52] G. Ikonnikov e D. Yelle, *Physiology of cardiac conduction and contractility*, (accessed: 04.2020).

[53] N. A. Mark Estesll e J. Weinstock, *Guidelines for cardiac arrhythmias: Practice makes progress*, 2011.

[54] C. H. Papadopoulos, D. Oikonomidis, E. Lazaris e P. Nihoyannopoulos, "Echocardiography and cardiac arrhythmias", *Hellenic Journal of Cardiology*, vol. 59, n. 3, 2018.

[55] J. Brugada, D. G. Katritsis, E. Arbelo, F. Arribas, J. J. Bax, C. Blomström-Lundqvist, H. Calkins, D. Corrado, S. G. Deftereos, G. Diller et al., "2019 esc guidelines for the management of patients with supraventricular tachycardiathe task force for the management of patients with supraventricular tachycardia of the european society of cardiology (esc) developed in collaboration with the association for european paediatric and congenital cardiology (aepc)", *European heart journal*, 2020.

[56] S. M. Al-Khatib, W. G. Stevenson, M. J. Ackerman, W. J. Bryant, D. J. Callans, A. B. Curtis, B. J. Deal, T. Dickfeld, M. E. Field, G. C. Fonarow et al., "2017 aha-acc-hrs guideline for management of patients with ventricular arrhythmias and the prevention of sudden cardiac death: A report of the american college of cardiology/american heart association task force on clinical practice guidelines and the heart rhythm society", *Journal of the American College of Cardiology*, vol. 72, n. 14, 2018.

[57] F. M. Kusumoto, M. H. Schoenfeld, C. Barrett, J. R. Edgerton, K. A. Ellenbogen, M. R. Gold, N. F. Goldschlager, R. M. Hamilton, J. A. Joglar, R. J. Kim et al., "2018 acc-aha-hrs guideline on the evaluation and management of patients with bradycardia and cardiac conduction delay: Executive summary: A report of the american college of cardiology/american heart association task force on clinical practice guidelines, and the heart rhythm society", *Journal of the American College of Cardiology*, 2018.

[58] D. L. Hayes e P. A. Friedman, *Cardiac pacing, defibrillation and resynchronization: a clinical approach*. John Wiley & Sons, 2011.

[59] L. Gaztañaga, F. E. Marchlinski e B. P. Betensky, "Mechanisms of cardiac arrhythmias", *Revista Española de Cardiologıa (English Edition)*, vol. 65, n. 2, 2012.

[60] D. P. Zipes, "Mechanisms of clinical arrhythmias", *Journal of Cardiovascular Electrophysiology*, vol. 14, n. 8, 2003.

[61] M. E. Mangoni e J. Nargeot, "Genesis and regulation of the heart automaticity", *Physiological reviews*, vol. 88, n. 3, 2008.

[62] W. T. Clusin, "Calcium and cardiac arrhythmias: Dads, eads, and alternans", *Critical reviews in clinical laboratory sciences*, vol. 40, n. 3, 2003.

[63] A. L. Wit, "Afterdepolarizations and triggered activity as a mechanism for clinical arrhythmias", *Pacing and Clinical Electrophysiology*, vol. 41, n. 8, 2018.

[64] A. G. Kléber e Y. Rudy, "Basic mechanisms of cardiac impulse propagation and associated arrhythmias", *Physiological reviews*, 2004.

[65] M. A. Allessie, F. I. Bonke e F. J. Schopman, "Circus movement in rabbit atrial muscle as a mechanism of tachycardia. iii. the" leading circle" concept: A new model of circus movement in cardiac tissue without the involvement of an anatomical obstacle.", *Circulation research*, vol. 41, n. 1, 1977.

[66] M. S. Spach e M. E. Josephson, "Initiating reentry: The role of nonuniform anisotropy in small circuits", *Journal of cardiovascular electrophysiology*, vol. 5, n. 2, 1994.

[67] J. M. Davidenko, P. Kent e J. Jalife, "Spiral waves in normal isolated ventricular muscle", *Physica D: Nonlinear Phenomena*, vol. 49, n. 1-2, 1991.

[68] J. A. Hopps, "The development of the pacemaker", *Pacing and Clinical Electrophysiology*, vol. 4, n. 1, 1981.

[69] H. U. Klein e S. Nisam, "Michel mirowski and the beginning of a new era of fighting sudden arrhythmic death", *Herzschrittmachertherapie+ Elektrophysiologie*, vol. 26, n. 2, 2015.

[70] M. Mirowski, P. R. Reid, M. M. Mower, L. Watkins, V. L. Gott, J. F. Schauble, A. Langer, M. S. Heilman, S. A. Kolenik, R. E. Fischell et al., "Termination of malignant ventricular arrhythmias with an implanted automatic defibrillator in human beings", *N Engl j Med*, vol. 303, n. 6, 1980.

[71] F. G. Akar, B. J. Roth e D. S. Rosenbaum, "Optical measurement of cell-to-cell coupling in intact heart using subthreshold electrical stimulation", *American Journal of Physiology-Heart and Circulatory Physiology*, vol. 281, n. 2, 2001.

[72] D. J. Dosdall, V. G. Fast e R. E. Ideker, "Mechanisms of defibrillation", *Annual review of biomedical engineering*, vol. 12, 2010.

[73] I. R. Efimov, R. A. Gray e B. J. Roth, "Virtual electrodes and deexcitation: New insights into fibrillation induction and defibrillation", *Journal of Cardiovascular Electrophysiology*, vol. 11, n. 3, 2000.

[74] K. A. Ellenbogen, B. L. Wilkoff, G. N. Kay, C. P. Lau e A. Auricchio, *Clinical Cardiac Pacing, Defibrillation and Resynchronization Therapy*. Elsevier Health Sciences, 2016.

[75] S. S. Barold, *Modern cardiac pacing*. Wiley-Blackwell, 1985.

[76] M. Shah e E. Cuvillier, "Clinically relevant basics of pacing and defibrillation", *Cardiac Pacing and Defibrillation in Pediatric and Congenital Heart Disease*, 2017.

[77] G. M. Calvagna, G. Torrisi, C. Giuffrida e S. Patanè, "Pacemaker, implantable cardioverter defibrillator, crt, crt-d, psychological difficulties and quality of life", *International Journal of Cardiology*, vol. 174, n. 2, 2014.

[78] D. Z. Uslan, M. J. Gleva, D. K. Warren, T. Mela, M. K. Chung, V. Gottipaty, R. Borge, D. Dan, T. Shinn, K. Mitchell et al., "Cardiovascular implantable electronic device replacement infections and prevention: Results from the replace registry", *Pacing and clinical electrophysiology*, vol. 35, n. 1, 2012.

[79] N. L. Gurvich e G. S. Yuniev, "Restoration of regular rhythm in the mammalian fibrillating heart.", *American review of Soviet medicine*, vol. 3, p. 236, 1946.

[80] P. D. Lambiase, C. Barr, D. A. Theuns, R. Knops, P. Neuzil, J. B. Johansen, M. Hood, S. Pedersen, S. Kääb, F. Murgatroyd et al., "Worldwide experience with a totally subcutaneous implantable defibrillator: Early results from the effortless s-icd registry", *European heart journal*, vol. 35, n. 25, 2014.

[81] M. S. Wathen, P. J. DeGroot, M. O. Sweeney, A. J. Stark, M. F. Otterness, W. O. Adkisson, R. C. Canby, K. Khalighi, C. Machado, D. S. Rubenstein et al., "Prospective randomized multicenter trial of empirical antitachycardia pacing versus shocks for spontaneous rapid ventricular tachycardia in patients with implantable cardioverter-defibrillators: Pacing fast ventricular tachycardia reduces shock therapies (painfree rx ii) trial results", *Circulation*, vol. 110, n. 17, 2004.

[82] A. Goyal, J. C. Sciammarella, L. Chhabra et al., *Synchronized electrical cardioversion*, (accessed: 04.2020).

[83] D. P. Zipes, J. Fischer, R. M. King, A. D. Nicoll e W. W. Jolly, "Termination of ventricular fibrillation in dogs by depolarizing a critical amount of myocardium", *The American journal of cardiology*, vol. 36, n. 1, 1975.

[84] P. Chen, N. Shibata, E. G. Dixon, P. D. Wolf, N. D. Danieley, M. B. Sweeney, W. M. Smith, R. E. Ideker et al., "Activation during ventricular defibrillation in open-chest dogs. evidence of complete cessation and regeneration of ventricular fibrillation after unsuccessful shocks", *The Journal of clinical investigation*, vol. 77, n. 3, 1986.

[85] P. Chen, P. D. Wolf, S. D. Melnick, N. D. Danieley, W. M. Smith e R. E. Ideker, "Comparison of activation during ventricular fibrillation and following unsuccessful defibrillation shocks in open-che.st dogs", *Circulation research*, vol. 66, n. 6, 1990.

[86] D. W. Frazier, P. D. Wolf, J. M. Wharton, A. S. Tang, W. M. Smith, R. E. Ideker et al., "Stimulus-induced critical point. mechanism for electrical initiation of reentry in normal canine myocardium", *The Journal of clinical investigation*, vol. 83, n. 3, 1989.

[87] C. D. Swerdlow, D. J. Martin, R. M. Kass, S. Davie, W. J. Mandel, E. S. Gang e P. Chen, "The zone of vulnerability to t wave shocks in humans", *Journal of cardiovascular electrophysiology*, vol. 8, n. 2, 1997.

[88] I. R. Efimov, Y. Cheng, D. R. Van Wagoner, T. Mazgalev e P. J. Tchou, "Virtual electrode–induced phase singularity: A basic mechanism of defibrillation failure", *Circulation Research*, vol. 82, n. 8, 1998.

[89] A. versus Implantable Defibrillators (AVID) Investigators, "A comparison of antiarrhythmic-drug therapy with implantable defibrillators in patients resuscitated from near-fatal ventricular arrhythmias", *New England Journal of Medicine*, vol. 337, n. 22, 1997.

[90] S. J. Connolly, M. Gent, R. S. Roberts, P. Dorian, D. Roy, R. S. Sheldon, L. B. Mitchell, M. S. Green, G. J. Klein e B. O'Brien, "Canadian implantable defibrillator study (cids) a randomized trial of the implantable cardioverter defibrillator against amiodarone", *Circulation*, vol. 101, n. 11, 2000.

[91] K. Kuck, R. Cappato, J. Siebels e R. Rüppel, "Randomized comparison of antiarrhythmic drug therapy with implantable defibrillators in patients resuscitated from cardiac arrest: The cardiac arrest study hamburg (cash)", *Circulation*, vol. 102, n. 7, 2000.

[92] T. Kleemann, T. Becker e K. Doenges, "Annual rate of transvenous defibrillation lead defects in implantable cardioverter defibrillators over a period of 10 years", *Circulation*, vol. 115, 2007.

[93] U. Dorwarth, B. Frey, M. Dugas, T. Matis, M. Fiek, M. Schmoeckel, T. Remp, I. Durchlaub, A. Gerth, G. Steinbeck et al., "Transvenous defibrillation leads: High incidence of failure during long-term follow-up", *Journal of cardiovascular electrophysiology*, vol. 14, n. 1, 2003.

[94] H. Fu, X. M. Huang, L. Zhong, M. J. Osborn, S. J. Asirvatham, R. E. Espinosa, P. A. Brady, H. Lee, K. L. Greason, L. M. Baddour et al., "Outcomes and complications of lead removal: Can we establish a risk stratification schema for a collaborative and effective approach?", *Pacing and Clinical Electrophysiology*, vol. 38, n. 12, 2015.

[95] S. Zayac e N. Finch, "Recipients' of implanted cardioverter-defibrillators actual and perceived adaptation: A review of the literature", *Journal of the American Academy of Nurse Practitioners*, vol. 21, n. 10, 2009.

[96] M. Hammash, S. M. McEvedy, J. Wright, J. Cameron, J. Miller, C. F. Ski, D. R. Thompson, M. J. Biddle, A. Wimsatt, M. Schrader, R. V. Smith, M. L. Chung e D. K. Moser, "Perceived control and quality of life among recipients of implantable cardioverter defibrillator", *Australian Critical Care*, 2019.

[97] A. Gauthey, S. Calle, S. Accinelli, P. Depuydt, C. Garnir Q.and Scavée, S. Marchandise, A. Wauters, P. Bordachar, J. de Pooter e J. le Polain de Waroux, "His bundle pacing for newly acquired pacing needs in patients implanted with a subcutaneous implantable cardioverter defibrillator: A feasibility study based on the automated screening score and clinical cases", *Journal of Cardiovascular Electrophysiology*, 2020.

[98] M. R. Gold, J. D. Aasbo, M. F. El-Chami, M. Niebauer, J. Herre, J. M. Prutkin, B. P. Knight, S. Kutalek, K. Hsu, R. Weiss et al., "Subcutaneous implantable cardioverter-defibrillator post-approval study: Clinical characteristics and perioperative results", *Heart Rhythm*, vol. 14, n. 10, 2017.

[99] L. R. A. Olde Nordkamp, T. F. Brouwer, C. Barr, D. A. M. J. Theuns, L. A. V. Boersma, J. B. Johansen, P. Neuzil, A. A. M. Wilde, N. Carter, M. Husby et al., "Inappropriate shocks in the subcutaneous icd: Incidence, predictors and management", *International journal of cardiology*, vol. 195, 2015.

[100] P. P. Borek e B. L. Wilkoff, "Pacemaker and icd leads: Strategies for long-term management", *Journal of interventional cardiac electrophysiology*, vol. 23, n. 1, 2008.

[101] J. Rivnay, H. Wang, L. Fenno, K. Deisseroth e G. G. Malliaras, "Next-generation probes, particles, and proteins for neural interfacing", *Science Advances*, vol. 3, n. 6, 2017.

[102] F. Zhang, L. Wang, E. S. Boyden e K. Deisseroth, "Channelrhodopsin-2 and optical control of excitable cells", *Nature methods*, vol. 3, n. 10, pp. 785–792, 2006.

[103] E. Pastrana, "Optogenetics: Controlling cell function with light", *Nature methods*, vol. 8, 2011.

[104] L. Fenno, O. Yizhar e K. Deisseroth, "The development and application of optogenetics", *Annual review of neuroscience*, vol. 34, 2011.

[105] I. Diester, M. T. Kaufman, M. Mogri, R. Pashaie, W. Goo, O. Yizhar, C. Ramakrishnan, K. Deisseroth e K. V. Shenoy, "An optogenetic toolbox designed for primates", *Nature neuroscience*, vol. 14, n. 3, 2011.

[106] H. Xu, L. Yin, C. Liu, X. Sheng e N. Zhao, "Recent advances in biointegrated optoelectronic devices", *Advanced Materials*, vol. 30, n. 33, 2018.

[107] E. A. Ferenczi, X. Tan e C. L. H. Huang, "Principles of optogenetic methods and their application to cardiac experimental systems", *Frontiers in physiology*, vol. 10, 2019.

[108] C. Goßler, C. Bierbrauer, R. Moser, M. Kunzer, K. Holc, W. Pletschen, K. Köhler, J. Wagner, M. Schwaerzle, P. Ruther et al., "Gan-based micro-led arrays on flexible substrates for optical cochlear implants", *Journal of Physics D: Applied Physics*, vol. 47, n. 20, 2014.

[109] A. B. Arrenberg, D. Y. R. Stainier, H. Baier e J. Huisken, "Optogenetic control of cardiac function", *Science*, vol. 330, n. 6006, 2010.

[110] O. J. Abilez, J. A. Baugh, M. L. Gorrepati, R. Prakash, C. Lee-Messer, M. Huang, F. Jia, J. Yu, K. D. Wilson, J. C. Wu et al., "Optogenetic control of human heart cells", *submitted for publication*, 2011.

[111] O. J. Abilez, "Biochemical, electrical, and optogenetic control of human pluripotent stem cell-derived cardiomyocytes", tesi di dott., Stanford University, 2012.

[112] U. Nussinovitch, R. Shinnawi e L. Gepstein, "Modulation of cardiac tissue electrophysiological properties with light-sensitive proteins", *Cardiovascular research*, vol. 102, n. 1, 2014.

[113] A. Klimas, C. M. Ambrosi, J. Yu, J. C. Williams, H. Bien e E. Entcheva, "Optodyce as an automated system for high-throughput all-optical dynamic cardiac electrophysiology", *Nature communications*, vol. 7, n. 1, 2016.

[114] E. Entcheva, "Cardiac optogenetics", *American Journal of Physiology-Heart and Circulatory Physiology*, vol. 304, n. 9, 2013.

[115] E. C. A. Nyns, R. H. Poelma, L. Volkers, J. J. Plomp, C. I. Bart, A. M. Kip, T. J. van Brakel, K. Zeppenfeld, M. J. Schalij, G. Q. Zhang et al., "An automated hybrid bioelectronic system for autogenous restoration of sinus rhythm in atrial fibrillation", *Science translational medicine*, vol. 11, n. 481, 2019.

[116] T. Bruegmann, T. Beiert, C. C. Vogt, J. W. Schrickel e P. Sasse, "Optogenetic termination of atrial fibrillation in mice", *Cardiovascular Research*, vol. 114, n. 5, 2018.

[117] B. O. Bingen, M. C. Engels, M. J. Schalij, W. Jangsangthong, Z. Neshati, I. Feola, D. L. Ypey, S. F. Askar, A. V. Panfilov, D. A. Pijnappels et al., "Light-induced termination of spiral wave arrhythmias by optogenetic engineering of atrial cardiomyocytes", *Cardiovascular research*, vol. 104, n. 1, pp. 194–205, 2014.

[118] L. Yu, L. Zhou, G. Cao, S. S. Po, B. Huang, X. Zhou, M. Wang, S. Yuan, Z. Wang, S. Wang et al., "Optogenetic modulation of cardiac sympathetic nerve activity to prevent ventricular arrhythmias", *Journal of the American College of Cardiology*, vol. 70, n. 22, pp. 2778–2790, 2017.

[119] E. C. A. Nyns, A. Kip, C. I. Bart, J. J. Plomp, K. Zeppenfeld, M. J. Schalij, A. A. F. De Vries e D. A. Pijnappels, "Optogenetic termination of ventricular arrhythmias in the whole heart: Towards biological cardiac rhythm management", *European heart journal*, vol. 38, n. 27, 2017.

[120] M. Funken, D. Malan, P. Sasse e T. Bruegmann, "Optogenetic hyperpolarization of cardiomyocytes terminates ventricular arrhythmia", *Frontiers in physiology*, vol. 10, 2019.

[121] T. Kim, J. G. McCall, Y. H. Jung, X. Huang, E. R. Siuda, Y. Li, J. Song, Y. M. Song, H. Pao, R. Kim et al., "Injectable, cellular-scale optoelectronics with applications for wireless optogenetics", *Science*, vol. 340, n. 6129, 2013.

[122] K. L. Montgomery, A. J. Yeh, J. S. Ho, V. Tsao, S. M. Iyer, L. Grosenick, E. A. Ferenczi, Y. Tanabe, K. Deisseroth, S. L. Delp et al., "Wirelessly powered, fully internal optogenetics for brain, spinal and peripheral circuits in mice", *Nature methods*, vol. 12, n. 10, 2015.

[123] M. W. Jenkins, A. R. Duke, S. Gu, Y. Doughman, H. J. Chiel, H. Fujioka, M. Watanabe, E. D. Jansen e A. M. Rollins, "Optical pacing of the embryonic heart", *Nature photonics*, vol. 4, n. 9, 2010.

[124] M. W. Jenkins, Y. T. Wang, Y. Q. Doughman, M. Watanabe, Y. Cheng e A. M. Rollins, "Optical pacing of the adult rabbit heart", *Biomedical optics express*, vol. 4, n. 9, 2013.

[125] M. G. Shapiro, K. Homma, S. Villarreal, C. Richter e F. Bezanilla, "Infrared light excites cells by changing their electrical capacitance", *Nature communications*, vol. 3, n. 1, 2012.

[126] S. M. Ford, M. Watanabe e M. W. Jenkins, "A review of optical pacing with infrared light", *Journal of neural engineering*, vol. 15, n. 1, 2017.

[127] L. Gentemann, S. Kalies, M. Coffee, H. Meyer, T. Ripken, A. Heisterkamp, R. Zweigerdt e D. Heinemann, "Modulation of cardiomyocyte activity using pulsed laser irradiated gold nanoparticles", *Biomedical optics express*, vol. 8, n. 1, 2017.

[128] A. Savchenko, V. Cherkas, C. Liu, G. B. Braun, A. Kleschevnikov, Y. I. Miller e E. Molokanova, "Graphene biointerfaces for optical stimulation of cells", *Science advances*, vol. 4, n. 5, 2018.

[129] F. Lodola, V. Vurro, S. Crasto, E. Di Pasquale e G. Lanzani, "Optical pacing of human-induced pluripotent stem cell-derived cardiomyocytes mediated by a conjugated polymer interface", *Advanced healthcare materials*, vol. 8, n. 13, 2019.

[130] N. Martino, P. Feyen, M. Porro, C. Bossio, E. Zucchetti, D. Ghezzi, F. Benfenati, G. Lanzani e M. Antognazza, "Photothermal cellular stimulation in functional bio-polymer interfaces", *Scientific reports*, vol. 5, 2015.

[131] F. Lodola, N. Martino, G. Tullii, G. Lanzani e M. R. Antognazza, "Conjugated polymers mediate effective activation of the mammalian ion channel transient receptor potential vanilloid 1", *Scientific reports*, vol. 7, n. 1, 2017.

[132] M. J. Fuchter, "On the promise of photopharmacology using photoswitches: A medicinal chemist's perspective", *Journal of Medicinal Chemistry*, 2020.

[133] J. Hinks, Y. Wang, W. H. Poh, B. C. Donose, A. W. Thomas, S. Wuertz, S. C. J. Loo, G. C. Bazan, S. Kjelleberg, Y. Mu et al., "Modeling cell membrane perturbation by molecules designed for transmembrane electron transfer", *Langmuir*, vol. 30, n. 9, 2014.

[134] L. E. Garner, J. Park, S. M. Dyar, A. Chworos, J. J. Sumner e G. C. Bazan, "Modification of the optoelectronic properties of membranes via insertion of amphiphilic phenylenevinylene oligoelectrolytes", *Journal of the American Chemical Society*, vol. 132, n. 29, 2010.

[135] H. Fujiwara e Y. Yonezawa, "Photoelectric response of a black lipid membrane containing an amphiphilic azobenzene derivative", *Nature*, vol. 351, n. 6329, 1991.

[136] M. Tanaka e Y. Yonezawa, "Photochemical regulation of ion transport through "quasi-channels" embedded in black lipid membrane", *Materials Science and Engineering: C*, vol. 4, n. 4, 1997.

[137] Y. Yonezawa, H. Fujiwara e T. Sato, "Photoelectric response of black lipid membranes incorporating an amphiphilic azobenzene derivative", *Thin solid films*, vol. 210, 1992.

[138] D. L. Fortin, M. R. Banghart, T. W. Dunn, K. Borges, D. A. Wagenaar, Q. Gaudry, M. H. Karakossian, T. S. Otis, W. B. Kristan, D. Trauner et al., "Photochemical control of endogenous ion channels and cellular excitability", *Nature methods*, vol. 5, n. 4, 2008.

[139] R. H. Kramer, A. Mourot e H. Adesnik, "Optogenetic pharmacology for control of native neuronal signaling proteins", *Nature neuroscience*, vol. 16, n. 7, 2013.

[140] I. Tochitsky, M. A. Kienzler, E. Isacoff e R. H. Kramer, "Restoring vision to the blind with chemical photoswitches", *Chemical reviews*, vol. 118, n. 21, 2018.

[141] L. Laprell, I. Tochitsky, K. Kaur, M. B. Manookin, M. Stein, D. M. Barber, C. Schön, S. Michalakis, M. Biel, R. H. Kramer et al., "Photopharmacological control of bipolar cells restores visual function in blind mice", *The Journal of clinical investigation*, vol. 127, n. 7, 2017.

[142] S. Osella e S. Knippenberg, "Triggering on/off states of photoswitchable probes in biological environments", *Journal of the American Chemical Society*, vol. 139, n. 12, 2017.

[143] J. Griffiths, "Photochemistry of azobenzene and its derivatives", *Chemical Society Reviews*, vol. 1, n. 4, 1972.

[144] G. S. Hartley, "The cis-form of azobenzene", *Nature*, vol. 140, n. 3537, 1937.

[145] H. M. D. Bandara e S. C. Burdette, "Photoisomerization in different classes of azobenzene", *Chemical Society Reviews*, vol. 41, n. 5, 2012.

[146] M. Moniruzzaman, P. Christogianni, R. M. Vrcelj e P. P. Gill, "Ultrasonic studies of solid azobenzene-decorated polymer thin films", *ACS omega*, vol. 3, n. 12, 2018.

[147] R. Turansk, M. Konôpka, N. L. Doltsinis, I. Štich e D. Marx, "Switching of functionalized azobenzene suspended between gold tips by mechanochemical, photochemical, and opto-mechanical means", *Physical Chemistry Chemical Physics*, vol. 12, n. 42, 2010.

[148] X. Tong, M. Pelletier, A. Lasia e Y. Zhao, "Fast cis–trans isomerization of an azobenzene derivative in liquids and liquid crystals under a low electric field", *Angewandte Chemie*, vol. 120, n. 19, 2008.

[149] L. Gagliardi, G. Orlandi, F. Bernardi, A. Cembran e M. Garavelli, "A theoretical study of the lowest electronic states of azobenzene: The role of torsion coordinate in the cis–trans photoisomerization", *Theoretical Chemistry Accounts*, vol. 111, n. 2-6, 2004.

[150] H. Fliegl, A. Köhn, C. Hättig e R. Ahlrichs, "Ab initio calculation of the vibrational and electronic spectra of trans-and cis-azobenzene", *Journal of the American Chemical Society*, vol. 125, n. 32, 2003.

[151] C. Boulègue, M. Löweneck, C. Renner e L. Moroder, "Redox potential of azobenzene as an amino acid residue in peptides", *ChemBioChem*, vol. 8, n. 6, 2007.

[152] M. Zhou, X. Liang, T. Mochizuki e H. Asanuma, "A light-driven dna nanomachine for the efficient photoswitching of rna digestion", *Angewandte Chemie International Edition*, vol. 49, n. 12, 2010.

[153] A. G. Cochran, N. J. Skelton e M. A. Starovasnik, "Tryptophan zippers: Stable, monomeric β-hairpins", *Proceedings of the National Academy of Sciences*, vol. 98, n. 10, 2001.

[154] G. A. Woolley, "Photocontrolling peptide α helices", *Accounts of chemical research*, vol. 38, n. 6, 2005.

[155] G. A. Woolley, E. Lee e F. Zhang, "Sgal: A computational method for finding surface exposed sites in proteins suitable for cys-mediated cross-linking", *Bioinformatics*, vol. 22, n. 24, 2006.

[156] F. Zhang, A. Zarrine-Afsar, M. S. Al-Abdul-Wahid, R. S. Prosser, A. R. Davidson e G. A. Woolley, "Structure-based approach to the photocontrol of protein folding", *Journal of the American Chemical Society*, vol. 131, n. 6, 2009.

[157] M. Banghart, K. Borges, E. Isacoff, D. Trauner e R. H. Kramer, "Light-activated ion channels for remote control of neuronal firing", *Nature neuroscience*, vol. 7, n. 12, 2004.

[158] C. Wyart, F. Del Bene, E. Warp, E. K. Scott, D. Trauner, H. Baier e E. Y. Isacoff, "Optogenetic dissection of a behavioural module in the vertebrate spinal cord", *Nature*, vol. 461, n. 7262, 2009.

[159] R. Numano, S. Szobota, A. Y. Lau, P. Gorostiza, M. Volgraf, B. Roux, D. Trauner e E. Y. Isacoff, "Nanosculpting reversed wavelength sensitivity into a photoswitchable iglur", *Proceedings of the National Academy of Sciences*, vol. 106, n. 16, 2009.

[160] R. H. Kramer, D. L. Fortin e D. Trauner, "New photochemical tools for controlling neuronal activity", *Current opinion in neurobiology*, vol. 19, n. 5, 2009.

[161] J. J. Chambers, M. R. Banghart, D. Trauner e R. H. Kramer, "Light-induced depolarization of neurons using a modified shaker k+ channel and a molecular photoswitch", *Journal of neurophysiology*, vol. 96, n. 5, 2006.

[162] L. Husaru, R. Schulze, G. Steiner, T. Wolff, W. D. Habicher e R. Salzer, "Potential analytical applications of gated artificial ion channels", *Analytical and bioanalytical chemistry*, vol. 382, n. 8, 2005.

[163] T. Hamada, Y. T. Sato, K. Yoshikawa e T. Nagasaki, "Reversible photoswitching in a cell-sized vesicle", *Langmuir*, vol. 21, n. 17, 2005.

[164] T. Hamada, R. Sugimoto, T. Nagasaki e M. Takagi, "Photochemical control of membrane raft organization", *Soft Matter*, vol. 7, n. 1, 2011.

[165] Y. Suzuki, K. H. Nagai, A. Zinchenko e T. Hamada, "Photoinduced fusion of lipid bilayer membranes", *Langmuir*, vol. 33, n. 10, 2017.

[166] S. C. Sebai, S. Cribier, A. Karimi, D. Massotte e C. Tribet, "Permeabilization of lipid membranes and cells by a light-responsive copolymer", *Langmuir*, vol. 26, n. 17, 2010.

[167] D. V. Tulumello e C. M. Deber, "Sds micelles as a membrane-mimetic environment for transmembrane segments", *Biochemistry*, vol. 48, n. 51, 2009.

[168] K. Takahashi e S. Yamanaka, "Induction of pluripotent stem cells from mouse embryonic and adult fibroblast cultures by defined factors", *cell*, vol. 126, n. 4, 2006.

[169] I. Batalov e A. W. Feinberg, "Differentiation of cardiomyocytes from human pluripotent stem cells using monolayer culture: Supplementary issue: Stem cell biology", *Biomarker insights*, vol. 10, 2015.

[170] E. Karbassi, A. Fenix, S. Marchiano, N. Muraoka, K. Nakamura, X. Yang e C. E. Murry, "Cardiomyocyte maturation: Advances in knowledge and implications for regenerative medicine", *Nature Reviews Cardiology*, 2020.

[171] M. Mazzola e E. Di Pasquale, "Toward cardiac regeneration: Combination of pluripotent stem cell-based therapies and bioengineering strategies", *Frontiers in Bioengineering and Biotechnology*, vol. 8, 2020.

[172] C. Kane, L. Couch e C. Terracciano, "Excitation–contraction coupling of human induced pluripotent stem cell-derived cardiomyocytes", *Frontiers in cell and developmental biology*, vol. 3, 2015.

[173] Y. Lee, K. Ng, W. Lai, Y. Chan, Y. Lau, Q. Lian, H. Tse e C. Siu, "Calcium homeostasis in human induced pluripotent stem cell-derived cardiomyocytes", *Stem Cell Reviews and Reports*, vol. 7, n. 4, 2011.

[174] F. Lodola, D. Morone, M. Denegri, R. Bongianino, H. Nakahama, L. Rutigliano, R. Gosetti, G. Rizzo, A. Vollero, M. Buonocore et al., "Adeno-associated virus-mediated casq2 delivery rescues phenotypic alterations in a patient-specific model of recessive catecholaminergic polymorphic ventricular tachycardia", *Cell death & disease*, vol. 7, n. 10, 2016.

[175] H. Nakahama e E. Di Pasquale, "Generation of cardiomyocytes from pluripotent stem cells", in *Patient-Specific Induced Pluripotent Stem Cell Models*, Springer, 2014.

[176] Z. Kalal, K. Mikolajczyk e J. Matas, "Forward-backward error: Automatic detection of tracking failures", in *2010 20th International Conference on Pattern Recognition*, IEEE, 2010.

[177] V. Rohlicek e J. Rohlicek, "Measurement of membrane capacitance and resistance of single cells using two frequencies", *Physiol. Res*, vol. 42, 1993.

[178] D. F. Donnelly, "A novel method for rapid measurement of membrane resistance, capacitance, and access resistance", *Biophysical journal*, vol. 66, n. 3, 1994.

[179] Y. Xu, L. Zhang, J. Xu, Y. Wei e X. Xu, "Membrane permeability of the human pluripotent stem cells to me2so, glycerol and 1, 2-propanediol", *Archives of biochemistry and biophysics*, vol. 550, 2014.

[180] M. Michalak e M. Opas, "Endoplasmic and sarcoplasmic reticulum in the heart", *Trends in cell biology*, vol. 19, n. 6, 2009.

[181] G. E. Palade, "The fine structure of blood capillaries", *J Appl phys*, vol. 24, 1953.

[182] E. Yamada, "The fine structure of the gall bladder epithelium of the mouse", *The Journal of biophysical and biochemical cytology*, vol. 1, n. 5, 1955.

[183] A. Echarri e M. A. Del Pozo, "Caveolae", *Current Biology*, vol. 22, n. 4, 2012.

[184] ——, "Caveolae–mechanosensitive membrane invaginations linked to actin filaments", *Journal of cell science*, vol. 128, n. 15, 2015.

[185] L. Pelkmans, J. Kartenbeck e A. Helenius, "Caveolar endocytosis of simian virus 40 reveals a new two-step vesicular-transport pathway to the er", *Nature cell biology*, vol. 3, n. 5, 2001.

[186] D. K. Sharma, J. C. Brown, A. Choudhury, T. E. Peterson, E. Holicky, D. L. Marks, R. Simari, R. G. Parton e R. E. Pagano, "Selective stimulation of caveolar endocytosis by glycosphingolipids and cholesterol", *Molecular biology of the cell*, vol. 15, n. 7, 2004.

[187] Y. Kang, Y. Ko e J. Seo, "Caveolin internalization by heat shock or hyperosmotic shock", *Experimental cell research*, vol. 255, n. 2, 2000.

[188] E. Boucrot, M. T. Howes, T. Kirchhausen e R. G. Parton, "Redistribution of caveolae during mitosis", *Journal of cell science*, vol. 124, n. 12, 2011.

[189] M. A. del Pozo, N. B. Alderson, W. B. Kiosses, H. Chiang, R. G. W. Anderson e M. A. Schwartz, "Integrins regulate rac targeting by internalization of membrane domains", *Science*, vol. 303, n. 5659, 2004.

[190] E. J. Smart, Y. Ying, P. A. Conrad e R. G. Anderson, "Caveolin moves from caveolae to the golgi apparatus in response to cholesterol oxidation.", *The Journal of cell biology*, vol. 127, n. 5, 1994.

[191] P. A. Conrad, E. J. Smart, Y. Ying, R. G. Anderson e G. S. Bloom, "Caveolin cycles between plasma membrane caveolae and the golgi complex by microtubule-dependent and microtubule-independent steps.", *Journal of Cell Biology*, vol. 131, n. 6, 1995.

[192] M. Gherghiceanu, L. Barad, A. Novak, I. Reiter, J. Itskovitz-Eldor, O. Binah e L. M. Popescu, "Cardiomyocytes derived from human embryonic and induced pluripotent stem cells: Comparative ultrastructure", *Journal of cellular and molecular medicine*, vol. 15, n. 11, 2011.

[193] R. G. Parton e M. A. Del Pozo, "Caveolae as plasma membrane sensors, protectors and organizers", *Nature reviews Molecular cell biology*, vol. 14, n. 2, 2013.

[194] P. Volpe, A. Villa, P. Podini, A. Martini, A. Nori, M. C. Panzeri e J. Meldolesi, "The endoplasmic reticulum-sarcoplasmic reticulum connection: Distribution of endoplasmic reticulum markers in the sarcoplasmic reticulum of skeletal muscle fibers", *Proceedings of the National Academy of Sciences*, vol. 89, n. 13, 1992.

[195] V. Robert, F. De Giorgi, M. L. Massimino, M. Cantini e T. Pozzan, "Direct monitoring of the calcium concentration in the sarcoplasmic and endoplasmic reticulum of skeletal muscle myotubes", *Journal of Biological Chemistry*, vol. 273, n. 46, 1998.

[196] L. Mackenzie, M. D. Bootman, M. Laine, M. J. Berridge, J. Thuring, A. Holmes, W. Li e P. Lipp, "The role of inositol 1, 4, 5-trisphosphate receptors in ca2+ signalling and the generation of arrhythmias in rat atrial myocytes", *The Journal of physiology*, vol. 541, n. 2, 2002.

[197] C. W. Taylor e S. C. Tovey, "Ip3 receptors: Toward understanding their activation", *Cold Spring Harbor perspectives in biology*, vol. 2, n. 12, 2010.

[198] E. A. Woodcock e S. J. Matkovich, "Ins (1, 4, 5) p3 receptors and inositol phosphates in the heart—evolutionary artefacts or active signal transducers?", *Pharmacology & therapeutics*, vol. 107, n. 2, 2005.

[199] N. Kapur e K. Banach, "Inositol-1, 4, 5-trisphosphate-mediated spontaneous activity in mouse embryonic stem cell-derived cardiomyocytes", *The Journal of physiology*, vol. 581, n. 3, 2007.

[200] Z. Sun C an.d Wang, L. Yue, Q. Huang, S. Lu e R. Wang, "Ros-initiated chemiluminescence-driven payload release from macrocycle-based azo-containing polymer nanocapsules", *Journal of Materials Chemistry B*, vol. 8, n. 38, 2020.

[201] R. Turansk, M. Konôpka, N. L. Doltsinis, I. Štich e D. Marx, "Switching of functionalized azobenzene suspended between gold tips by mechanochemical, photochemical, and opto-mechanical means", *Physical Chemistry Chemical Physics*, vol. 12, n. 42, 2010.

[202] S. K. Surampudi, H. R. Patel, G. Nagarjuna e D. Venkataraman, "Mechano-isomerization of azobenzene", *Chemical Communications*, vol. 49, n. 68, 2013.

[203] M. M. Hossain, E. Shimizu, M. Saito, S. R. Rao, Y. Yamaguchi e E. Tamiya, "Non-invasive characterization of mouse embryonic stem cell derived cardiomyocytes based on the intensity variation in digital beating video", *Analyst*, vol. 135, n. 7, 2010.

[204] T. C. Stummann, M. Wronski, T. Sobanski, B. Kumpfmueller, L. Hareng, S. Bremer e M. P. Whelan, "Digital movie analysis for quantification of beating frequencies, chronotropic effects, and beating areas in cardiomyocyte cultures", *Assay and Drug Development Technologies*, vol. 6, n. 3, 2008.

[205] X. Liu e D. Padfield, "Motion-based segmentation for cardiomyocyte characterization", in *International Workshop on Spatio-temporal Image Analysis for Longitudinal and Time-Series Image Data*, Springer, 2012.

[206] M. Maddah, J. D. Heidmann, M. A. Mandegar, C. D. Walker, S. Bolouki, B. R. Conklin e K. E. Loewke, "A non-invasive platform for functional characterization of stem-cell-derived cardiomyocytes with applications in cardiotoxicity testing", *Stem cell reports*, vol. 4, n. 4, 2015.

[207] A. Kamgoué, J. Ohayon, Y. Usson, L. Riou e P. Tracqui, "Quantification of cardiomyocyte contraction based on image correlation analysis", *Cytometry Part A: The Journal of the International Society for Advancement of Cytometry*, vol. 75, n. 4, 2009.

[208] T. Hayakawa, T. Kunihiro, S. Dowaki, H. Uno, E. Matsui, M. Uchida, S. Kobayashi, A. Yasuda, T. Shimizu e T. Okano, "Noninvasive evaluation of contractile behavior of cardiomyocyte monolayers based on motion vector analysis", *Tissue Engineering Part C: Methods*, vol. 18, n. 1, 2012.

[209] T. Hayakawa, T. Kunihiro, T. Ando, S. Kobayashi, E. Matsui, H. Yada, Y. Kanda, J. Kurokawa e T. Furukawa, "Image-based evaluation of contraction–relaxation kinetics of human-induced pluripotent stem cell-derived cardiomyocytes: Correlation and complementarity with extracellular electrophysiology", *Journal of molecular and cellular cardiology*, vol. 77, 2014.

[210] A. Ahola, A. L. Kiviaho, K. Larsson, M. Honkanen, K. Aalto-Setälä e J. Hyttinen, "Video image-based analysis of single human induced pluripotent stem cell derived cardiomyocyte beating dynamics using digital image correlation", *Biomedical engineering online*, vol. 13, n. 1, 2014.

[211] N. Huebsch, P. Loskill, M. A. Mandegar, N. C. Marks, A. S. Sheehan, Z. Ma, A. Mathur, T. N. Nguyen, J. C. Yoo, L. M. Judge et al., "Automated video-based analysis of contractility and calcium flux in human-induced pluripotent stem cell-derived cardiomyocytes cultured over different spatial scales", *Tissue Engineering Part C: Methods*, vol. 21, n. 5, 2015.

[212] A. Chen, E. Lee, R. Tu, K. Santiago, A. Grosberg, C. Fowlkes e M. Khine, "Integrated platform for functional monitoring of biomimetic heart sheets derived from human pluripotent stem cells", *Biomaterials*, vol. 35, n. 2, 2014.

[213] B. Pesquet-Popescu, M. Cagnazzo e F. Dufaux, "Motion estimation techniques", *Telecom ParisTech*, 2016.

[214] L. Kitchen e A. Rosenfeld, "Gray-level corner detection", *Pattern recognition letters*, vol. 1, n. 2, 1982.

[215] H. P. Moravec, "Obstacle avoidance and navigation in the real world by a seeing robot rover.", Stanford Univ CA Dept of Computer Science, rapp. tecn., 1980.

[216] D. Marr, S. Ullman e T. Poggio, "Bandpass channels, zero-crossings, and early visual information processing", *JOSA*, vol. 69, n. 6, 1979.